Università degli Studi di Padova
Department of Industrial Engineering

PHD COURSE IN INDUSTRIAL ENGINEERING
Curriculum: Chemical and Environmental Engineering
XXXIV series

A thesis submitted for the degree of Doctor of Philosophy

Numerical Modelling of Segregation Mechanisms in Bulk Materials

Coordinator and supervisor
Prof. Andrea Claudio Santomaso

PhD student
Monica Tirapelle

To my dear parents.
To my beloved Mattia.

Abstract

Granular materials are deeply rooted in the long history of science and technology. Furthermore, several industries process granular materials routinely, including chemical, food and pharmaceutical industries. Handling and processing of these materials remain a major challenge in numerous industrial applications. The main difficulty regards the mixing of particles with different properties because of their tendency to segregate spontaneously. Thus, the development of tools for predicting segregation is essential in order to control and minimize the occurrence.

This research project is concerned with the numerical modelling of segregation mechanisms in bulk materials for mixtures with varying degrees and types of particle dispersity, in many industrial settings. More specifically, we first study size-driven segregation in diluted binary mixtures. We then tackle segregation due to size differences in multi-component and polydisperse particle systems. In these cases, the segregation equations are fully coupled with the solid flow rheology. Since the coupling is challenging, only a few other studies exist in this area. We then propose a new mathematical model for density-driven segregation in binary mixtures. Unlike the previous models, in this case, we employ a one-way coupling. Furthermore, the velocity field is determined directly from analytic solutions rather than by solving the momentum equation. The inclusion of density differences would have led to compressible velocity fields and hence, to more complex models. An additional chapter describes a new model for particle-size segregation that include the compressibility of the velocity field. Wherever possible, the models are validated in a two-way comparison among experiments and theory. In the other cases, the validation procedure is accomplished with DEM simulations.

All theories are capable of reproducing both qualitatively and quantitatively what happens in reality. Thus, the proposed segregation models represent a step towards a complete and accurate description of segregation in a variety of dense granular flows. Furthermore, the models can help engineers in developing mitigation strategies and in rationally designing and scaling equipment, processes, and process control.

Sommario

I materiali granulari sono profondamente radicati nella lunga storia della scienza e della tecnologia. Essi vengono trattati quotidianamente da numerose industrie tra cui l'industria chimica, l'industria alimentare e l'industria farmaceutica. Tuttavia, la loro manipolazione e la loro lavorazione rimangono un importante problema in numerose applicazioni industriali. Uno dei problemi più rilevanti è quello della miscelazione di particelle aventi proprietà diverse dal momento che tendono a segregare spontaneamente. Pertanto, lo sviluppo di strumenti per prevedere la segregazione è essenziale per controllare e ridurre al minimo il fenomeno.

Questo progetto di ricerca riguarda la modellazione numerica dei meccanismi di segregazione in materiali sfusi, per miscele con vari gradi e tipi di dispersione particellare e applicati a diversi contesti industriali. Nello specifico, studieremo dapprima la segregazione per dimensione in miscele binarie diluite. Successivamente tratteremo la segregazione per taglia in sistemi di particelle multicomponenti e polidispersi. In questi casi, le equazioni di segregazione sono accoppiate con la reologia del flusso solido in modo bidirezionale. Poiché l'accoppiamento bidirezionale è piuttosto complesso, esistono solo pochi altri studi a riguardo. Proporremo poi un nuovo modello matematico per descrivere la segregazione per densità in miscele binarie. A differenza dei modelli precedenti, in questo caso utilizzeremo un accoppiamento unidirezionale. Inoltre, il campo di velocità sarà determinato direttamente da soluzioni analitiche piuttosto che risolvendo l'equazione di conservazione della quantità di moto. L'inclusione delle differenze di densità avrebbe portato a campi di velocità comprimibili e quindi, a modelli più complessi. Un ulteriore capitolo descrive un nuovo modello di segregazione per taglia che include la comprimibilità del campo di velocità. Ove possibile, i modelli saranno validati con esperimenti. Negli altri casi, la procedura di validazione si realizzerà con simulazioni DEM.

Tutte le teorie sono in grado di riprodurre sia qualitativamente che quantitativamente ciò che accade nella realtà. Pertanto, i modelli di segregazione proposti rappresentano un ulteriore passo avanti verso una descrizione completa e accurata della segregazione in una varietà di flussi granulari densi. Questi modelli possono inoltre aiutare gli ingegneri a sviluppare strategie di mitigazione, a progettare e dimensionare razionalmente apparecchiature e a sviluppare più efficaci sistemi di controllo di processo.

Acknowledgements

Several people have offered suggestions, comments and ideas related to the work contained in this thesis. A special thanks to my supervisor, Prof Andrea Claudio Santomaso, for his immense support and his advice throughout my all doctoral studies. I also feel greatly indebted to Dr Silvia Volpato for her teachings and for providing me with technical suggestions. They were grateful people to work with. I would also like to express my gratitude to Dr Riccardo Artoni and Dr Patrick Richards for the warm hospitality during my mobility at IFSTTAR (The French Institute of Science and Technology for Transport, Development and Networks), site of Nantes. Least but not last, I would like to acknowledge the support and the immense kindness of Dr Luca Mazzei of the Chemical Engineering Department at UCL.

Finally, I would like to thank my entire family and my dearest husband, Mattia. They have always been a source of love and encouragement. All that I have accomplished would not have been possible without their support.

Contents

List of Figures

List of Tables

Chapter 1

Introduction

> Granular materials represent a major object of human activities: as measured in tons, the first material manipulated on earth is water; the second is granular matter.
>
> Pierre-Gilles de Gennes

1.1 Introduction to granular matter

Granular materials are defined as a collection of discrete solid grains having size larger than one micron. Below one micron, thermal agitation is important and Brownian motion can be seen. Above one micron, thermal agitation is negligible. As a consequence, granular systems have to gain energy from shear, vibration or external volume forces (i.e. gravity, electric and magnetic fields...) to remain active [1, 2].

Granular materials are widespread in nature, everyday life and industrial processes. Classical examples of granular materials are sand, soil, snow; food products such as seeds, rice, sugar, coffee; chemical and pharmaceutical products like pills, tablets and powders. Examples of unit operations involving granular materials include fluidized catalytic reactions (bulk chemical industry), compression of drugs into tablets (pharmaceutical industry), freeze-drying (food industry), mixing and blending (cosmetic industry) and concrete production (construction industry).

Even if granular systems are so pervasive both in nature and industry, processes involving these types of materials are often poorly understood compared to their fluid processing counterparts. Depending on the particular flow conditions, they can exhibit a variety of behaviours that are in many ways different from those of conventional solids, liquids and gases [2–4]. In addition, the properties of granular materials can depend upon their history [5]. For these reasons, granular materials have grabbed the attention of many physicists and have led to several new theories.

Today, granular matters constitute a very multi-disciplinary field of research.

1.2 Motivation

Granular materials are made of particles having different properties such as different sizes, shapes and/or densities. A common industrial practice is to mix the different types of particles before processing in order to obtain a homogeneous mixture (e.g. to produce pills) [6]. However, granular materials tend to segregate under external agitation rather than to mix. When segregation happens, the main implications for industries include product rejection, variable look, variable taste, excessive blending times, customer complaints, erratic dosage mass, poor quality control and an increase in production costs. To give an example, Saint-Gobain Weber's production facilities have to re-process about 100 kt of segregated products each year, with a waste of money roughly estimated at 1 million euros [7]. Thus, the development of tools for predicting segregation is essential in order to control and minimize the occurrence.

A central motivation for the study of segregation in dry granular media is its implication in many industrial phenomena and the lack of fundamental research. Although there has been considerable recent progress in developing continuum-based segregation models [8], a fundamental understanding of the phenomenon is still lacking and industrial applications still rely on expensive and time-consuming trial-and-error approaches.

1.3 Research objectives

We restrict ourselves to the case of segregation of dry and cohesionless mixtures of particles differing in size and density. We present new models for both size- and density-driven segregation. These will be incorporated into continuum descriptions involving advection and diffusion. The purposes of the present research are:

- to improve understanding of the physical insights of the segregation phenomena and its underlying mechanisms;
- to develop general and physically-based segregation models for predicting segregation of bulk materials in the framework of continuum mechanics;
- to apply segregation models to different flow configurations such as flow down inclined planes, emptying of a storage silo and confined flows in shear cells;
- to track the evolution of the local porosity by introducing flow compressibility.

Unlike most of the models reported in the literature, in developing our models we have favoured physical approaches, probabilistic assumptions and mathematical developments supported by empirical observations. The proposed segregation models can help engineers in developing mitigation strategies and in designing industrial equipment.

1.4 Outlines

This thesis is divided into chapters that can be outlined as follow.

Chapter 2 surveys the state of the art of segregation and provides a summary description of the continuum theories and rheological models mostly adopted throughout the thesis.

Chapter 3 presents a theoretical model to predict the percolation velocity in sheared binary systems under diluted conditions whose assumptions are verified through statistical considerations and ad-hoc DEM simulations. The model is validated experimentally for a range of size ratios and shear rates.

Chapter 4 provides a continuum framework for predicting size-driven segregation in multi-component granular mixtures. The standard advection-diffusion transport equation is fully coupled with a phenomenological hydrodynamic rheological model, whereas the segregation velocity relies on the falling probabilities and the overall mass conservation. The model is implemented for simulating size-driven segregation in ternary mixtures during discharge from a storage hopper and it is validated against experimental and DEM simulation data taken from the literature.

Since real mixtures are usually polydisperse over their size, in chapter 5 we shed further light on size-driven segregation by considering polydisperse mixtures. The evolution of the particle size distribution is described through a Population Balance Equation (PBE) solved numerically with the Direct Quadrature Method of Moments. To allow segregation and micromixing to occur, the size-conditioned velocity of the particles is closed with a segregation-remixing model. The PBE is then included in an Eulerian-Eulerian framework and solved in a commercial Computational Fluid Dynamics (CFD) code. The model is used to study granular flows down inclined planes. The results are compared with those obtained from Discrete Element Method simulations.

Because the effect of large density differences may also be an important factor determining segregation, in chapter 6 we propose a continuum approach to model density-driven segregation. We use a segregation-diffusion transport equation, constitutive relations and a segregation velocity analogous to Stokes' law. The model is implemented for a range of density ratios and a range of heavy particle concentrations. The results are validated by comparison with experimental findings.

Chapter 7 sits apart from the rest of this thesis. In there, we propose a new segregation model where the assumption of particle incompressibility is overcome. Each class of particle is represented with an Eulerian model. The interaction between classes is represented by drag forces. The model must be implemented and validated in future works.

The main conclusions and possible extensions to this work are summarized in chapter 8. Some of the mathematical proofs are reported in Appendix A.

Bibliography

[1] P. G. de Gennes. Granular matter: a tentative view. *Reviews of modern physics*, 71 (2):S374, 1999.

[2] I. S. Aranson and L. S. Tsimring. Patterns and collective behavior in granular media: Theoretical concepts. *Reviews of Modern Physics*, 78(2):641–692, 2006.

[3] H. M. Jaeger and S. R. Nagel. Physics of the granular state. *Science*, pages 1523–1531, 1992.

[4] P. G. de Gennes. From rice to snow. In *Nishina Memorial Lectures*, pages 297–318. Springer, 2008.

[5] L. P. Kadanoff. Built upon sand: Theoretical ideas inspired by granular flows. *Reviews of Modern Physics*, 71(1):435, 1999.

[6] G. H. Ristow. *Pattern formation in granular materials.* Springer Science & Business Media, 2000.

[7] N. Engblom. *Segregation of powder mixtures in silos with particular reference to dry mineral-based construction materials.* PhD thesis, Åbo Akademi University, 2012.

[8] K. van der Vaart, P. Gajjar, G. Epely-Chauvin, N. Andreini, J. M. N. T. Gray, and C. Ancey. Underlying asymmetry within particle size segregation. *Physical review letters*, 114(23):238001, 2015.

Chapter 2

State of the art

This chapter provides the state of the art of the physics of segregation and surveys the recent advances in the field.

2.1 Mixing and Segregation

A poor mixing process can lead to segregation, which is the tendency of particles to separate from the mixture. Segregation is due to many factors that can be classified as mixture properties and process dynamics. So factors like size, density, shape, surface roughness, as well as process vibration, shear strain and equipment geometry could determine segregation. The most famous example of segregation is the Brazil nut effect whereby large particles rise to the top of a shaken container of mixed nuts [1, 2]. Other phenomena related to the segregation mechanism are observed in connection with the deposition of sediments in a geological context [3]. Let us report as example landslides, rock-falls, debris flows, pyroclastic flows and snow avalanches [4, 5]. Segregation of granular materials is frequently encountered also in many industrial flows practice, including granular convection, hopper flows and rotating drums [6, 7].

Segregation may be helpful in some situations such as in mining and stone crushing [8, 9]. Devices such as pinched sluices, Humphreys spirals and Reichert cones take advantage of the mechanism of gravity separation both in slurries and in dry state for sorting materials of different sizes and different densities into approximately monodisperse classes [3, 8].

Nevertheless, segregation is more often an undesired phenomenon. It may determine hot spots and selectivity problems in reactors, it may affect the performance of a catalytic packed bed, it may degrade the quality of a final product [10–12]. These are just a few examples of the many adverse situations causing an increase in production costs and wastes [13]. Thus, the development of tools for predicting segregation, not only at a small scale but also in industrial equipment, is essential in order to control and minimize the occurrence.

Even if segregation has been studied for nearly a century and a lot of efforts have been made to understand its underlying physical mechanisms [14–16], a quantitative analysis of the phenomenon is still lacking, and much remains to be done [6, 17, 18]. Design decisions are still made without a fundamental understanding of the phenomenon and, to minimize the effects of segregation, process engineers still rely on empirical heuristic rules and avoidance practices [6, 18].

2.1.1 Segregation mechanisms

Due to the huge variety of processes and handling regimes, a lot of segregation mechanisms can be found in the literature. These include: rolling, sieving, push-away or displacement, angle of repose, sifting or percolation, displacement or floating migration, trajectory or inertia segregation, dusting or air-current segregation, fluidization or elutriation, impact or bouncing, concentration driven displacement, agglomeration, embedding and squeeze expulsion [19–24]. Among these, the most frequent and important mechanism of segregation is interparticle percolation [25].

Interparticle percolation is responsible for small particles to filter through the gaps in a matrix of larger grains. Percolation occurs spontaneously if the particle size ratio ($\delta_R = d_f/D_c$) is smaller than 0.155 [26, 27]. For higher size ratios, it is commonly referred to as shear-induced percolation or kinetic sieving and is due to shear or vibrations [28, 29]. Due to the strain applied across the failure zone, the larger particles will yield a space into which a smaller particle can move downward [12, 30]. Opposed to the percolation effect, there is squeeze expulsion. This phenomenon describes the squeeze of a particle into an adjacent layer, mostly upward, and affects all the particles, regardless of their properties. However, for larger and lighter particles, it is easier to rise. Combined with sieving, squeeze expulsion determines the net percolation [3]. Depending on the flow geometry, interparticle percolation can generate different final configurations. For instance, in a rotating drum, fine particles accumulate at the centre of the bulk mass forming a core surrounded by the coarser ones [31–33]. In a heap flow, the fine particles travel shorter paths because they percolate below the flowing surface, whilst the coarser grains tend to flow at the surface arriving and accumulating at the base of the pile [3, 34, 35].

2.1.2 Theoretical approaches to segregation

Several authors have looked at deriving new theories for predicting segregation in dense granular flows (i.e. where there are multiple enduring frictional contacts).

The most effective driver of particle segregation is size differences. Thus, let us first consider binary mixtures of large and small particles. The first quantitative description of interparticle percolation was proposed by Bridgwater and coworkers [10, 36–40] and was implemented in a convective diffusion equation. Successively, Savage and Lun [3] proposed a new theory based on a statistical argument about the distribution of void spaces. For the first time, they considered percolation to be a combination of two mechanisms: kinetic sieving and squeeze expulsion. Dolgunin and coworkers [41, 42] proposed a segregation theory based on empirical observations. In their model, they included the effect of diffusional remixing. The diffusion coefficient was determined using considerations from the kinetic theory. They applied their theory to problems in which there were both a dense basal avalanche and a rarefied saltation layer.

In the last decades, other theoretical models have been proposed. These models are derived from the mixture theory under the following assumptions: every point in the domain is simultaneously occupied by both the constituents, the pore space is incorporated into each phase, the granular flow is incompressible and the partial properties (partial density, partial pressure and partial velocity) are defined for each constituent. These types of models differ from each other mainly for the definition of the interaction forces. Gray and Thornton [43] introduced a pressure scaling for determining the proportion of the hydrostatic load which is carried by the large and small particles. They assumed a linear velocity-dependent drag and a grain-grain surface interaction force. Gray and Chugunov [44] extended the latter theory by adding a remixing force that seeks to drive a grain belonging to one phase toward the area of lower concentration. Thornton et al. [45] and Tunuguntla et al. [46] extended the theory further by incorporating the buoyancy effects of an interstitial fluid and a shear rate-dependent drag, respectively. They both neglected the effect of diffusion. Note that, the models derived from the mixture theory are of limited applicability (i.e. they are valid for a size ratio lower than two) because they do not account for the percolation effects [46, 47].

There exist also theoretical models supported by numerical simulations. We cite as an example the model of Fan et al. [48] that includes the effects of three different mechanisms: advection, diffusion and shear-rate dependent segregation velocity; and the model of Hajra et al. [49] where the segregation velocity depends on the particle size ratio. In their theory, Bertuola et al. [50] considered the dependence of both the shear rate and the size ratio and did not neglect the deviatoric part of the stress tensor.

Unlike binary mixtures, there exist only a few theoretical studies for size-segregation in multi-component granular mixtures. Deng et al. [51] explored the segregation of ternary granular materials in a gravity-driven flow. Gray and Ancey [23] extended the existing theory for binary mixtures to the case of size segregation of an arbitrary number of discrete grain-size classes. Barker et al. [52] developed a general multi-component segregation model that is fully coupled with a solid flow rheology. To the author's knowledge, only Marks et al. [53] and Schlick et al. [54] mapped the entire evolution of the grain-size distribution by replacing the finite number of constituents with a probability density function.

Other researchers considered the case of segregation solely due to density differences in different devices. Khakhar et al. [55] focused on density-driven segregation in a rotating cylinder and proposed a continuum theory based on a species balance equation. Khakhar et al. [56] used transport equations from the kinetic theory to model the segregation of spherical particles in a chute flow. Tripathi and Khakhar [57] derived a continuum model based on a theory for the motion of a single particle in a dense flow. This has a similar structure to the size-segregation models. More recently, Xiao et al. [5] and Duan et al. [58] proposed an expression for the interspecies momentum exchange in density bi-disperse granular flows as an extension of ideas from kinetic theory.

To conclude, only a few studies deal with the coupled effect of size and density differences [46, 53, 59–61].

2.2 Computational modelling

Unlike regular fluids, the behaviour of solid systems is complex to understand and requires computational models. Traditionally, particle systems have been treated as pseudo-solids or pseudo-liquids and have been simulated with continuum modelling. However, with the increase of computer power, discrete approaches have become popular [62]. These include Cellular Automata (CA), Monte Carlo methods (DSMC), Contact Dynamics (CD) and the Discrete Element Method (DEM) [6]. Here, we briefly review the Discrete Element Method and Continuum modelling. If the Discrete Element Method simulations are useful for describing accurately micro-mechanisms on a local scale, the continuum approach seems to be more efficient for simulating macro scale events.

2.2.1 Review of Discrete Element Method

Cundall and Strack were the pioneers who developed the Discrete Element Method (DEM). Since their first publication on DEM in 1979, the method has gained importance and it has been applied to a variety of fields such as geophysics, engineering and mathematics. In the area of particle technology, it has been employed to investigate numerous industrial processes including powder mixing and segregation.

The method has numerous advantages: it is simple, flexible, general and it provides information at the individual particle scale that is not accessible from physical experimentation (e.g. stress information). Furthermore, the topology of particle interaction can evolve freely and it does not require a hypothesis on the rheological behaviour of the solid phase [62, 64–66]. However, due to the computational effort demanded, this approach cannot be used to simulate particles in full-scale industrial equipment.

2.2.1.1 The principle of DEM

In Discrete Element Method simulations, the particle systems are treated as discontinua assemblies of discrete spheres so that each particle is tracked at each time step. Let us consider a spherical particle labelled i with radius R_i. The translational and rotational accelerations of i are given by Newton's second law of motion [62–64, 66]:

$$m_i \frac{d\boldsymbol{v}_i}{dt} = \sum_{j=1}^{k_i} \boldsymbol{F}_{ij} + m_i \boldsymbol{g}_i \,, \tag{2.1}$$

$$I \frac{d\boldsymbol{\omega}_i}{dt} = \sum_{j=1}^{k_i} \boldsymbol{F}_{ij}^T R_i + \sum_{j=1}^{k_i} M_r \,, \tag{2.2}$$

where $\boldsymbol{v}_i$ and $\boldsymbol{\omega}_i$ are the linear and angular velocity, $\boldsymbol{F}_i$ is the resulting force acting between particles i and j and it is usually decomposed into its normal and tangential components (i.e. $\boldsymbol{F}_{ij}^N$ and $\boldsymbol{F}_{ij}^T$), $\boldsymbol{g}_i$ is the gravitational acceleration, $\boldsymbol{I}$ is the moment of inertia and $\boldsymbol{F}_{ij}^T R_i$ is the torque that causes particle i to rotate. Since the relative rotation between particles or between a particle and a wall produces rolling resistance, sometimes also a rotational frictional torque is incorporated into Eq. 2.2 (i.e. $\sum_{j=1}^{k_i} M_r$). For a complete review of the different rolling resistance models see Ai et al. [67].

There exist several numerical schemes used for integrating Eqs. 2.1 and 2.2. The oldest one was proposed by Verlet [68, 69]. In its original form, the equations for advancing the position and the velocities of the i-th particle read:

$$\boldsymbol{x}_i\left(t+\Delta t\right) = 2\boldsymbol{x}_i\left(t\right) - \boldsymbol{x}_i\left(t-\Delta t\right) + a_i(t)\Delta t^2 \,, \tag{2.3}$$

$$\theta_i\left(t+\Delta t\right) = 2\theta_i\left(t\right) - \theta_i\left(t-\Delta t\right) + \alpha_i(t)\Delta t^2 \,, \tag{2.4}$$

$$\boldsymbol{v}_i(t) = \frac{1}{2\Delta t}\left[\boldsymbol{x}_i\left(t+\Delta t\right) - \boldsymbol{x}_i\left(t-\Delta t\right)\right] \,, \tag{2.5}$$

$$\boldsymbol{\omega}_i(t) = \frac{1}{2\Delta t}\left[\theta_i\left(t+\Delta t\right) - \theta_i\left(t-\Delta t\right)\right] \,, \tag{2.6}$$

where $\boldsymbol{x}_i$ and θ_i represent the particle coordinates and its rotational displacement, respectively, whereas $a_i \equiv \frac{d\boldsymbol{v}_i}{dt}$ and $\alpha_i \equiv \frac{d\boldsymbol{\omega}_i}{dt}$ are the translational and rotational acceleration. This formulation is disadvantageous since the particle positions are given at time $t+\Delta t$, while the velocities are given one time step behind. Furthermore, it requires storing the particle positions for three consecutive time steps. A modified version of the Verlet algorithm that tackles these deficiencies is the so-called half-step (i.e. central finite difference) leap-frog scheme [62, 66, 69]. In this case, the translational and angular velocities are given by:

$$\boldsymbol{v}_i\left(t+\frac{\Delta t}{2}\right) = \boldsymbol{v}_i\left(t-\frac{\Delta t}{2}\right) + a_i(t)\Delta t \,, \tag{2.7}$$

$$\boldsymbol{\omega}_i\left(t+\frac{\Delta t}{2}\right) = \boldsymbol{\omega}_i\left(t-\frac{\Delta t}{2}\right) + \alpha_i(t)\Delta t \,, \tag{2.8}$$

whereas the particle positions are updated in accordance to:

$$\boldsymbol{x}_i\left(t+\Delta t\right) = \boldsymbol{x}_i\left(t\right) + \boldsymbol{v}_i\left(t+\frac{\Delta t}{2}\right)\Delta t \,, \tag{2.9}$$

$$\theta_i\left(t+\Delta t\right)=\theta_i\left(t\right)+\boldsymbol{\omega}_i\left(t+\frac{\Delta t}{2}\right)\Delta t\,. \tag{2.10}$$

Another possible method is the velocity-Verlet algorithm that provides positions, velocities and accelerations at the same time step [69, 70]:

$$\boldsymbol{x}_i\left(t+\Delta t\right)=\boldsymbol{x}_i\left(t\right)+\boldsymbol{v}_i(t)\Delta t+a_i(t)\frac{\Delta t^2}{2}\,, \tag{2.11}$$

$$\theta_i\left(t+\Delta t\right)=\theta_i\left(t\right)+\boldsymbol{\omega}_i(t)\Delta t+\alpha_i(t)\frac{\Delta t^2}{2}\,, \tag{2.12}$$

$$\boldsymbol{v}_i\left(t+\Delta t\right)=\boldsymbol{v}_i(t)+\left[a_i(t)+a_i(t+\Delta t)\right]\frac{\Delta t}{2}\,, \tag{2.13}$$

$$\boldsymbol{\omega}_i\left(t+\Delta t\right)=\boldsymbol{\omega}_i\left(t\right)+\left[\alpha_i(t)+\alpha_i(t+\Delta t)\right]\frac{\Delta t}{2}\,. \tag{2.14}$$

In this thesis, discrete numerical simulations were performed with the molecular dynamics platform LIGGGHTS® PUBLIC [71, 72], which implement, by default, the velocity form of the Verlet integration scheme.

Once the particle positions are updated, it is checked whether new contacts between a particle and its neighbouring particles have been established. By definition, two spherical particles are in contact if the distance between their centres, D, is less than the sum of their radii (i.e. if $D < R_i + R_j$). If this is the case, the magnitude of the overlap $\delta \equiv R_i + R_j - D$ is used for the calculation of the repulsive forces [63].

2.2.1.2 Contact modelling

Different force-displacement relationships are provided in the literature for modelling the contact forces between interacting particles. Some of them are contact laws based upon theoretical contact mechanics, whereas others are simplified phenomenological models [66]. Because the latter ones require lower computational time, they are the most commonly employed by researchers. Among these models, there are the linear and non-linear springs models, with and without dashpots.

In a general spring-dashpot model, the interparticle contact is represented as a spring and a dashpot both in the normal and tangential directions (see Fig. 2.1). If the spring accounts for the elastic contribution to the response, the dashpot accounts for the dissipation of energy due to plastic deformations [64]. The normal and tangential contact forces are calculated respectively as:

$$F_{ij}^{N}=k_n\delta\boldsymbol{n}_{ij}-\gamma_n v\boldsymbol{n}_{ij}\,, \tag{2.15}$$

$$F_{ij}^{T}=k_t\delta\boldsymbol{t}_{ij}-\gamma_t v\boldsymbol{t}_{ij}\,, \tag{2.16}$$

where k_n and k_t are spring elastic constants, γ_n and γ_t are viscous damping constants, $\delta\boldsymbol{n}_{ij}$ and $\delta\boldsymbol{t}ij$ are the normal and tangential displacements, and $v\boldsymbol{n}_{ij}$ and $v\boldsymbol{t}_{ij}$ are relative

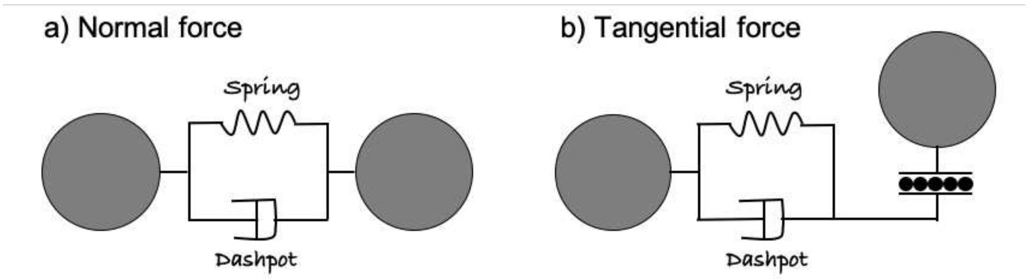

Figure 2.1: a) Normal and b) tangential components of the contact force between two interacting particles considering a spring-dashpot model.

velocities [72]. Note that, by Newton's third law, the force experienced by a particle j in contact with i is: $\boldsymbol{F}_{ji} = -\boldsymbol{F}_{ij}$ [73]. Furthermore, the tangential force is governed by Coulomb's condition:

$$|F_{ij}^T| \leq \mu F_{ij}^N \, , \tag{2.17}$$

with μ being the sliding friction coefficient. When the Coulomb criterion is not satisfied, particle sliding occurs.

2.2.1.3 Choice of the contact parameters

To implement the contact models, the user has to define the contact stiffness coefficients, the damping viscous coefficients and the coefficient of sliding friction. These parameters are related to the intrinsic properties of the material: Young's modulus, Poisson's ratio, restitution coefficient, particle intrinsic density and particle diameter. One can choose to define the coefficients directly (i.e. by implementing the Hooke/stiffness or Hertz/stiffness contact models). There exist some rules of thumb in order to implement suitable coefficients. Otherwise, one can decide to specify the material properties instead (i.e. by implementing the standard Hooke or Hertz contact models). The material properties can be obtained from the literature or through particle characterization.

Table 2.1 summarizes the formulation for the stiffnesses as well as the damping coefficients both for the linear and non-linear spring-dashpot model. The linear model was first introduced by Walton and Braun [74] and it is based on a Hooke type relation [64]. The latter was firstly developed by Hertz and Mindlin [75, 76] and it is based on Hertz's theory [64]. Note that, in the last decades, various methods of modelling collisions and several modification of the integral non-linear model of Mindlin have been proposed [77].

As regards the time step, it must be small enough to avoid the propagation of the disturbance waves through the neighbourhood, but as large as possible so as to increase the computational efficiency [62, 66]. Thus, a suitable time step has to be no greater than the critical time step. In the case of the linear contact models, the critical time step is related to the ratio between the particle mass and the contact stiffness governing the

	Coefficients	Symbol	Linear model	Non-linear model
Normal	Stiffness	k_n	$\frac{16}{15}\sqrt{R^*E^*}\left(\frac{15m^*V^2}{16\sqrt{R^*E^*}}\right)^{\frac{1}{5}}$	$\frac{4}{3}E^*\sqrt{R^*\delta}$
	Damping	γ_n	$\sqrt{\frac{4m^*k_n}{1+\left(\frac{\pi}{ln(e_n)}\right)^2}} \geq 0$	$-\sqrt{\frac{10}{3}}\beta\sqrt{S_n m^*} \geq 0$
Tangent	Stiffness	k_t	K_n	$8G^*\sqrt{R^*\delta}$
	Damping	γ_t	γ_n	$-\sqrt{\frac{10}{3}}\beta\sqrt{S_t m^*} \geq 0$

with $S_n = 2E^*\sqrt{R^*\delta}$, $S_t = 8G^*\sqrt{R^*\delta}$, $\beta = \frac{\ln(e_n)}{\sqrt{\ln^2(e_n)+\pi^2}}$, $\frac{1}{E^*} = \frac{1-\sigma_i^2}{E_i} + \frac{1-\sigma_j^2}{E_j}$,
$\frac{1}{G^*} = \frac{2(2-\sigma_i)(1+\sigma_i)}{E_i} + \frac{2(2-\sigma_j)(1+\sigma_j)}{E_j}$, $\frac{1}{R^*} = \frac{1}{R_i} + \frac{1}{R_j}$ and $\frac{1}{m^*} = \frac{1}{m_i} + \frac{1}{m_j}$

Table 2.1: The normal and tangential coefficients for the linear and non-linear spring-dashpot models. In their formulations, E is the Young's modulus, G is the shear modulus, σ is the Poisson ratio and e_n is the coefficient of restitution [72]

particle motion [62, 78]:

$$t_{crit} = 2\sqrt{\frac{m}{k_n}} \, . \tag{2.18}$$

In the case of the non-linear spring contact model, the critical time step cannot be calculated a priori, however, as a rule of thumb, it should not be greater than the 20% of the Rayleigh time [62].

2.2.1.4 Our implementation

In this thesis, we have implemented DEM simulations to model size and density segregation in binary systems, as well as size segregation in poly-disperse mixtures. The simulations have allowed us to deepen the physical insight of the systems under investigation. Sometimes, DEM simulations have instead been used as a validation tool.

We have used an open-source DEM particle simulation software: LIGGGHTS® PUBLIC [71, 72]. In LIGGGHTS, two granular models are implemented: 1) a linear spring-dashpot model based on Hooke's relation and 2) a non-linear model based on Hertz's theory. For each one, one can choose to provide directly the coefficients or the intrinsic properties of the materials. In chapter 3 and chapter 5, we have employed the non-linear spring-dashpot model and we have defined the material properties. On the other hand, in chapter 6 we have employed the linear spring-dashpot model and we have directly defined the coefficients. As a rolling resistance model, we have always employed the Constant Directional Torque (CDT) wherein M_r is modelled as [67]:

$$M_r = -\frac{\boldsymbol{\omega}_i - \boldsymbol{\omega}_j}{|\boldsymbol{\omega}_i - \boldsymbol{\omega}_j|}\mu_r R_r \boldsymbol{F}_{ij}^N \, . \tag{2.19}$$

In Eq. 2.19, $R_r \equiv r_i r_j/(r_i + r_j)$ represents the rolling radius and μ_r is the coefficient of rolling friction. The direction of the torque is against the relative rotation between the two in-contact bodies [67, 72]. Despite the CDT model can generate non-stopping oscillating torque in pseudo-static systems, it has been used because of its simple formulation and low computational effort.

2.2.2 Review of continuum mechanics models

Even if granular materials are discontinuous mediums, their behaviour is commonly described by continuum approaches. Granular materials are considered to behave like incompressible non-Newtonian pseudo-fluids with a peculiar rheological behaviour, and the continuum equations used are the conservation of mass, momentum and (sometimes) granular temperature. In the following sections, we present the dynamical equations for the solid phase and a few granular rheological models.

2.2.2.1 Conservation equations

Granular materials are two-phase systems composed of a solid phase and a fluid phase. The solid phase consists of discrete solid particles, whereas the fluid phase fills the interstitial space between particles [79]. If we assume that the effect of the interstitial fluid on the solid phase is negligible (a reasonable assumption if the grains are dry and have sufficient inertia - i.e. they are sufficiently large and dense), the macroscopic balance equations for mass and linear momentum of the solid phase read, respectively [79, 80]:

$$\frac{\partial \rho}{\partial t} + \nabla \cdot (\rho \boldsymbol{u}) = 0\,, \tag{2.20}$$

$$\frac{\partial}{\partial t}(\rho \boldsymbol{u}) + \nabla \cdot (\rho \boldsymbol{u}\boldsymbol{u}) = \nabla \cdot \boldsymbol{\sigma} + \rho \boldsymbol{g}\,, \tag{2.21}$$

where ρ is the solid bulk density (or partial density) defined as the amount of solid per unit volume of the mixture, $\boldsymbol{u}$ is the velocity field, $\boldsymbol{\sigma}$ is the stress tensor and $\boldsymbol{g}$ is the gravitational acceleration.

When a granular material flows, in addition to the average velocity of the grains, there are random velocities generated by collisions and induced by the flow itself [81]. Since the random motion of individual particles is analogous to the thermal motion of molecules in a dense gas, kinetic theories of rapid granular flows that extend the Chapman-Enskog kinetic theory of dense gases have been developed [79]. The magnitude of these velocity fluctuations, which have been regarded as granular temperature, is defined as $\theta \equiv \frac{1}{3}\langle \tilde{u}^2 \rangle$, where $\tilde{u}$ is the fluctuating component of the velocity vector. The constitutive law for θ is derived from the macroscopic balance equations for the translational kinetic energy [79, 80]:

$$\frac{\partial}{\partial t}\left[\rho(\varepsilon^T + E^T)\right] + \nabla \cdot \left[\rho(\varepsilon^T + E^T)\boldsymbol{u}\right] = \nabla \cdot (\boldsymbol{\sigma} \cdot \boldsymbol{u}) - \nabla \cdot \boldsymbol{q}^T + \rho \boldsymbol{g} \cdot \boldsymbol{u} - z^T\,, \tag{2.22}$$

where $\boldsymbol{q}^T$ is a diffusive energy flux, z^T represents the rate of dissipation of mechanical energy, ε^T and E^T are the kinetic energies associated with the fluctuating velocity field $\tilde{\boldsymbol{u}}$ and the average velocity field $\boldsymbol{u}$, respectively. The equation for the conservation of

$E^T \equiv \frac{1}{2}\langle u^2 \rangle$ can be derived by taking the dot product of the velocity $\boldsymbol{u}$ with the momentum equation (i.e. Eq. 2.21):

$$\frac{\partial}{\partial t}\left(\rho \frac{1}{2}\langle u^2 \rangle\right) + \nabla \cdot \left(\rho \boldsymbol{u} \frac{1}{2}\langle u^2 \rangle\right) = \boldsymbol{u} \cdot \nabla \cdot \boldsymbol{\sigma} + \rho \boldsymbol{g} \cdot \boldsymbol{u}\,, \tag{2.23}$$

whereas the equation for the kinetic energy ε^T associated with the fluctuating velocity is obtained subtracting Eq. 2.23 from Eq. 2.22 and decomposing the stress tensor into its spherical and deviatoric contributions (i.e. $\boldsymbol{\sigma} \equiv -p\boldsymbol{I} + \boldsymbol{\tau}$):

$$\frac{\partial}{\partial t}\left(\rho \varepsilon^T\right) + \nabla \cdot \left(\rho \varepsilon^T \boldsymbol{u}\right) = -p\nabla \cdot \boldsymbol{u} + \boldsymbol{\tau} \colon \nabla \boldsymbol{u} - \nabla \cdot \boldsymbol{q}^T - z^T\,. \tag{2.24}$$

Introducing the definition of θ into Eq. 2.24, it yields to the general constitutive law for the granular temperature:

$$\frac{3}{2}\frac{\partial}{\partial t}\left(\rho\theta\right) + \frac{3}{2}\nabla \cdot \left(\rho\theta\boldsymbol{u}\right) = -p\nabla \cdot \boldsymbol{u} + \boldsymbol{\tau} \colon \nabla \boldsymbol{u} - \nabla \cdot \boldsymbol{q}^T - z^T\,. \tag{2.25}$$

This set of differential equations gives p, $\boldsymbol{u}$ and θ; however, $\boldsymbol{\tau}$, $\boldsymbol{q}^T$ and z^T remain unknown.

For granular systems made of particles differing only by size, we can assume phase incompressibility. Under the assumption of incompressible granular flows (i.e. the packing density ν is constant throughout the solid domain and all particles have the same intrinsic density ρ^*), the conservation laws for the mass, momentum and granular temperature reduce to:

$$\nabla \cdot \boldsymbol{u} = 0\,, \tag{2.26}$$

$$\rho\left[\frac{\partial \boldsymbol{u}}{\partial t} + \boldsymbol{u} \cdot \nabla \boldsymbol{u}\right] = -\nabla p + \nabla \cdot \boldsymbol{\tau} + \rho \boldsymbol{g}\,, \tag{2.27}$$

$$\frac{3}{2}\rho\left[\frac{\partial \theta}{\partial t} + \boldsymbol{u} \cdot \nabla \theta\right] = \boldsymbol{\tau} \colon \nabla \boldsymbol{u} - \nabla \cdot \boldsymbol{q}^T - z^T\,. \tag{2.28}$$

Note that, this assumption does not hold for granular systems made of particles differing by density. The inclusion of density differences implies that the bulk velocity field is compressible.

2.2.2.2 Granular rheology - monodisperse systems

The conservation equations have to be supplemented by constitutive relations that describe the material characteristics, providing the closure of the stress tensor [81, 82]. Even if different rheological models of dense granular flows have been proposed in the literature, a unified version still lacks. In this thesis, we have employed the incompressible $\mu(I)$ rheology proposed by the Groupement De Recherche Milieux Divisés [83] and the phenomenological hydrodynamic model by Artoni et al. [80]. Before describing these models in detail, we will introduce the definition of effective viscosity and Inertial number.

The effective viscosity

Let us consider a mono-disperse granular material characterized by spherical grains of diameter d and intrinsic density ρ_p. Its stress state is described by the Cauchy's stress tensor, $\boldsymbol{\sigma}$, which may be decomposed into an isotropic and a deviatoric part:

$$\boldsymbol{\sigma} = -p\boldsymbol{I} + \boldsymbol{\tau}\,, \tag{2.29}$$

where p is the pressure, $\boldsymbol{I}$ is the identity tensor and $\boldsymbol{\tau}$ is the deviatoric stress tensor. Closing $\boldsymbol{\sigma}$, therefore, reduces to expressing constitutively $\boldsymbol{\tau}$. The closure of $\boldsymbol{\tau}$ is achieved by specifying three constitutive equations: a flow rule, an alignment condition and a plastic yield condition [84]. Let us begin with the flow rule. If we consider incompressible granular systems, the flow rule far from the interface between solid and air is:

$$\nabla \cdot \boldsymbol{u} = 0\,. \tag{2.30}$$

The alignment condition is formulated in terms of the strain-rate tensor [84–86]

$$\boldsymbol{D} \equiv \frac{1}{2}\left(\nabla\boldsymbol{u} + \nabla\boldsymbol{u}^T\right) \tag{2.31}$$

and reads:

$$\frac{\boldsymbol{\tau}}{||\boldsymbol{\tau}||} = \frac{\boldsymbol{D}}{||\boldsymbol{D}||}\,, \tag{2.32}$$

where $||\cdot||$ denotes the second invariant that is, by definition: $||\cdot|| \equiv \sqrt{\mathrm{tr}(\cdot^2)/2}$. This condition states that the principal directions of $\boldsymbol{\tau}$ and $\boldsymbol{D}$ must be aligned (i.e. the eigenvectors must be parallel) [87]. The third constitutive equation, take the form of a generalized yield condition that relates $||\boldsymbol{\tau}||$ with the pressure:

$$||\boldsymbol{\tau}|| = \mu p\,, \tag{2.33}$$

being μ the effective friction coefficient. Introducing the yield condition (Eq. 2.33) into the alignment condition (Eq. 2.32) leads to a closure relation for the deviatoric stress tensor:

$$\boldsymbol{\tau} = \mu p \frac{\boldsymbol{D}}{||\boldsymbol{D}||}\,. \tag{2.34}$$

If we consider that for incompressible granular flows the shear rate is $\dot{\gamma} = 2||\boldsymbol{D}||$, and if we substitute the definition of $\boldsymbol{D}$ (i.e. Eq. 2.31), Eq. 2.34 becomes:

$$\boldsymbol{\tau} = \frac{\mu p}{\dot{\gamma}}\left(\nabla\boldsymbol{u} + \nabla\boldsymbol{u}^T\right)\,, \tag{2.35}$$

where, by definition, the effective viscosity, η, is:

$$\eta = \frac{\mu p}{\dot{\gamma}}\,. \tag{2.36}$$

As a result, the closure of $\boldsymbol{\tau}$ is achieved by closing η. For mono-disperse granular systems, η can be determined by means of different rheological models such as the incompressible $\mu(I)$-rheology [83, 88], non-local rheology [89] and kinetic theories [90].

The inertial number

The non-dimensional Inertial number is a fundamental parameter used to describe the rheology of granular materials. For a single granular material composed of nearly identical rigid and spherical particles, the inertial number takes the form [83, 91]:

$$I = \frac{d\dot{\gamma}}{\sqrt{p/\rho^*}} \,. \tag{2.37}$$

The Inertial number can be interpreted in terms of the ratio between two time scales:

$$I = \frac{t_p}{t_\gamma} \,. \tag{2.38}$$

where $t_p \equiv d/\sqrt{p/\rho^*}$ is a microscopic grain rearrangement time scale and $t_\gamma \equiv 1/\dot{\gamma}$ is a macroscopic flow time scale [83, 92]. If the former refers to the time required by a particle to rearrange at the microscopic length scale, the latter refers to the time required by a grain to cross the grain underneath [83, 93].

The value of I enables the classification of the flow regimes [93]. Low inertial numbers identify the so-called quasi-static regime of flow [94]. In this regime, the grain inertia is not relevant [91], the macroscopic deformations are slow compared to microscopic rearrangement and the flow is characterized by multi-body long-lasting contacts between neighbouring particles [95, 96]. On the other hand, large values of I correspond to the kinetic (or collisional) regime. Here, the system is dilute and the grains interact only by binary collisions. Since the flow properties share common features with an agitated gas, kinetic theories have been developed to describe this regime [91, 94, 97, 98]. In between the quasi-static and the rapid regimes, there is the intermediate (or dense inertial) regime of flow. In the intermediate regime, the solid fraction is close to the maximum solid fraction and continuous paths of long-lasting contacts between grains exist [91, 96]. To switch from the quasi-static to the inertial regime, one can either increase the shear rate or decrease the pressure [93].

The $\mu(I)$ constitutive law

The $\mu(I)$-rheology was originally proposed by the Groupement De Recherche Milieux Divisés [83] to describe dense granular flows under the hypothesis of flow incompressibility. According to the $\mu(I)$-rheology, the shear stress is proportional to the normal stress:

$$||\boldsymbol{\tau}|| = \mu(I)p \,. \tag{2.39}$$

The coefficient of proportionality $\mu(I)$, which is a function of the Inertial number, is the friction coefficient [91]. Different friction laws have been postulated for the closure of $\mu(I)$. In the dense flow regime (i.e. $10^{-3} < I < 0.3$), it has been observed that the effective friction coefficient varies almost linearly with I, starting from a minimum value, μ_{min} [91]:

$$\mu(I) = \mu_{min} + bI \,, \tag{2.40}$$

where the parameters μ_{min} and b are characteristic of the flowing material. However, the effective friction coefficient tends to saturate for $I > 0.2$ [88]. Thus, the most frequently used form for expressing $\mu(I)$ is [88]:

$$\mu(I) = \mu_s + \frac{\mu_2 - \mu_s}{I_0/I + 1} \,, \tag{2.41}$$

where μ_s is the static friction coefficient, μ_2 is the limiting value toward which the friction coefficient converges at high inertial numbers, and I_0 is a constant. The friction coefficient expressed in this way is an increasing monotonic function: it starts from the critical minimum value μ_s for zero shears and increases asymptotically to μ_2 when I diverges.

For more complex configurations, where the flow is characterized by shears in different directions, a 3D generalization of Eq. 2.39 is required [88, 92]. Assuming flow incompressibility and isotropic pressure, the internal stress tensor in tensorial form becomes:

$$\sigma_{ij} = -p\delta_{ij} + \tau_{ij} \,, \tag{2.42}$$

where:

$$\tau_{ij} = \eta\dot{\gamma}_{ij} \quad \text{with} \quad \eta = \frac{\mu(I)p}{|\dot{\gamma}|} \quad \text{and, in turn,} \quad |\dot{\gamma}| = \sqrt{\frac{1}{2}\dot{\gamma}_{ij}\dot{\gamma}_{ij}} \,. \tag{2.43}$$

It should be noticed that the effective viscosity diverges to infinity when the shear rate goes to zero. Thus, the material flows only if the following condition is satisfied:

$$|\tau| > \mu_s p \,. \tag{2.44}$$

Furthermore, the rheology is local since the stress depends on the local shear rate and local pressure [93].

The phenomenological hydrodynamic model

The phenomenological hydrodynamic rheological model proposed by Artoni et al. [80] is based on the local granular temperature definition $\theta(z)$. Thus, to close Eq. 2.28, one has to express constitutively $\boldsymbol{\tau}$, $\boldsymbol{q}^T$ and z^T. We have seen that for incompressible granular flow, $\boldsymbol{\tau} = 2\eta\boldsymbol{D} = \eta(\nabla\boldsymbol{u} + \nabla\boldsymbol{u}^T)$ where η is the effective viscosity of the solid phase. The viscosity is analogous to Eyring's equation for simple liquids, where the thermodynamic temperature is replaced by the granular temperature, and it has been scaled with particle diameter and bulk density. Thus, it reads [80]:

$$\eta = \rho d^2 \eta_0 \exp\left(\frac{\theta^*}{\theta}\right) , \tag{2.45}$$

where η_0 is the viscosity coefficient parameter, d is the diameter of the particles, θ^* is a granular temperature scale. The constitutive law for θ is the one reported in Eq. 2.28. For what concerns the energy flux, Artoni et al. [80] assumed an isotropic diffusion-like mechanism:

$$\boldsymbol{q}^T = -k\nabla\theta , \tag{2.46}$$

where the diffusion coefficient reads $k = k'\rho d^2$. The energy dissipation rate is instead formulated as follow [80]:

$$z^T = \mu p|\dot{\gamma}| . \tag{2.47}$$

Note that, this rheology has been extensively used to describe the flow rheological properties in silo geometries [50, 80, 99].

2.2.2.3 Generalized rheological models

In previous paragraphs, we have stated a few granular rheological models that have been clearly developed for predicting the flow properties of homogeneous granular systems. However, segregating systems are made of particles differing by size and/or by density. Segregation results in changes in the local rheology and consequently the flow [57]. Thus, for a complete description of segregation, one has to define generalized rheological models that account for local constituent concentration [53, 98].

The $\mu(I)$-rheology (Section 2.2.2.2) essentially depends on the Inertial number, which is a function of particle size and particle density. For size-segregating systems made of discrete size classes, Rognon et al. [100] proposed a new version of the inertial number in which the particle size is replaced with the locally-averaged diameter of the grains, $\bar{d}$:

$$I = \frac{\bar{d}|\dot{\gamma}|}{\sqrt{p/\rho^*}} . \tag{2.48}$$

As in Tripathi and Khakhar [101], the locally-averaged diameter is taken to be:

$$\bar{d} = \sum \phi_i d_i , \tag{2.49}$$

where ϕ_i is the local solid volume ratio of the i-th species and hence, $\sum \phi_i = 1$ in the bulk solid domain.

Analogously, for polydisperse granular materials, we propose to replace the particle diameter with the average diameter of the PSD, which is expressed as the ratio between the first- and the zeroth-order moments of the distribution:

$$\bar{\mathcal{D}} = \frac{\mathcal{M}_1}{\mathcal{M}_0}\,, \tag{2.50}$$

Thus, the inertial number becomes:

$$I = \frac{\bar{\mathcal{D}}\dot{\gamma}}{\sqrt{p/\rho^*}}\,. \tag{2.51}$$

In density-segregating systems having same sized particles, however, I must depend on the local density of the solid mixture:

$$\bar{\rho} = \sum \phi_i \rho_i\,. \tag{2.52}$$

Thus, the Inertial number becomes:

$$I = \frac{d|\dot{\gamma}|}{\sqrt{p/\bar{\rho}}}\,. \tag{2.53}$$

Note that, the inclusion of density differences implies that the bulk velocity field is compressible therefore also a solid bulk viscosity must be specified (see chapter 8 for more details).

Analogously, if we generalize the Artoni et al. rheology for the case of multi-component systems of different sized particles, we obtain:

$$\eta = \eta_0 \rho \overline{d^2} \exp\left(\frac{\theta^*}{\theta}\right)\,, \tag{2.54}$$

whereas, the diffusion coefficient appearing in Eq. 2.46 becomes:

$$k = k' \rho \overline{d^2}\,. \tag{2.55}$$

For the case of density-driven segregation instead, applying the Artoni et al. rheology means solving the general constitutive law for the granular temperature accounting for particle compressibility (i.e. Eq. 2.25) and using the following diffusion coefficient:

$$k = k' \bar{\rho} d^2\,. \tag{2.56}$$

Again, in the latter case one must define also the bulk viscosity.

Note that, when only one component is present (i.e. $\phi_i = 1$), all the previous Eqs. reduce to the original formulations for mono-disperse systems.

2.3 The segregation equation

The conservation equations for the solid phase (see Section 2.2.2.1) allow the bulk velocity field, pressure and granular temperature to be tracked in space and time. However, modelling segregation requires specifying further equations for the evolution of the different species. Many models to describe particle segregation have been proposed in the literature (see Section 2.1.2). These all have the general form of an advection–diffusion segregation equation and are combined with constitutive relation for the segregation flux [15, 52].

2.3.1 Advection-diffusion segregation equation

The volume concentration of the i-th sized class, ϕ_i, which is defined as the volume of particles of species i per unit of solid mixture volume, is described through the following advection-diffusion segregation equation [10, 44, 48]:

$$\frac{\partial \phi_i}{\partial t} + \nabla \cdot (\boldsymbol{u}\phi_i) = -\nabla \cdot F(\phi_i) + \nabla \cdot (\boldsymbol{\mathcal{D}} \nabla \phi_i) \ , \tag{2.57}$$

where $F(\phi_i)$ is the net segregation flux and $\boldsymbol{\mathcal{D}}$ is the diffusion coefficient. These quantities are local quantities that depend on particle concentration and velocity gradient [15]. For an N-components system, $N-1$ transport equations of this type must be solved indeed, because of the summation constraint, the evolving composition of the N-th component reads:

$$\phi_N = 1 - \sum_{i=1}^{N-1} \phi_i \, . \tag{2.58}$$

The coupling between segregation and flow is achieved by solving simultaneously the Navier-Stokes and transport equations [15]. The velocity field featured in Eq. 2.57 is the solution of the momentum balance equation (see Eq. 2.27). The local composition of species, solution of Eqs. 2.57 and 2.58, is in turn used to determine the local viscosity, and hence the velocity field.

2.3.2 The segregation flux

The net segregation flux appearing in Eq. 2.57 is defined as $F(\phi_i) \equiv \phi_i \boldsymbol{v_{i,seg}}$ where $\boldsymbol{v_{i,seg}}$ is the segregation velocity. Different constitutive relations for the segregation velocity have been proposed in the literature for the dilute limit. For non-dilute mixtures, DEM simulations have helped uncover the dependence of $\boldsymbol{v_{i,seg}}$ on concentration and kinematics [15]. In this thesis, we provide new constitutive equations describing the segregation velocity for dilute mixtures, multi-component mixtures as well as polydisperse mixtures. These equations depend on local concentration and kinematics.

2.3.3 Description of the free surface

As mentioned above, granular systems are a two-phase flows. The two simulated phases are the bulk solid and the superficial ambient air. The two phases do not inter-penetrate and are separated by the solid free surface. To describe the evolution of the free surface, we employed the level set method, which is suitable for moving interfaces [102]. By definition, the level set function, $\psi(\boldsymbol{x}, t)$, is a continuous step function (smoothed for numerical reasons) that takes the values of 0 in one domain and of 1 in the other. The isocontour $\psi = 0.5$ corresponds to the interface. The level set function is transported by an advection equation:

$$\frac{\mathrm{D}\psi}{\mathrm{D}t} = 0\,, \tag{2.59}$$

where $\mathrm{D}\cdot/\mathrm{D}t$ is the substantial derivative.

2.4 Conclusions

Modelling of segregation processes requires the confluence of several tools, including continuum and discrete descriptions [92]. In this chapter, we have surveyed some of the tools employed in this project. In what follows, indeed, we will propose continuum models for size- and density-driven segregation. The continuum model framework predictions will then be extensively compared with results from experiments and/or DEM simulations.

Bibliography

[1] J. C. Williams. The segregation of powders and granular materials. *Fuel Soc. J*, 14: 29–34, 1963.

[2] A. Rosato, K. J. Strandburg, F. Prinz, and R. H. Swendsen. Why the brazil nuts are on top: Size segregation of particulate matter by shaking. *Physical review letters*, 58(10):1038, 1987.

[3] S. B. Savage and C. K. K. Lun. Particle size segregation in inclined chute flow of dry cohesionless granular solids. *Journal of Fluid Mechanics*, 189:311–335, 1988.

[4] J. M.N.T. Gray and K. Hutter. Pattern formation in granular avalanches. *Continuum Mechanics and Thermodynamics*, 9(6):341–345, 1997.

[5] H. Xiao, P. B. Umbanhowar, J. M. Ottino, and R. M. Lueptow. Modelling density segregation in flowing bidisperse granular materials. *Proceedings of the Royal Society A: Mathematical, Physical and Engineering Sciences*, 472:1–21, 2016.

[6] Julio M. Ottino and D. V. Khakhar. Mixing and segregation of granular materials. *Annu. Rev. Fluid Mech*, pages 55–91, 2000.

[7] I. S. Aranson and L. S. Tsimring. Patterns and collective behavior in granular media: Theoretical concepts. *Reviews of Modern Physics*, 78(2):641–692, 2006.

[8] B. Wills. Mineral processing technology: New york city, 1979.

[9] A. Kudrolli. Size separation in vibrated granular matter. *Reports on progress in physics*, 67(3):209, 2004.

[10] J. Bridgwater, W. S. Foo, and D.J. Stephens. Particle Mixing and Segregation in Failure Zones - Theory and Experiment. *Powder Technology*, 41:147–158, 1985.

[11] J. M. N. T. Gray. Particle Segregation in Dense Granular Flows. *Annu. Rev. Fluid Mech*, 50(1):407–33, 2018.

[12] A. M. Scott and J. Bridgwater. Interparticle percolation: a fundamental solids mixing mechanism. *Industrial & Engineering Chemistry Fundamentals*, 14(1):22–27, 1975.

[13] M. Tirapelle, S. Volpato, and A. C. Santomaso. Shear-induced particle segregation in binary mixtures: Verification of a percolation theory. *Particuology*, 57:214–222, 2021.

[14] Y. Fan, K. V. Jacob, B. J. Freireich, and R. M. Lueptow. Segregation of granular materials in bounded heap flow: A review. *Powder Technology*, 312:67–88, 2017.

[15] P. B. Umbanhowar, R. M. Lueptow, and J. M. Ottino. Modeling segregation in granular flows. *Annual Review of Chemical and Biomolecular Engineering*, 10:129–153, 2019.

[16] S. Volpato, M. Tirapelle, and A. C. Santomaso. Modeling and experimental investigation of shear-induced particle percolation in diluted binary mixtures. *Physical Review E*, 102(1):1–8, 2020.

[17] M. Alonso, M. Satoh, and K. Miyanami. Optimum combination of size ratio, density ratio and concentration to minimize free surface segregation. *Powder Technology*, 68(2):145–152, 1991.

[18] J. J. McCarthy. Turning the corner in segregation. *Powder Technology*, 192(2): 137–142, 2009.

[19] J. Mosby. *Investigations of the Segregation of Particulate Solids with Emphasis on the Use of Segregation Testers.* PhD thesis, Thesis, Telemark College, Porsgrunn, Norway, 1996.

[20] S.R. De Silva. Mixing and segregation in industrial processes. *IFPRI Report SAR*, pages 12–20, 1997.

[21] G. F. Salter. *Investigations into the segregation of heaps of particulate materials with particular reference to the effects of particle size.* PhD thesis, University of Greenwich, 1999.

[22] S. R. De Silva, A. Dyrøy, and G. G. Enstad. Segregation mechanisms and their quantification using segregation testers. In *IUTAM Symposium on Segregation in Granular Flows*, pages 11–29. Springer, 2000.

[23] J. M.N.T. Gray and C. Ancey. Multi-component particle-size segregation in shallow granular avalanches. *Journal of Fluid Mechanics*, 678:535–588, 2011.

[24] G. Liu. Understanding and minimizing powder segregation. , Dow Du Pont, 2018.

[25] J. C. Williams. The segregation of particulate materials. A review. *Powder Technology*, 15:245–251, 1976.

[26] J. Bridgwater and N. D. Ingram. Rate of spontaneous inter-particle percolation. *Transaction of the institution of chemical engineers and the chemical engineer*, 49 (3):163–+, 1971.

[27] A. D. Rosato, F. Prinz, K. J. Standburg, and R. Swendsen. Monte Carlo simulation of particulate matter segregation. *Powder Technology*, 49:59–69, 1986.

[28] R. Hogg. Mixing and segregation in powders: evaluation, mechanisms and processes. *KONA Powder and Particle Journal*, 27:3–17, 2009.

[29] N. Khola and C. Wassgren. Correlations for shear-induced percolation segregation in granular shear flows. *Powder technology*, 288:441–452, 2016.

[30] J. Bridgwater. Mixing and segregation mechanisms in particle flow. In *Granular matter*, pages 161–193. Springer, 1994.

[31] A. A. Boateng and P. V. Barr. Modelling of particle mixing and segregation in the transverse plane of a rotary kiln. *Chemical Engineering Science*, 51(17):4167–4181, 1996.

[32] A. C. Santomaso, R. Artoni, and P. Canu. Controlling axial segregation in drum mixers through wall friction: cellular automata simulations and experiments. *Chemical Engineering Science*, 90:151–160, 2013.

[33] E. Alizadeh, O. Dubé, F. Bertrand, and J. Chaouki. Characterization of mixing and size segregation in a rotating drum by a particle tracking method. *AIChE Journal*, 59(6):1894–1905, 2013.

[34] S. Wiederseiner, N. Andreini, G. Épely-Chauvin, G. Moser, M. Monnereau, J. M. N. T. Gray, and C. Ancey. Experimental investigation into segregating granular flows down chutes. *Physics of Fluids*, 23(1):013301, 2011.

[35] V. N. Dolgunin and A. A. Ukolov. Segregation modeling of particle rapid gravity flow. *Powder Technology*, 83(2):95–103, 1995.

[36] A. M. Scott and J. Bridgwater. Self-Diffusion of Spherical Particles in a Simple Shear Apparatus. *Powder Technology*, 14:177–183, 1976.

[37] J. Bridgwater. Mixing and segregation mechanisms in particle flow. In *Granular matter*, pages 161–193. Springer, 1994.

[38] M.H. Cooke, J. Bridgwater, and A.M. Scott. Interparticle percolation: lateral and axial diffusion coefficients. *Powder Technology*, 21(2):183–193, 1978.

[39] J. Bridgwater, M. H. Cooke, and A. M. Scott. Interparticle percolation: equipment development and mean percolation velocities. *Transactions of the Institution of Chemical Engineers*, 56:157—167, 1978.

[40] M. H. Cooke and J. Bridgewater. Interparticle percolation: a statistical mechanical interpretation. *Industrial & Engineering Chemistry Fundamentals*, 18(1):25–27, 1979.

[41] V. N. Dolgunin and A. A. Ukolov. Segregation modeling of particle rapid gravity flow. *Powder technology*, 83(2):95–103, 1995.

[42] V. N. Dolgunin, A. N. Kudy, and A. A. Ukolov. Development of the model of segregation of particles undergoing granular flow down an inclined chute. *Powder Technology*, 96(3):211–218, 1998.

[43] J. M.N.T. Gray and A. R. Thornton. A theory for particle size segregation in shallow granular free-surface flows. *Proceedings of the Royal Society A: Mathematical, Physical and Engineering Sciences*, 461(2057):1447–1473, 2005.

[44] J. M. N. T. Gray and V. A. Chugunov. Particle-size segregation and diffusive remixing in shallow granular avalanches. *Journal of Fluid Mechanics*, 569:365–398, 2006.

[45] A. R. Thornton, J. M. N. T. Gray, and A. J. Hogg. A three-phase mixture theory for particle size segregation in shallow granular free-surface flows. *Journal of Fluid Mechanics*, 550:1–25, 2006.

[46] D. R. Tunuguntla, O. Bokhove, and A. R. Thornton. A mixture theory for size and density segregation in shallow granular free-surface flows. *Journal of Fluid Mechanics*, 749:99–112, 2014.

[47] A. Thornton, T. Weinhart, S. Luding, and O. Bokhove. Modeling of particle size segregation: calibration using the discrete particle method. *International journal of modern physics C*, 23(08):1240014, 2012.

[48] Y. Fan, C. P. Schlick, P. B. Umbanhowar, J. M. Ottino, and R. M. Lueptow. Modelling size segregation of granular materials: the roles of segregation, advection and diffusion. *Journal of Fluid Mechanics*, 741:252–279, 2014.

[49] S. K. Hajra, D. Shi, and J. J. McCarthy. Granular mixing and segregation in zigzag chute flow. *Physical Review E*, 86(6):061318, 2012.

[50] D. Bertuola, S. Volpato, P. Canu, and A. C. Santomaso. Prediction of segregation in funnel and mass flow discharge. *Chemical Engineering Science*, 150:16–25, 2016.

[51] Z. Deng, P. B. Umbanhowar, J. M. Ottino, and R. M. Lueptow. Continuum modelling of segregating tridisperse granular chute fow. *Proceedings of the Royal Society A: Mathematical, Physical and Engineering Sciences*, 474(2211), 2018.

[52] T. Barker, M. Rauter, E. S. F. Maguire, C. G. Johnson, and J. M. N. T. Gray. Coupling rheology and segregation in granular flows. *Journal of Fluid Mechanics*, 909, 2021.

[53] B. Marks, P. G. Rognon, and I. Einav. Grainsize dynamics of polydisperse granular segregation down inclined planes. *Journal of Fluid Mechanics*, 690:499–511, 2012.

[54] C. P. Schlick, A. B. Isner, B. J. Freireich, Y. Fan, P. B. Umbanhowar, J. M. Ottino, and R. M. Lueptow. A continuum approach for predicting segregation in flowing polydisperse granular materials. *Journal of Fluid Mechanics*, 797:95–109, 2016.

[55] D. V. Khakhar, J. J. McCarthy, and J. M. Ottino. Radial segregation of granular mixtures in rotating cylinders. *Physics of Fluids*, 9(12):3600–3614, 1997.

[56] D. V. Khakhar, J. J. McCarthy, and J. M. Ottino. Mixing and segregation of granular materials in chute flows. *Chaos: An Interdisciplinary Journal of Nonlinear Science*, 9(3):594–610, 1999.

[57] A. Tripathi and D. V. Khakhar. Density difference-driven segregation in a dense granular flow. *Journal of Fluid Mechanics*, 717:643–669, 2013.

[58] Y. Duan, P. B. Umbanhowar, J. M. Ottino, and R. M. Lueptow. Kinetic theory based segregation model for density-bidisperse dense granular flows. *arXiv: Soft Condensed Matter*, pages 1–17, 2019.

[59] S. K. Hajra and D. V. Khakhar. Radial segregation of ternary granular mixtures in rotating cylinders. *Granular Matter*, 13:475–486, 2011.

[60] J. M. N. T. Gray and C. Ancey. Particle-size and -density segregation in granular free-surface flows. *Journal of Fluid Mechanics*, 779:622–668, 2015.

[61] Y. Duan, P. B. Umbanhowar, J. M. Ottino, and R. M. Lueptow. Modelling segregation of bidisperse granular mixtures varying simultaneously in size and density for free surface flows. *Journal of Fluid Mechanics*, 918, 2021.

[62] C. Thornton. *Granular dynamics, contact mechanics and particle system simulations*, volume 24. Springer, 2015.

[63] P. A. Cundall and O. D. L. Strack. A discrete numerical model for granular assemblies. *Geotechnique*, 29(1):47–65, 1979.

[64] A. Di Renzo and F. P. Di Maio. Comparison of contact-force models for the simulation of collisions in DEM-based granular flow codes. *Chemical Engineering Science*, 59(3):525–541, 2004.

[65] N. Bell, Y. Yu, and P. J. Mucha. Particle-based simulation of granular materials. In *Proceedings of the 2005 ACM SIGGRAPH/Eurographics symposium on Computer animation*, pages 77–86, 2005.

[66] J. P. K. Seville and C. Y. Wu. *Particle Technology and Engineering: An Engineer's Guide to Particles and Powders: Fundamentals and Computational Approaches.* Butterworth-Heinemann, 2016.

[67] J. Ai, J. F. Chen, J. M. Rotter, and J. Y. Ooi. Assessment of rolling resistance models in discrete element simulations. *Powder Technology*, 206(3):269–282, 2011.

[68] L. Verlet. Computer experiments on classical fluids. i. thermodynamical properties of lennard-jones molecules. *Physical review*, 159(1):98, 1967.

[69] M. P. Allen and D. J. Tildesley. Chapter 4 molecular dynamics simulations adapted from: “computer simulations of liquids”. 2015.

[70] D. Rozmanov and P. G Kusalik. Robust rotational-velocity-verlet integration methods. *Physical Review E*, 81(5):056706, 2010.

[71] C. Kloss, C. Goniva, A. Hager, S. Amberger, and S. Pirker. Models, algorithms and validation for opensource dem and cfd–dem. *Progress in Computational Fluid Dynamics, an International Journal*, 12(2-3):140–152, 2012.

[72] LIGGGHTS(R)-PUBLIC website. `https://www.cfdem.com`, n.d.

[73] S. Chialvo, J. Sun, and S. Sundaresan. Bridging the rheology of granular flows in three regimes. *Physical Review E - Statistical, Nonlinear, and Soft Matter Physics*, 85(2):1–8, 2012.

[74] O. R. Walton and R. L. Braun. Viscosity, granular-temperature, and stress calculations for shearing assemblies of inelastic, frictional disks. *Journal of Rheology*, 30 (5):949–980, 1986.

[75] K. L. Johnson. *Contact mechanics*. Cambridge university press, 1987.

[76] R. D. Mindlin. Compliance of elastic bodies in contact. *Journal of Applied Mechanics*, 16:259–268, 1949.

[77] A. Di Renzo and P. F. Di Maio. An improved integral non-linear model for the contact of particles in distinct element simulations. *Chemical Engineering Science*, 60(5):1303–1312, 2005.

[78] C. O’Sullivan and J. D. Bray. Selecting a suitable time step for discrete element simulations that use the central difference time integration scheme. *Engineering Computations*, 2004.

[79] M. Babic. Average balance equations for granular materials. *International Journal of Engineering Science*, 35(5):523–548, 1997.

[80] R. Artoni, A. C. Santomaso, and P. Canu. Simulation of dense granular flows: Dynamics of wall stress in silos. *Chemical Engineering Science*, 64(18):4040–4050, 2009.

[81] H. M. Jaeger and S. R. Nagel. Physics of the granular state. *Science*, pages 1523–1531, 1992.

[82] H. M. Jaeger, S. R. Nagel, and R. P. Behringer. Granular solids, liquids, and gases. *Reviews of modern physics*, 68(4):1259, 1996.

[83] G. D. R. MiDi. On dense granular flows. *European Physical Journal E*, 14(4): 341–365, 2004.

[84] T. Barker and J. M.N.T. Gray. Partial regularisation of the incompressible μ(I)-rheology for granular flow. *Journal of Fluid Mechanics*, 828:5–32, 2017.

[85] J. Heyman, R. Delannay, H. Tabuteau, and A. Valance. Compressibility regularizes the μ(I)-rheology for dense granular flows. *Journal of Fluid Mechanics*, 830:553–568, 2017.

[86] D. G. Schaeffer, T. Barker, D. Tsuji, P. Gremaud, M. Shearer, and J. M.N.T. Gray. Constitutive relations for compressible granular flow in the inertial regime. *Journal of Fluid Mechanics*, 874:926–951, 2019.

[87] E. B. Pitman and D. G. Schaeffer. Stability of time dependent compressible granular flow in two dimensions. *Communications on Pure and Applied Mathematics*, 40(4): 421–447, 1987.

[88] P. Jop, Y. Forterre, and O. Pouliquen. A constitutive law for dense granular flows. *Nature*, 441:727–730, 2006.

[89] O. Pouliquen and Y. Forterre. A non-local rheology for dense granular flows. *Philosophical Transactions of the Royal Society A: Mathematical, Physical and Engineering Sciences*, 367(1909):5091–5107, 2009.

[90] J. T. Jenkins and S. B. Savage. A theory for the rapid flow of identical, smooth, nearly elastic, spherical particles. *Journal of Fluid Mechanics*, 130:187–202, 1983.

[91] F. Da Cruz, S. Emam, M. Prochnow, J. N. Roux, and F. Chevoir. Rheophysics of dense granular materials: Discrete simulation of plane shear flows. *Physical Review E*, 72(2), 2005.

[92] Y. Forterre and O. Pouliquen. Flows of dense granular media. *Annual Review of Fluid Mechanics*, 40:1–24, 2008.

[93] B. Andreotti, Y. Forterre, and O. Pouliquen. *Granular media: between fluid and solid*. Cambridge University Press, 2013.

[94] G. I. Tardos, S. McNamara, and I. Talu. Slow and intermediate flow of a frictional bulk powder in the couette geometry. *Powder Technology*, 131(1):23–39, 2003.

[95] O. Pouliquen and Y. Forterre. Friction law for dense granular flows: Application to the motion of a mass down a rough inclined plane. *Journal of Fluid Mechanics*, 453 (2002):133–151, 2002.

[96] J. Rajchenbach. Some remarks on the rheology of dense granular flows. *The European Physical Journal E*, 14(4):367–371, 2004.

[97] P. Jop. Rheological properties of dense granular flows. *Comptes Rendus Physique*, 16(1):62–72, 2015.

[98] B. Yohannes and K. M. Hill. Rheology of dense granular mixtures: Particle-size distributions, boundary conditions, and collisional time scales. *Physical Review E*, 82(6):1–9, 2010.

[99] S. Volpato, R. Artoni, and A. C. Santomaso. Numerical study on the behavior of funnel flow silos with and without inserts through a continuum hydrodynamic approach. *Chemical Engineering Research and Design*, 92(2):256–263, 2014.

[100] P. G. Rognon, J. N. Roux, M. Naaïm, and F. Chevoir. Dense flows of bidisperse assemblies of disks down an inclined plane. *Physics of Fluids*, 19(5):15–19, 2007.

[101] A. Tripathi and D. V. Khakhar. Rheology of binary granular mixtures in the dense flow regime. *Physics of Fluids*, 23:1–12, 2011.

[102] E. Bovet, L. Preziosi, B. Chiaia, and F. Barpi. The Level Set Method Applied to Avalanches. *Proceedings of the European COMSOL conference*, 2007.

Chapter 3

Size segregation in diluted binary mixtures

We begin our investigation by considering the size-driven segregation in a diluted binary mixture. We provide a detailed physical insight into the mechanism of a small isolated particle percolating through a mono-disperse bed of coarse grains when subjected to shear. We then propose a reliable percolation model. The model predictions are compared with experimental data and the model assumptions are verified through DEM simulations.

Parts of this chapter have been published:

S. Volpato, M. Tirapelle, and A. C. Santomaso (2020). Modelling and experimental investigation of shear-induced particle percolation in diluted binary mixtures. *Physical Review E*, 102, 012902, https://doi.org/10.1103/PhysRevE.102.012902.

M. Tirapelle, S. Volpato, and A. C. Santomaso (2021). Shear-induced particle segregation in binary mixtures: Verification of a percolation theory. *Particuology*, 57, 214-222, https://doi.org/10.1016/j.partic.2021.01.005.

3.1 Introduction

When strained in the presence of a gravitational field, small particles drain in a matrix of coarse grains. This phenomenon, which is referred to as percolation, is the primary mechanism for segregation in gravity-driven sheared flows. Percolation was first treated by Bridgwater and co-workers [1–5]. In their work, they evaluated the amount of percolation as a function of cell operating conditions and particle properties, and they addressed the issue of percolation velocity [6]. As shear apparatus, they used a simple shear cell supplied with moving lateral walls that swing backwards and forwards, and that generates heterogeneous zones of shear [7]. Under shear, the shape of the particle bed changes from a rectangle to a parallelogram [1], the particle layers move one over the other for

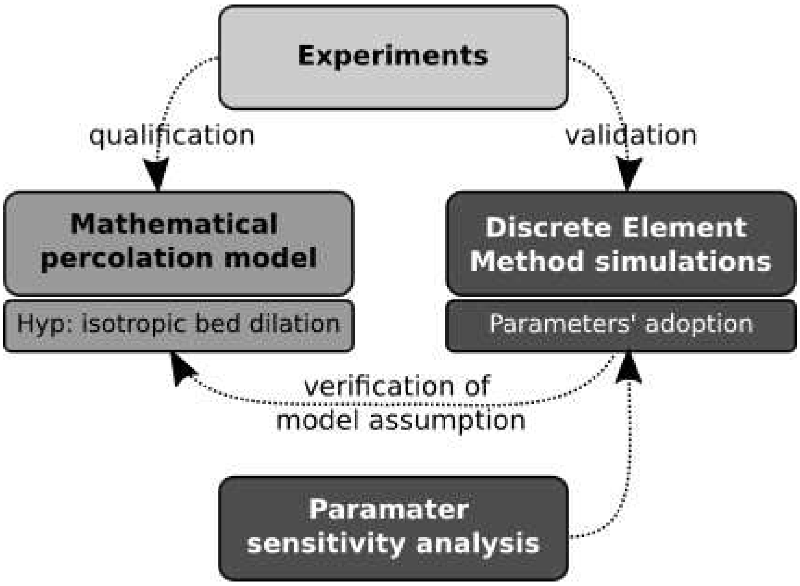

Figure 3.1: The diagram describes the relationship between mathematical model, DEM simulations and reality. After having proposed a mathematical model, we performed both experiments and DEM simulations. The experiments, which represent the real world, allow to qualify the mathematical model and to validate the DEM simulations. Such simulations are then used to verify whether the assumptions of the starting model accurately represent the reality. Note that, the accuracy of the numerical solution is improved by a parameter sensitivity analysis.

convection, the bed dilates, and percolation takes place. They found that the amount of percolation depends mainly on the total strain, rate of strain and diameter ratio of small to large particles [1]. More recently, a similar experimental set-up was used by Johanson et al. [7] to study the effect of small particle concentration on segregation and by van der Vaart et al. [8] to quantify the asymmetric behaviour of small and large particles. The dependence of the percolation velocity on concentrations and kinematics was instead studied in a simulated shear box [9]. Note that, a similar shear box has also been employed in our study.

In what follows, we first propose a simple theoretical model for predicting the percolation behaviour of a fine isolated spherical particle in a shear bed of coarse particles. The model arises from the observation of reality and it is based on statistical considerations and probabilistic assumptions. To demonstrate the predictive capability of the model, we further provide a validation and verification analysis. The validation procedure of the mathematical model is accomplished by comparing the theoretical results with the experimental outcomes. The verification procedure consists in verifying that the model assumptions are reliable. In doing so, we also made use of Discrete Element Method simulations since they allowed us 1) to obtain data that were inaccessible to physical experimentation such as the Voronoi particle dynamics and 2) to perform a rigorous parametric study [10]. A framework of the working procedure is shown in Fig. 3.1.

3.2 Percolation model

For a fine particle to percolate in a bed of coarse particles, two conditions must be met. First, the particle bed must be subjected to shear strain. Under shear, the voids within the bed are continuously renewed and particles can move. In the absence of such a shear, even in the presence of a gravitational field, the particles will remain in their initial positions. The second condition that must be satisfied concerns the size of the voids. More specifically, the voids beneath the percolating particles must be great enough to host such particles. Thus, the first step in developing a percolation model is to investigate the geometrical and topological properties of the void space (e.g. size of the voids, mean particle distance...). Once defined, one can argue about percolation time, travelled space and percolation velocity.

3.2.1 Topology and percolation probability

The size of the voids is strictly related to the mean distance between the particles, $\bar{h}$, which is intended as the average chord length between the surface points of two neighbourhood spheres. For an isotropic and random packing of equal-sized spherical particles having diameter d_c, it has been demonstrated that $\bar{h}$ is a function of the particle diameter, the solid volume fraction ν, and it can be expressed as [11]:

$$\bar{h} = k d_c \frac{\nu}{1-\nu} \, , \tag{3.1}$$

where the parameter k depends upon the geometrical properties of the particle bed. In the case of an isotropic packing of spheres in static conditions, k is equal to 2/3 whereas, k is expected to slightly increase when the particle bed is subjected to shear [12]. For proof refer to Appendix A.1.

As demonstrated by Pavlovitch et al. [13], statistical mechanics provides a relationship for the length distribution function of the distances (or chords) of a random packing of mono-sized particles

$$F(h) = \frac{1}{\bar{h}} \exp\left[-\frac{h}{\bar{h}}\right] \, , \tag{3.2}$$

with $\bar{h}$ being the one defined in Eq. 3.1.

The probability for a fine particle to find an aperture equal or greater than its own diameter ($h \geq d_f$) in one direction is obtained by integrating Eq. 3.2 between d_f and infinity:

$$P(h \geq d_f) = \int_{d_f}^{\infty} F(h) dh = \int_{d_f}^{\infty} \frac{1}{\bar{h}} \exp\left[-\frac{h}{\bar{h}}\right] dh = \exp\left[-\frac{d_f}{\bar{h}}\right] \, . \tag{3.3}$$

However, for the fine particle to percolate through the underlying void, this condition must be satisfied both in the two directions normal to the percolation direction (i.e. x and y) as well as in the parallel one (i.e. z). This is because the void has to be not only large enough but also deep enough to receive the fine percolating particle. The falling probability is therefore given by the composed probability of finding a void greater than d_f in the three spatial directions (i.e. P_x, P_y and P_z). Considering such probabilities as coming from independent events, it can be expressed as:

$$P_f = P(h_x \geq d_f \cap h_y \geq d_f \cap h_z \geq d_f) = \exp\left[-\frac{3}{k}\frac{d_f}{d_c}\frac{\nu}{(1-\nu)}\right] . \tag{3.4}$$

For a complete proof of the derivation of Eq. 3.4 refer to Appendix A.2. Note that, to derive this result, we assumed that the powder bed remains isotropic after expansion even if a directional shear is applied.

To sum up, a fine particle in a gravity-driven sheared flow percolates through a bed of coarse grains when it ran into underlying voids that are great enough to host it. The probability P_f of finding such voids becomes increasingly stronger with the decrease of the diameter ratio: $d^* = d_f/d_c$.

3.2.2 Percolation time

Let us consider a fine particle that lies in a cage composed of coarse particles. As Fig. 3.2 shows, the fine particle may be 1) in motion inside the cage or 2) at rest at the bottom of the cage. If it is at rest, the particle will fall again when the renewal of the bed generates an underlying void large enough to percolate through. The percolation process is therefore a discontinuous process characterized by the alternation of stop and go events. The discontinuity of the process is even more evident for coarser percolating particles.

To determine the total percolation time required for a particle to travel through the cage, both the times of stopping and falling must be considered. The time of stopping, t_s, is proportional to the size of the coarse particles, which represents the length scale of the system, and inversely proportional to the relative velocity between two layers of coarse particles, namely $v_c = \dot{\gamma} d_c$. The time of stopping results therefore proportional to:

$$t_s \propto \frac{d_c}{\dot{\gamma} d_c} . \tag{3.5}$$

In turn, the time of falling must be proportional to the square root of the ratio between the distance travelled by the fine percolating particle (i.e. $d_c - d_f$) and the acceleration of gravity:

$$t_f \propto \sqrt{\frac{d_c - d_f}{g}} . \tag{3.6}$$

This relation arises from an elementary energy balance considering that all the potential energy of the particle is converted into kinetic energy (i.e. the dissipation due to contact friction is neglected).

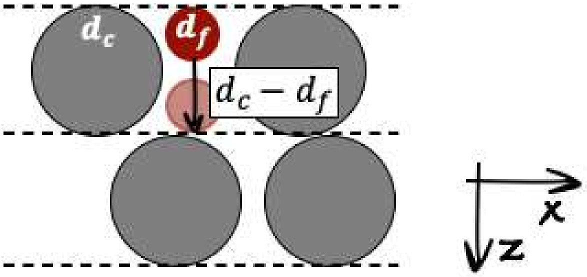

Figure 3.2: Schematic representation of the cage used to describe the percolation mechanism.

3.2.3 Percolation velocity

To model the averaged percolation velocity of a fine isolated spherical particle, we considered the contribution of kinetic sieving and we disregarded the contribution of squeeze expulsion. We believe that squeeze expulsion affects minimally the overall percolation velocity when dealing with diluted binary systems in the absence of significant density differences [14].

Using the previous definitions for the percolation time, the averaged fine percolation velocity can be written as:

$$v_p \propto \frac{(d_c - d_f) \cdot P_f + 0 \cdot (1 - P_f)}{P_f \cdot t_f + (1 - P_f) \cdot t_s} \,, \tag{3.7}$$

where the numerator represents the averaged space travelled by several fine particles. This space is equal to $d_c - d_f$ when the fine particles fall within the cage, or to zero when they are at rest. The two contributions are weighed by the fraction of fines that, at each instant, meet the conditions for falling or staying. For what concerns the denominator, it represents the average percolation time, which is the sum of the falling and stopping times, again weighted by the corresponding occurrence probabilities. Introducing Eqs. 3.5 and 3.6 into Eq. 3.7 yields:

$$v_p \propto \frac{d_c \cdot \dot{\gamma} \cdot P_f \cdot (1 - \frac{d_f}{d_c})}{P_f \cdot \dot{\gamma} \cdot \sqrt{\dfrac{d_c \cdot (1 - \frac{d_f}{d_c})}{g}} + (1 - P_f)} \,. \tag{3.8}$$

As expected, the percolation velocity is a function of the local shear rate, the characteristic size of the particle bed and the falling probability. Furthermore, this formulation satisfies the zero flux condition for the limiting case $d_f = d_c$. By introducing the following three dimensionless groups (i.e. dimensionless velocity v_p^*, dimensionless shear rate $\dot{\gamma}^*$ and size ratio d^*):

$$v_p^* = \frac{v_p}{\dot{\gamma} d_c},\ \dot{\gamma}^* = \dot{\gamma}\sqrt{\frac{d_c}{g}},\ d^* = \frac{d_f}{d_c}\,, \tag{3.9}$$

the percolation velocity becomes, in the dimensionless form:

$$v_p^* = \frac{A \cdot (1 - d^*) \cdot P_f}{P_f \cdot \dot{\gamma}^* \sqrt{1 - d^*} + (1 - P_f)}\,, \tag{3.10}$$

where A is a proportionality parameter expected to be dependent on the material properties [12, 15, 16].

From the physics of the phenomenon, we expect that the time of falling does not significantly affect the percolation time since the falling is a much more rapid event than the stopping. An a posteriori estimation of these times showed indeed that the time of stopping is two orders of magnitude larger than the time of falling. Given this, Eq. 3.10 can be simplified to:

$$v_p^* = A \cdot (1 - d^*) \cdot \frac{P_f}{(1 - P_f)}\,. \tag{3.11}$$

Notice that the above equation bears similarities to the one proposed by Bertuola et al. [17] for predicting the percolation velocity of fine particles during hopper discharge:

$$v_p^* = A \cdot (1 - d^*) \cdot (1 - \phi_f)\,. \tag{3.12}$$

Unlike Eq. 3.11, this equation accounts for the effect of the concentration of the fine particles ϕ_f, a contribution that disappears at infinite fine particles dilution ($\phi_f \to 0$). However, Eq. 3.11 adds the probabilistic term as a substantial improvement of Bertuola et al.'s model [17].

3.3 Experimental campaign

To accomplish model validation, we performed an experimental campaign. The experiments were designed to test the model capability for a range of shear rates and diameter ratios.

3.3.1 Materials and methods

The experiments are performed in a simple shear box that bears several similarities with the shear cell used by Scott and Bridgwater [1]. It consists of two fixed sidewalls and two wooden tilting sidewalls hinged at the bottom of the box. These can tilt backwards and forwards up to 45° of inclination. This inclination ensures the complete renewal of the neighbouring particles belonging to two adjacent layers when sheared. The bottom wall consists of a transparent bumpy glass bottom. The bumpiness, which is made of polymeric hemispheres glued in random positions, prevents the development of the hexagonal close-packing. To prevent the formation of a dead zone close to the bottom, the bottom wall was also raised (this ensure a small, but not null, momentum to the bottom layer of particles). Unlike Scott and Bridgwater's shear box, our setup is not confined on top. To reduce the undesired convective re-circulation loops affecting the upper layer of an unconfined granular bed, a mobile rack with baffles penetrate the free surface.

The shear box is 0.2 m deep, 0.2 m high and the distance between the tilting walls is 0.1 m wide. We defined the coordinate system in such a way that width and depth are oriented along the x and y axes, whereas the gravitational acceleration acts along z. Fig. 3.3 shows a schematic representation of the shear cell.

We employed binary mixtures of fine and coarse particles in dilute conditions: the fine particles were few in number compared with the coarse particles ($\sim$ 1:3000). At the beginning of each experiment, we first filled the shear box with the coarse particles ($d_c = 6$ mm) up to a height of 60 mm. We then deposited, on the surface of the bed and at a regular distance from each other, six fine tracer particles with diameters d_f varying from 1.5 mm to 3.3 mm. We loaded a further layer of coarse particles until a total bed height of 100 mm was reached. This prevents the fines particles to remain trapped into the convective recirculation loops that typically develop close to the free surface. After filling, the system was subjected to shear: the mobile walls were pushed forward and back by hand at three different constant linear velocities corresponding to the following tilting frequencies: $f = 17$, 26, 35 rpm; and hence, the following shear rates: $\dot{\gamma} = 0.57$, 0.87, 1.17 1/s. Because of the shear rate, which is calculated as:

$$\dot{\gamma} = 2 \cdot f \cdot \tan(\alpha_{max}) \,, \tag{3.13}$$

the fine particles percolated toward the bottom of the shear box.

The percolating particles cannot be detected until they reach the bottom transparent wall. The evolution of the bottom layer of the granular bed was recorded with a digital camera. The time elapsed between the start of the shearing action and the arrival time at the glass bottom of each tracer particle represents the percolation time. The (average) percolation velocity of each percolating particle is the ratio between the distance travelled by the particle (i.e. $\bar{s} = 60$ mm) and the average residence time $\bar{t}$ corrected by its variance σ^2:

$$v_m = \frac{\bar{s}}{\bar{t}} \left(1 + \frac{\sigma^2}{\bar{t}^2} \right) \,. \tag{3.14}$$

Note that all the experiments were performed in the so-called *slow-frictional regime*, which is typical of granular flows in dense and confined conditions (such as those occurring in silos or hoppers far from the outlet).

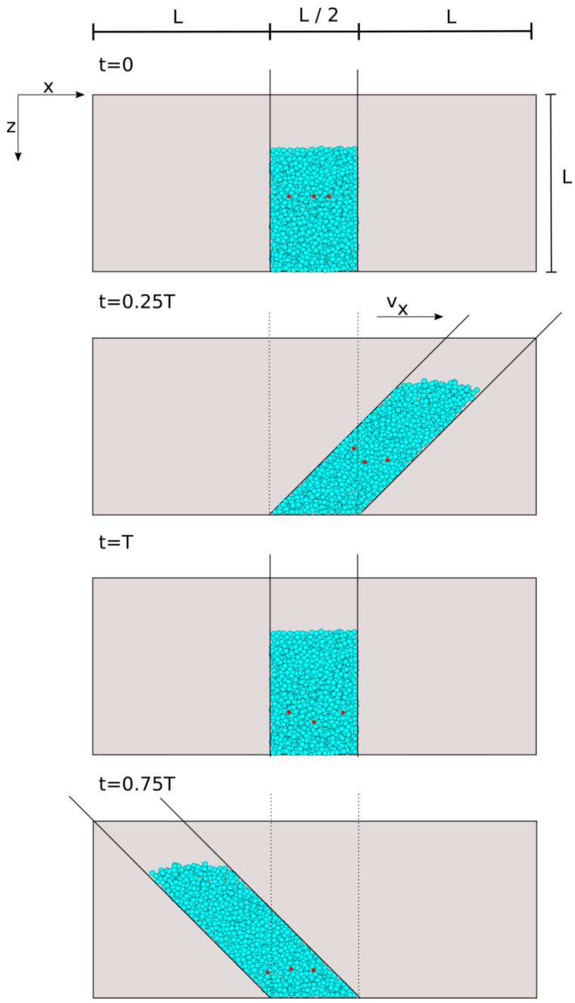

Figure 3.3: Schematic diagram of the experimental apparatus with the coordinate system. The four possible positions of the shear box are shown with the indication of the time t (starting from 0) after which the position is achieved. The time is expressed as a function of the period T equal to the reciprocal of the frequency. The max inclination angle is 45^o.

3.3.2 Results and discussion

The results reported in this section refer to a range of diameter ratios and a range of shear rates. For each experimental condition, the error bars represent the standard deviation of fifteen independent measurements.

Fig. 3.4 shows the residence time of the fine percolating particles as a function of the dimensionless particle size for the three shear rates tested. For same-sized percolating particles, the residence time decreases with the increase of the shear rate because of the more frequent generation of voids. On the other hand, the residence time increases with the size ratio: larger percolating particles remain trapped for longer under the same shearing action. The residence time approaches zero for $d^* \to 0$ since tracers particles can percolate almost undisturbed throughout the particle bed and without ever stopping.

The percolation model in Section 3.2 predicts a linear dependence of the percolation

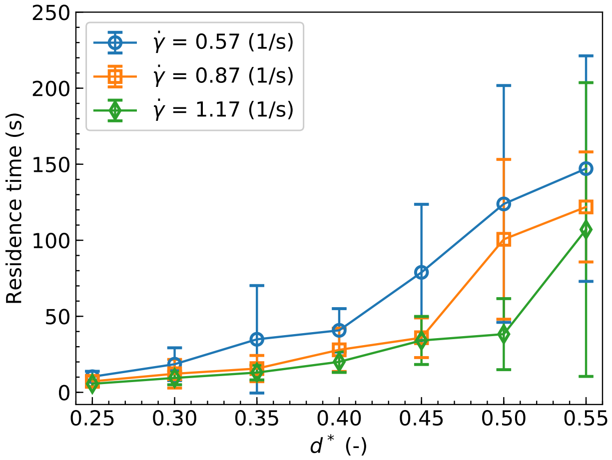

Figure 3.4: The experimental residence time of fine particles is plotted against d^* at different shear rates. The error bars represent the standard deviation of fifteen independent measurements.

velocity on the shear rate and a more complex dependence on the size ratio, which is modulated by the probability term. Fig. 3.5 confirms that v_p varies almost linearly with the shear rate, whereas Fig. 3.6 proves that v_p decreases exponentially with the size ratio. Thus, the percolation model qualitatively agrees with experimental evidence.

The model is validated quantitatively against experimental data. Fig. 3.7 shows the percolation velocity in dimensionless form as a function of d^* for the three shear rates. The experimental data (black squares) are fitted with Eq. 3.11 by using the least-squares minimization method (solid line). The optimal values for the model parameters are: $A = 9.7$ and $k = 0.71$. For a static and isotropic bed, k should be equal to 2/3. In our case, k is slightly greater because of the shear. Independently by the shear rate applied, all data collapse on the same master curve confirming that the dimensionless velocity is independent of the shear rate.

Under shear, the particle bed is dilated with respect to its initial state. If in the static condition the porosity is estimated to be equal to 0.39, the porosity of the sheared bed is equal to 0.40. These estimations were done from data of particle true density, which was measured by liquid picnometry, and bulk density, which was measured with the funnel flow method [18]. Fig. 3.8 shows the comparison of the probabilities P_f (see Eq. 3.4) for the static case (k=2/3, ε=0.39) and the sheared case (k=0.71, ε=0.4). It is clear that, there exists a relative increase of P_f when a shearing action is applied. The inset of Fig. 3.8 shows that the increase δ rises with d^*. In particular, we get that $\delta \sim 19\%$ for $d^* = 0.25$ and $\delta \sim 47\%$ for $d^* = 0.55$. As expected, the action of the shear rate has little influence on the percolation velocity when the size ratio is small, but it becomes significant for larger size ratios.

We can conclude that the percolation model is suitable for predicting the segregation behaviour of a fine isolated particle in a gravity-driven shear flow. The model is qualified

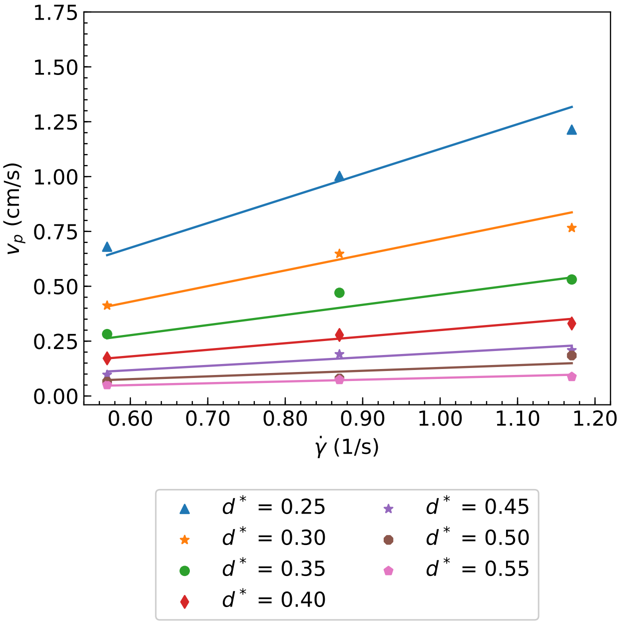

Figure 3.5: Percolation velocity against the shear rate at seven different size ratios.

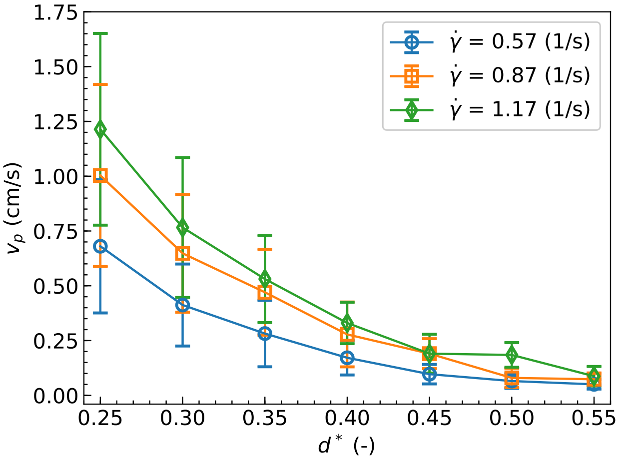

Figure 3.6: Percolation velocity against the size ratio at three different shear rates. The error bars represent the standard deviation of fifteen independent measurements.

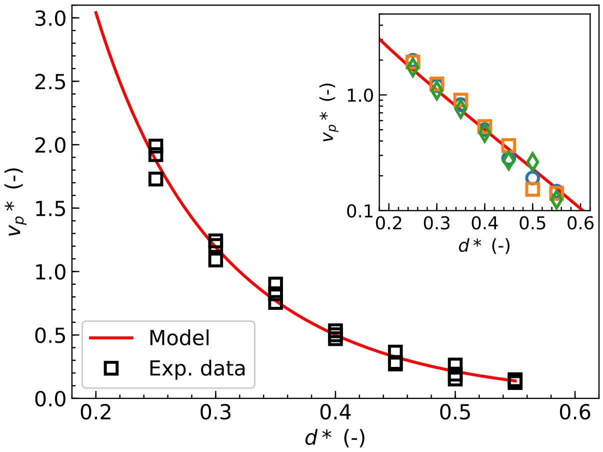

Figure 3.7: Dimensionless percolation velocity against the size ratio. The squares represent the experimental data, whereas the solid line represents the model outcome. Inset: semi-logarithmic plot of the dimensionless percolation velocity obtained from data (squares) and model (solid line).

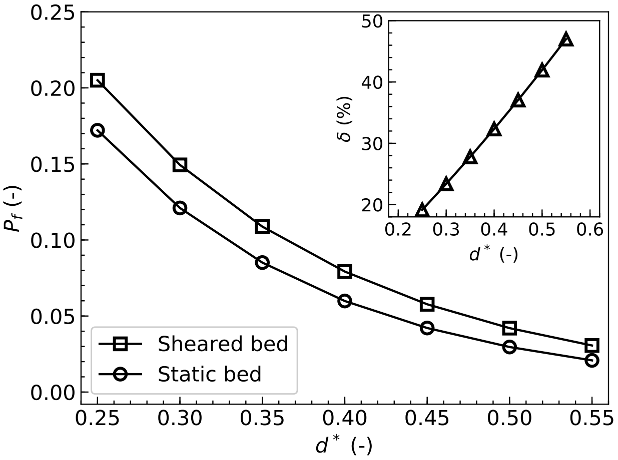

Figure 3.8: Estimated falling probability of a fine particle, determined as the probability of finding a void greater than d_f in x, y and z directions, as a function of the size ratio. The curves are obtained from Eq. 3.4, using $\varepsilon = 0.39$ and $k = 2/3$ for the static bed and $\varepsilon = 0.4$ and $k = 0.71$ for the sheared bed.

by experimental evidence, however, to increase the significance of the model, in what follow we verify the reliability of the model assumptions.

3.4 DEM simulations

In this section, we provide discrete element simulations of the shear box. We investigate a wide range of model parameters to determine what are the parameters that mostly affect the percolation behaviour of a fine particle. We tuned the simulation parameters by means of comparison with experimental findings.

3.4.1 Simulation setup

The DEM simulations were carried out using LIGGGHTS® PUBLIC [19, 20]. We employed the non-linear spring-dashpot contact model based on the Hertz and Mindlin' theory with Constant Directional Torque rolling friction (see Section 2.2.1.2). Since we could not experimentally measure all the material properties (e.g. Young's modulus, friction coefficients...), we performed a parameter sensitivity analysis.

The simulated geometry consists of a three-dimensional shear box having the same dimensions as the real system. We bound the simulation domain with frictional walls so that all the particles can interact with the walls. The tilting sidewalls can rotate backwards and forward up to 45° while remaining parallel to each other. To produce a constant shear rate (i.e. $\dot{\gamma} \equiv v(h)/h = const$), we imposed the following angular velocity, ω:

$$\omega(t) = \frac{\arctan(\dot{\gamma} \cdot t)}{t}\,, \tag{3.15}$$

with $0 < t < t(45^\circ)$. It is worth noticing that, despite the shear rate being held constant throughout most of the forward and backward movement, transients necessarily occur during the direction reversal [9]. Our simulated shear box is different from the others simulated in the literature: unlike in van der Vaart et al. [8], we applied constant strain rates and unlike Khola and Wassgren [9], our walls were frictional and our boundaries were non-periodic. These choices were done in order to perfectly mimic the experimental shear box.

3.4.2 Particle properties and input parameters

The cell was filled with spherical glass beads assumed to be monodisperse and cohesionless, up to a bed height of 16 cm. The bed of coarse particles was generated within the cell and let settle by gravity. To prevent the development of the regular hexagonal close packing close to the bottom [1], the first layer of particles presented a polydisperse size distribution (Gaussian distribution with $\mu = 6$ mm and $\sigma = 0.15 \cdot \mu$. The standard deviation is big enough to avoid regular packing, but it likewise ensures that the particles in the bed are

Variable	**Symbol**	**Value**
Particle density (kg/m^3)	ρ_s	2540
Young's modulus (MPa)	E	26
Poisson ratio	σ	0.25
Sliding friction coefficient	μ_s	0.18
Rolling friction coefficient	μ_r	0.005
Wall-particle friction	μ_{wp}	0.18
Restitution coefficient	e_n	0.60
Coarsest particle diameter (m)	d_c	0.006
Diameter ratio	d_f/d_c	0.25-0.55
Number of particles	N_T	> 16000
Time step (s)	Δt	$< 1x10^{-5}$
Shear rate (s^{-1})	$\dot{\gamma}$	0.567-1.167
Boundary conditions	$-$	f f f

Table 3.1: A summary of the DEM simulation parameters of the standard case.

always larger than the tracer particles). All the other grains had a diameter equal to 6 mm. The fine percolating particles were successively inserted by randomly replacing some of the coarse grains. The fine particles were positioned at a constant distance from the bottom ($10 \cdot d_c$), spaced apart to ensure diluted conditions (i.e. few fines in a bed of coarse particles), and far enough (at least 2 d_c far) from the sidewalls to minimize any wall influence. Both bulk particles and percolating particles had the same density of 2540 kg/m^3. The total amount of grains in each simulation was around 16000.

The material properties and the simulation parameters of the standard case are summarized in Table 3.1. All properties are typical of glass beads, except for the elastic Young's modulus. The Young's modulus E was set of the order of magnitude of MPa instead of GPa. This reduces the computational time without significantly affecting flow patterns, velocity profiles, shear stresses [20, 21]. Furthermore, it does not result in a significant error in the structural analysis [22]. As concern the wall-particle friction coefficient, it was imposed equal to 0.18 regardless of the type of materials in contact since we measured $\mu_{wp} \approx 0.17 \pm 0.01$ for wood-glass interactions and $\mu_{wp} \approx 0.19 \pm 0.01$ for glass-glass interactions.

The numerical time step was chosen to be at least 20% lower than the Rayleigh time. In particular, we imposed $\Delta T = 0.5 \cdot 10^{-5}$ s for $d^* = 0.25 - 0.30$ and $\Delta T = 1.0 \cdot 10^{-5}$ s in all the other cases.

3.4.3 Results and discussion

3.4.3.1 Parameter tuning

To have realistic simulation results, the parameters must be calibrated. However, calibration has a problem of ambiguity of the parameters' selection [23]. Furthermore, it is difficult to obtain all the parameters by physical experiments. Therefore, we performed a parameter sensitivity analysis. This study was done by systematically changing the mechanical properties of glass beads and evaluating their impact on the percolation velocity, considering different size ratios and 26 rpm as tilting frequency. Once the percolation velocities were evaluated, a response surface regression was made for each parameter. Note that the effect of the mutual interaction of the parameters has not been studied.

The coefficient of rolling friction is usually added to mimic the behaviour of not perfectly spherical particles. Here, we varied the rolling friction in the range of 0.005-0.100 which approximately match the one of the glass beads. As Fig. 3.9-a shows, the rolling friction has no drastic influence on the percolation velocity. Neither Young's modulus in the range of $1 \cdot 10^7$-$5 \cdot 10^7$ Pa, nor the coefficient of restitution, which was varied in between 0.4 and 0.8, have a significant impact on the results (see Fig. 3.9-b,c). The same conclusion can be drawn also for the variations of the Poisson ratio from 0.20 to 0.30. (Fig. 3.9-d). According to these simulations, the shape and the mechanical properties of the material have minimal influence on the percolating velocity. In each case indeed, it appears from response surface regression with backwards elimination that the response variable (namely the dimensionless percolation velocity) depends quadratically on the size ratio but it is independent on the parameter under consideration.

What strongly influence the granular behaviour of the system are the frictional properties. As Fig. 3.10 shows, higher frictional coefficients determine an increase in the percolation velocity. In this case, the response has a statistically significant dependence on both sliding friction coefficient, size ratio and their interaction:

$$v_p^* = 8.63 - 34.18d^* + 5.09\mu_s + 35.33d^{*2} - 10.33d^*\mu_s \,. \tag{3.16}$$

The standard deviation of the data points around the fitted values, which is equal to 0.20 (in dimensionless units since v_p^* is dimensionless), and $R^2 = 96.5\%$ ensure the reliability of the model. Fig. 3.11 represents the corresponding contour map. It is interesting to see that for a fixed d^* the percolation velocity increases with friction. Despite this result can be counter-intuitive at a first sight, different explanations can be found in the literature. According to Remy et al. [21], this is due to an increase in the granular temperature with associated an increase in diffusive mixing. For Jing et al. [24], the increase of interparticle friction promotes the upward migration of large particles and hence, the creation of voids that are easily filled by adjacent fines [25]. According to us, the effect of friction on the percolation process is likely related to changes in the packing structure of the bed

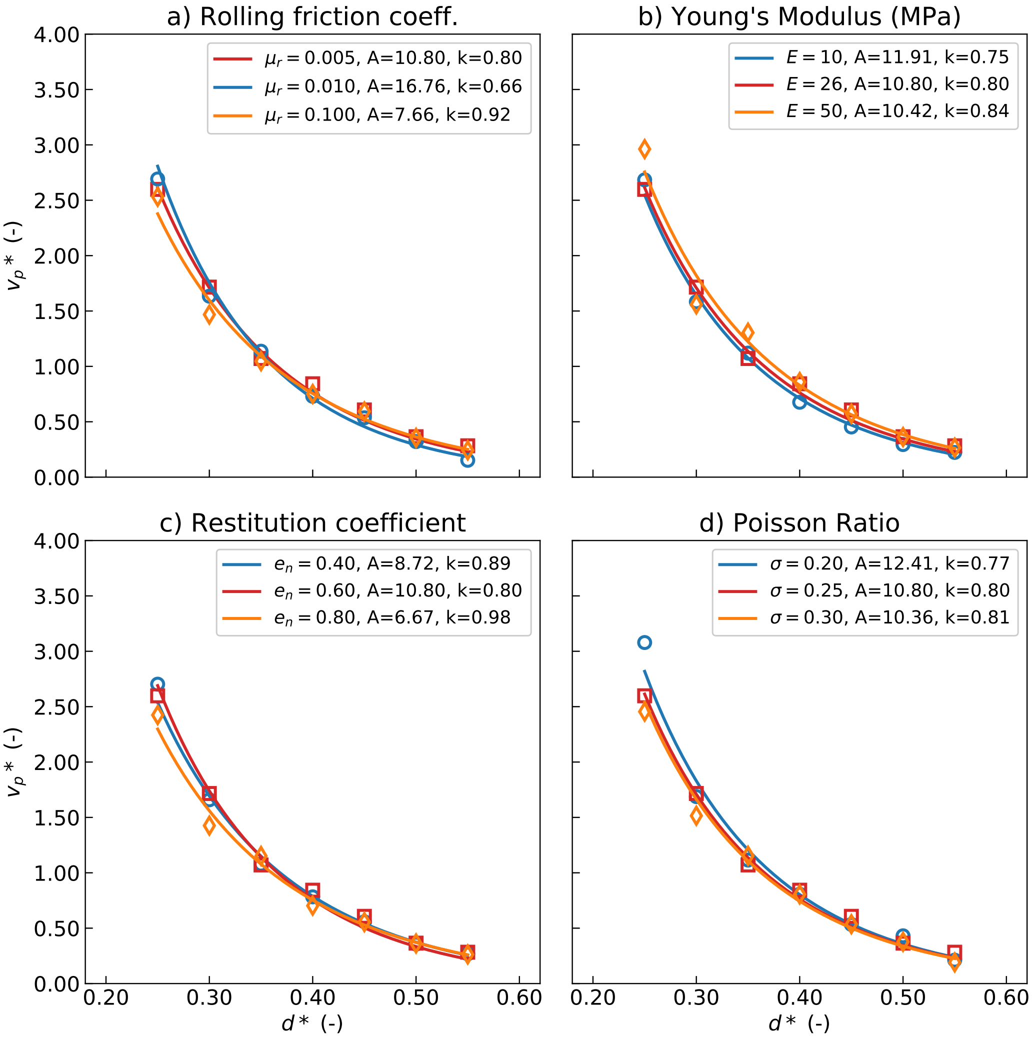

Figure 3.9: Dimensionless percolation velocity as a function of the size ratio in the case of 26 rpm tilting frequency and for different values of (a) rolling friction, (b) Young's modulus, (c) restitution coefficient and (d) Poisson ratio.

subjected to shear. To verify this hypothesis, we performed dedicated simulations and measured the bed porosity as a function of the sliding friction coefficient. Fig. 3.12 shows an increase of the bulk porosity with increasing the friction coefficient. The lower mobility of the coarse particles due to the increased friction at the contact points determines a less efficient packing during the bed deposition and also during the shearing action. According to Eq. 3.4, this implies a larger probability P_f and hence, a larger percolation velocity. Clearly, the sliding friction coefficient is the only parameter that requires accurate tuning. We set $\mu_s = 0.18$. The adoption of $\mu_s = 0.18$ is justified both from direct experimental measurements ($\mu_s = 0.19 \pm 0.01$) and because $\mu_s = 0.18$ corresponds exactly to the estimated bulk porosity of $\varepsilon = 0.40$ (see Fig. 3.12).

The effect of changes in packing quality can also be observed in Fig. 3.13 that reports

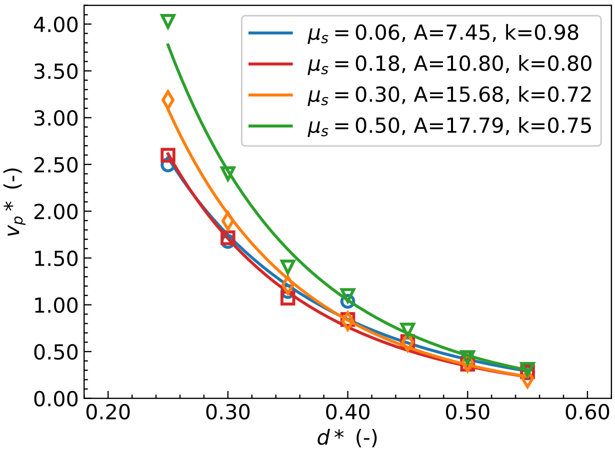

Figure 3.10: Effect of changes in sliding friction coefficient on the percolation velocity. The tilting frequency used is 26 rpm.

the trends of the parameters A and k (present in Eq. 3.4) as a function of bed porosity. k is not significantly affected by the average bed porosity and, except for the lowest value, which corresponds to a very low inter-particle friction (Fig. 3.12), it tends to a constant value. This is also physically accurate because k is a geometrical parameter and hence expected to be more affected by some shear-induced anisotropy rather than changes in the average bed porosity. On the other hand, the parameter A increases linearly with porosity, suggesting the existence of a relationship between A and the average distance between the particles. This effect is already incorporated into the probability term (Eq. 3.4) and hence, we suggest a dependence of A on inter-particle friction mediated by the bulk porosity. This is also shown in Fig. 3.10 where we observe a monotonic increase of A with the inter-particle friction coefficient (i.e. with a porosity increment). A larger distance between particles increases the falling distance and therefore increases the overall percolation velocity.

3.4.3.2 Percolation velocities

A full factorial design of simulations was performed for the following size ratios: $d^* = d_f/d_c$=0.25, 0.30, 0.35, 0.40, 0.45, 0.50, 0.55 and for the following three different tilting frequencies: 17, 26 and 35 rpm. A total of 21 combinations were simulated. The average percolation velocity (i.e. the response variable) was calculated for each run as:

$$v_p = \frac{1}{N}\sum_{j=1}^{N} v_{p,j} \,, \tag{3.17}$$

where $v_{p,j}$ is the percolation rate of the *j-th* particle to cross the cell and N is the number of fine percolating grains. N was 32 for $d^* = 0.20, 0.25, 0.30$, and 16 for all the other cases.

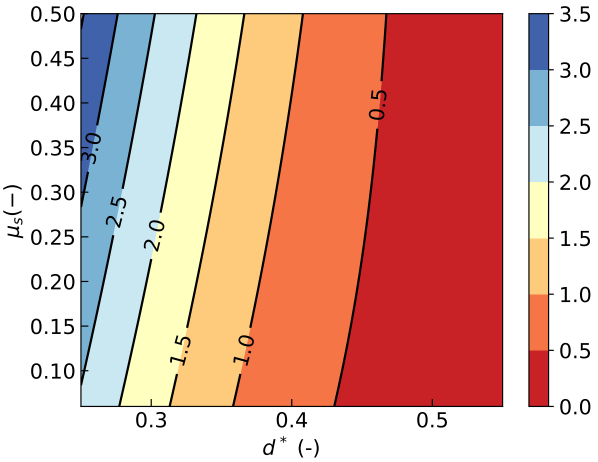

Figure 3.11: Contour plot of dimensionless percolation velocity versus size ratio and friction coefficient.

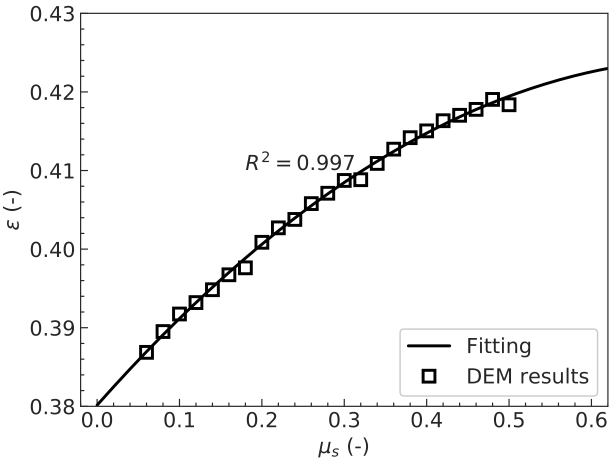

Figure 3.12: Porosity as a function of the coefficient of sliding friction.

Fig. 3.14 shows the velocity profile as a function of size ratio for each tested shear rate when using the parameters listed in Table 3.1 (remind that the reliability of these parameters has been proved in §3.4.3.1). The error bars represent the standard deviation of 16 or 32 independent measurements, which becomes larger for smaller percolating particles. As expected, the percolation velocity significantly decreases for size ratios tending to 1 (at 5% significance level). On the other hand, smaller percolating particles has a higher number of opportunities to find a void bigger than themselves. The percolation velocity is then larger at high shear rates. In the inset, the same data are represented in terms of dimensionless percolation velocity. All data collapse on the same curve since the dimensionless percolation velocity is independent of the shear rate.

In Fig. 3.15 the simulated dimensionless velocities are fitted with the mathematical

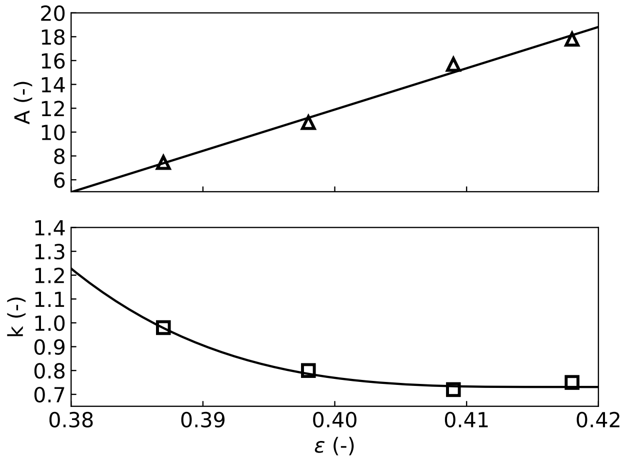

Figure 3.13: The parameters A (on the left axis) and k (on the right axis) are plotted as a function of the bed porosity.

model presented in Section 3.2.3 by using the Least-squares minimization (in detail, the Trust Region Reflective minimization algorithm of the SciPy library [26]). The optimal values found for the parameters, considering $\varepsilon = 0.40$, are: $A = 10.80$ and $k = 0.80$. The latter suggests that, as the size ratio approaches 0.80, the percolation becomes negligible (the velocity profile converges to 0). It should be noted that $k = 0.80$ is slightly larger than 2/3, the typical value that characterizes isotropic static beds. The root-mean-square deviation (RMSD) between predicted and observed values is 0.133, showing a good quality of the fitting.

If we compare the fitting parameters, we can see that the numerical results agree with the experiments. The numerical model is therefore valid and can be used to accurately predict percolation in sheared systems with dilute fines concentration in the range of the explored shear rates.

3.4.3.3 Packing structure characterisation

The mathematical model (3.4) shows that the packing structure plays an important role in the percolation velocity: the probability P_f is indeed a function of both local porosity ε and bed stereo-geometry k. It is therefore important to characterize the internal packing structure of the granular bed.

The bed porosity was computed by using the tessellation method based on the 3D generalization of the Voronoi diagrams. By definition, a Voronoi cell around a particle is the region of space that is much closer to that particle than to any other particle in the system [27, 28]. Thus, the Voronoi tessellation divides the space into regular polyhedra with flat faces and straight edges and allows the local porosity to be calculated as:

$$\varepsilon_l = \frac{V_{Voro} - V_p}{V_{Voro}}\,. \tag{3.18}$$

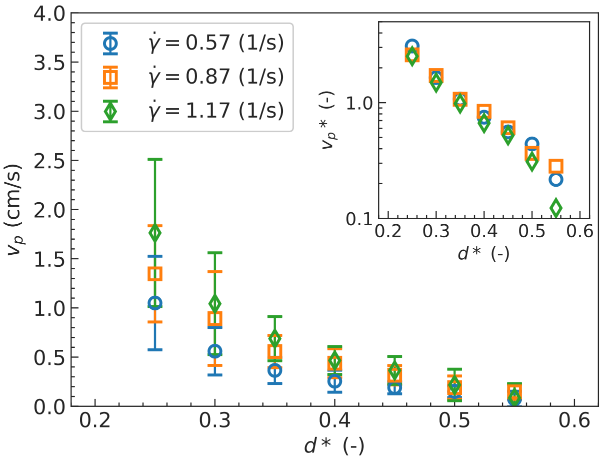

Figure 3.14: Percolation velocity as a function of the size ratio for three different frequencies of tilting: 17, 26 and 35 rpm. In the inset, the dimensionless percolation velocities are reported.

In Eq. 3.18, V_{Voro} and V_p are respectively the volume of the tessellation containing the *i-th* particle and the volume of the particle itself. The latter was known, whereas V_{Voro} was computed in LIGGGHTS®-PUBLIC by using Voro++, an open-source software library [29].

In Fig. 3.16 the density distribution and the cumulative distribution of the local porosities are reported both in static and sheared conditions. The packing condition varies after the application of the shear: the bed porosity slightly decreases from an initial median value of 0.42 to 0.40 indicating a contraction (settling) of the bed under shear. Note that the medians are more representative than the means because less biased by the outliers. The second peak of the distributions is indeed due to the over-relaxation of the bed close to the walls while the peak at ε=1 refers to the particles at the free surface of the bed. Both these peaks are not representative of the bulk. The porosity $\varepsilon = 0.40$, which was used in the mathematical model for fitting the simulation data (Fig. 3.15), is therefore justified and in agreement with the experimental findings.

The porosity estimated from the Voronoi tessellation is a volumetric porosity that does not provide any information about the isotropic or anisotropic nature of the packing of spheres [30]. Because an anisotropic packing bed could affect the percolation process, and because the model rests on the hypothesis of perfect isotropy of the bed, the structure of our bed of coarse glass beads was studied in detail. To establish if there was anisotropy, a cubic region of edge length 8 cm within the powder bed was considered. For visual reference, Fig. 3.17 shows three examples of 2-D cross-sections orthogonal to the x, y and z directions. The porosity characteristics of XY, XZ, and YZ planes is calculated as the ratio between the empty spaces (white pixel) and the area of the whole cross-section. To calculate a porosity distribution for each of the three directions, the porosity was estimated on a hundred slices along any direction. In Fig. 3.18 the respective boxplots are shown.

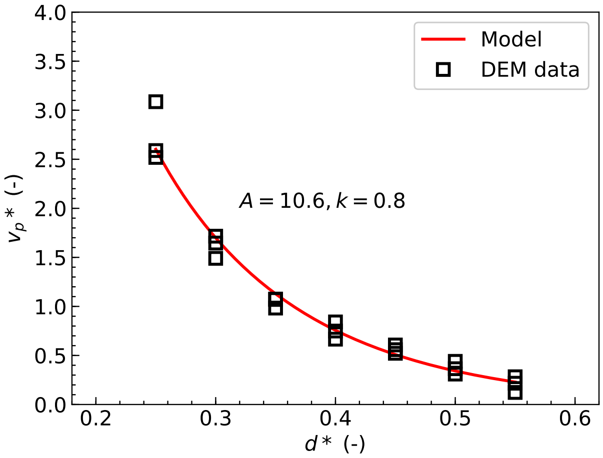

Figure 3.15: Fitting of the numerical data with the mathematical model proposed by Volpato et al. [15].

Unlike along x and y directions, the porosity along z spreads over a wider range and some outliers appear. However, as detailed below, this difference is not statistically significant.

The assumption of isotropic packing structure on which Eq. 3.4 relies is justified below using statistics. Firstly, Bartlett's test of equality of variances was performed at the 0.05 significance level. Because the p-value is less than the significance level, the hypothesis of equal variances has to be rejected: a statistically significant difference exists between the variances of at least two independent sets of our normally distributed continuous data. For testing the equality of the porosity in the three directions, a one-way ANOVA F-test statistics scheme was applied assuming no equal variances. Because the p-value=0.721 is greater than the significance level of 5%, there are no statistically significant differences between the means. We can therefore conclude that the mean porosity is the same in all three directions and hence, the assumption of isotropic bed under shear conditions is justified.

3.5 Conclusions

We developed a percolation model for a small isolated particle in a gravity-driven shear flow of coarse grains. In developing the model, we assumed that the particle bed dilates isotropically when subjected to shear. The model captures, in a three-way comparison, both experimental and DEM results.

To qualify the model, we performed an experimental campaign for a range of size ratios and a range of shear rates that are characteristic of the quasi-static regime of flow [31], namely until dimensionless shear rates of 0.15–0.20. As expected, the percolation speed decreases exponentially when the particle size ratio increases; furthermore it is linearly dependent on the shear rate, at least for the quasi-static regime of flow. The experimental

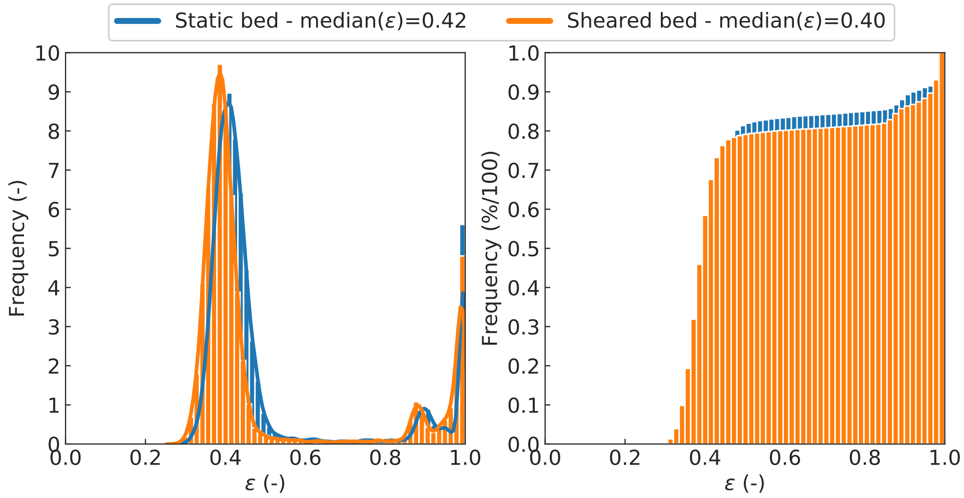

Figure 3.16: Distribution (on the left) and cumulative distribution (on the right) of the bed porosity in static (blue bars) and sheared condition (orange bars).

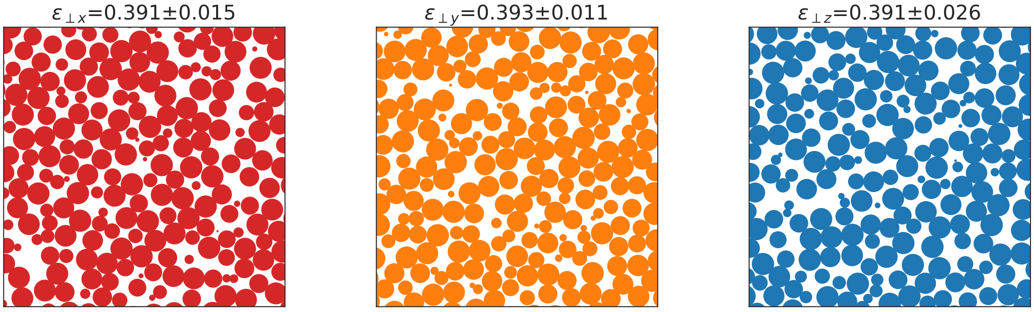

Figure 3.17: Orthogonal slices for 3D visualisation of the pore structure.

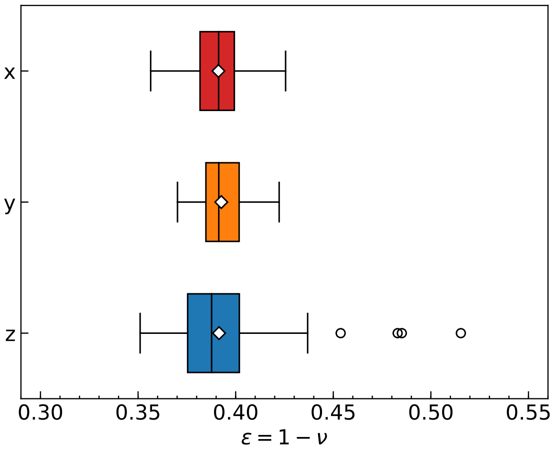

Figure 3.18: The boxplots of the bed porosity along the three directions: x, y and z.

data are well fitted by the model for $A = 9.7$ and $k = 0.71$.

To verify the hypothesis on which the model relies, we performed DEM simulations. We found that, in sheared conditions, the pack of grains is almost isotropic with volumetric median porosity of 0.40 and friction coefficient equals to $\mu_s = 0.18$. Also, the parameters A and k are in close agreement with the experimental ones. This suggests that the percolation theory relies on physically consistent assumptions and meaningful parameters. Thus, the model can be successfully used as a closure relation for the continuum modelling of segregation in granular flows, analogously to what was done in Bertuola et al. [17].

Bibliography

[1] A. M. Scott and J. Bridgwater. Interparticle percolation: a fundamental solids mixing mechanism. *Industrial & Engineering Chemistry Fundamentals*, 14(1):22–27, 1975.

[2] J. Bridgwater, M. H. Cooke, and A. M. Scott. Interparticle percolation: equipment development and mean percolation velocities. *Transactions of the Institution of Chemical Engineers*, 56:157—167, 1978.

[3] M. H. Cooke and J. Bridgewater. Interparticle percolation: a statistical mechanical interpretation. *Industrial & Engineering Chemistry Fundamentals*, 18(1):25–27, 1979.

[4] J. Bridgwater, W. S. Foo, and D.J. Stephens. Particle Mixing and Segregation in Failure Zones - Theory and Experiment. *Powder Technology*, 41:147–158, 1985.

[5] J. Bridgwater. Mixing and segregation mechanisms in particle flow. In *Granular matter*, pages 161–193. Springer, 1994.

[6] Julio M. Ottino and D. V. Khakhar. Mixing and segregation of granular materials. *Annu. Rev. Fluid Mech*, pages 55–91, 2000.

[7] K. Johanson, C. Eckert, D. Ghose, M. Djomlija, and M. Hubert. Quantitative measurement of particle segregation mechanisms. *Powder Technology*, page 12, 2005.

[8] K. van der Vaart, P. Gajjar, G. Epely-Chauvin, N. Andreini, J. M. N. T. Gray, and C. Ancey. Underlying asymmetry within particle size segregation. *Physical review letters*, 114(23):238001, 2015.

[9] N. Khola and C. Wassgren. Correlations for shear-induced percolation segregation in granular shear flows. *Powder technology*, 288:441–452, 2016.

[10] J. P. K. Seville and C. Y. Wu. *Particle Technology and Engineering: An Engineer's Guide to Particles and Powders: Fundamentals and Computational Approaches.* Butterworth-Heinemann, 2016.

[11] P. Mills and P. Snabre. Settling of a suspension of hard spheres. *EPL*, 25(9):651, 1994.

[12] P. Snabre and P. Mills. Settling and fluidization of non Brownian hard spheres in a viscous liquid. *The European Physical Journal E*, 1(2-3):105–114, 2000.

[13] A. Pavlovitch, R. Jullien, and P. Meakin. Geometrical properties of a random packing of hard spheres. *Physica A: Statistical Mechanics and its Applications*, 176(2):206–219, 1991.

[14] S. B. Savage and C. K. K. Lun. Particle size segregation in inclined chute flow of dry cohesionless granular solids. *Journal of Fluid Mechanics*, 189:311–335, 1988.

[15] S. Volpato, M. Tirapelle, and A. C. Santomaso. Modeling and experimental investigation of shear-induced particle percolation in diluted binary mixtures. *Physical Review E*, 102(1):1–8, 2020.

[16] A. M. Fry, V. Vidyapati, J. P. Hecht, P. B. Umbanhowar, J. M. Ottino, and R. M. Lueptow. Measuring segregation characteristics of industrially relevant granular mixtures: Part II – Experimental application and validation. *Powder Technology*, 368: 278–285, 2020.

[17] D. Bertuola, S. Volpato, P. Canu, and A. C. Santomaso. Prediction of segregation in funnel and mass flow discharge. *Chemical Engineering Science*, 150:16–25, 2016.

[18] L. Svarovsky. *Powder testing guide.* 1987.

[19] C. Kloss, C. Goniva, A. Hager, S. Amberger, and S. Pirker. Models, algorithms and validation for opensource dem and cfd–dem. *Progress in Computational Fluid Dynamics, an International Journal*, 12(2-3):140–152, 2012.

[20] LIGGGHTS(R)-PUBLIC website. `https://www.cfdem.com`, n.d.

[21] B. Remy, J. G. Khinast, and B. J. Glasser. Discrete element simulation of free flowing grains in a four-bladed mixer. *AIChE Journal*, 55(8):2035–2048, 2009.

[22] Y. C. Zhou, A. B. Yu, R. L. Stewart, and J. Bridgwater. Microdynamic analysis of the particle flow in a cylindrical bladed mixer. *Chemical Engineering Science*, 59(6): 1343–1364, 2004.

[23] T. Roessler, C. Richter, A. Katterfeld, and F. Will. Development of a standard calibration procedure for the DEM parameters of cohesionless bulk materials – part I: Solving the problem of ambiguous parameter combinations. *Powder Technology*, 343:803–812, 2019.

[24] L. Jing, C. Y. Kwok, and Y. F. Leung. Micromechanical origin of particle size segregation. *Physical review letters*, 118(11):118001, 2017.

[25] R. Hogg. Mixing and segregation in powders: evaluation, mechanisms and processes. *KONA Powder and Particle Journal*, 27:3–17, 2009.

[26] P. Virtanen, R. Gommers, T. E. Oliphant, M. Haberland, T. Reddy, D. Cournapeau, E. Burovski, P. Peterson, W. Weckesser, J. Bright, et al. SciPy 1.0: Fundamental Algorithms for ScientificComputing in Python. *Nature Methods*, 17(3):261–272, 2020.

[27] L. Burtseva and F. Werner. *Modeling of spherical particle packing structures using mathematical tessellation.* Univ., Fak. für Mathematik, 2015.

[28] The Royal Society of Chemistry. Using a voronoi tessellation to measure properties of a polydisperse sphere packing in a microphase separated system. 2010.

[29] C. Rycroft. Voro++: A three-dimensional voronoi cell library in c++. Technical report, Lawrence Berkeley National Lab.(LBNL), Berkeley, CA (United States), 2009.

[30] C. A. Grattoni and R. A. Dawe. Anisotropy in pore structure of porous media. *Powder technology*, 85(2):143–151, 1995.

[31] G. I. Tardos, S. McNamara, and I. Talu. Slow and intermediate flow of a frictional bulk powder in the couette geometry. *Powder Technology*, 131(1):23–39, 2003.

Chapter 4

Size segregation in multi-component granular mixtures

In chapter 3, we proposed a percolation model for diluted binary mixtures and we evaluated its validity for a range of shear rates and diameter ratios. A natural extension for the model concerns the introduction of fine particles concentration and the generalization to multi-component mixtures. In this chapter, we generalize the percolation model to a multi-component mixture made up of discrete solid phases having different particle sizes but same intrinsic density. This represents a step forward in the description of segregation since most of the existing formulations are for binary mixtures only. The model has been implemented in a continuum framework and fully coupled with a solid flow rheology.

Parts of this chapter have been submitted for publication:

M. Tirapelle, S. Volpato, and A. C. Santomaso. A theory for size-driven segregation in dense multidisperse granular mixtures.

4.1 Introduction

Continuum models differ from DEM because they do not explicitly represent individual grains but rather they treat the bulk solid as a pseudo-fluid (see Section 2.2). The standard starting point for the development of continuum models is the combination of an advection-diffusion transport equation with appropriate rheology for the granular solid [1]. Continuum modelling for predicting segregation in binary mixtures has been implemented many times and for several processes such as mixing in tumblers [2, 3], transport in chute [4–6], granular avalanches [7, 8], filling and emptying of silos and hoppers [9, 10]. However, there exist only a few studies focusing on segregation in multi-component or poly-disperse mixtures [11–16]. Furthermore, even in the most advanced segregation models, segregation equations and velocity field are usually uncoupled [17]. Coupling segregation and flow field becomes of importance especially when the degree of dispersity is large and hence, the local mobility depends on the local concentrations [1, 17].

The challenge addressed in this chapter is the development of a general multi-component segregation model fully coupled with a rheology for the granular mixture. To validate the model, simulations for ternary mixtures of coarse, intermediate and fine particles during emptying of a storage hopper are performed in COMSOL Multiphysics. The model predictions are validated against experimental data and DEM outcomes taken from the literature. The main advantages of our model are: it is simple, it can be applied to mixtures made of any number of discrete solid phases that differs by size and it is potentially applicable to any geometry and flow configuration.

4.2 Governing equations

4.2.1 Multiphase Fluid Dynamic Model

The granular material is assumed to be composed of a finite number of grain-size classes having the same intrinsic density. The velocity field of the bulk solid is determined directly by solving the momentum equations for incompressible granular flows (Eq. 2.27) together with the generalized rheological model proposed by Artoni et al. [18] and derived in Section 2.2.2.3.

To describe the evolution of the free surface between bulk solid and air, we employed the level set method (see Section 2.3.3). In particular, we employed the laminar two-phase flow with the level set physics module of COMSOL Multiphysics. Therefore, a unique set of conservation equations is solved throughout all domain. The density and viscosity are described through the level set function respectively as:

$$\rho = \rho_s + (\rho_{air} - \rho_s)\,\psi\,, \tag{4.1}$$

$$\eta = \eta_s + (\eta_{air} - \eta_s)\,\psi\,, \tag{4.2}$$

where the subscripts indicate the phase of belonging. Notice that, far from the interface, where $\psi = 0$, the density and viscosity are the ones of the solid phase (i.e. the ones discussed in Section 4.2.1) while, where $\psi = 1$, the density and viscosity are the ones of pure air. For air, we used the properties of air (gas) of COMSOL's material library.

4.2.2 Segregation Equations

In quasi 2D gravity-driven flows, such as discharge from a storage hopper, the only relevant components of the segregation flux and diffusion coefficient are the ones that act in the direction of gravity. Furthermore, because the diffusion of grains in a polydisperse system is still a matter of research, $\mathcal{D}$ is usually treated as a constant. It has also been proved that it is reasonable to neglect the dependence of the diffusion coefficient on a spatially varying shear rate [19]. Thus, in a 2D gravity-driven flow, the standard advection-diffusion segregation equation (i.e. Eq. 2.57) reduces to:

$$\frac{\partial \phi_i}{\partial t} + \frac{\partial (u\phi_i)}{\partial x} + \frac{\partial (v\phi_i)}{\partial z} = -\frac{\partial (v_{i,NET}\phi_i)}{\partial z} + \frac{\partial}{\partial z}\left(\mathcal{D}\frac{\partial \phi_i}{\partial z}\right), \tag{4.3}$$

where u and v are the horizontal and vertical components of $\boldsymbol{u}$ and $v_{i,NET}$ is the normal component of the net segregation velocity, which is aligned with gravity.

4.3 Flux Functions and Segregation Velocities

A number of mechanisms have been proposed in the literature for describing the segregation of dissimilar particles in granular flows (see Section 2.1.1). Here, we focus on the two mechanisms proposed by Savage and Lun [4] which are referred to as kinetic sieving and squeeze expulsion. For modelling kinetic sieving, we propose a generalization of the model reported in the chapter 3. For modelling squeeze expulsion, we implement the overall mass conservation [4]. In developing the particle size-segregation model, we assumed that 1) the system is incompressible (i.e. the solid volume fraction or packing density, ν, is constant in time and space) and 2) squeeze expulsion is not size preferential. The result is a new and original expression for size-driven segregation that can be applied to multi-component mixtures of grains.

4.3.1 Distribution of voids

We have seen that, in a dense isotropic matrix of mono-disperse spherical particles, the mean distance between particles can be expressed as [20]:

$$\bar{h} = \frac{2}{3} d \frac{1-\nu}{\nu}, \tag{4.4}$$

where d is the particle diameter and ν is the solid volume fraction. As a matter of fact, there are not formulations of $\bar{h}$ for the case of mixtures of particles differing in size. Therefore, we propose the following expression for $\bar{h}$:

$$\bar{h} = \frac{2}{3} \bar{d} \frac{1-\nu}{\nu}, \tag{4.5}$$

where $\bar{d}$ is the local average diameter. The rationale behind this is that, on average, the mean distance between particles in a multi-component system can be linked to the mean particle distance of an isotropic packing having particles with a diameter equal to $\bar{d}$. It is important to highlight that this assumption holds only if ν is constant, as it is for incompressible granular flows. Bearing this in mind, the length distribution of the

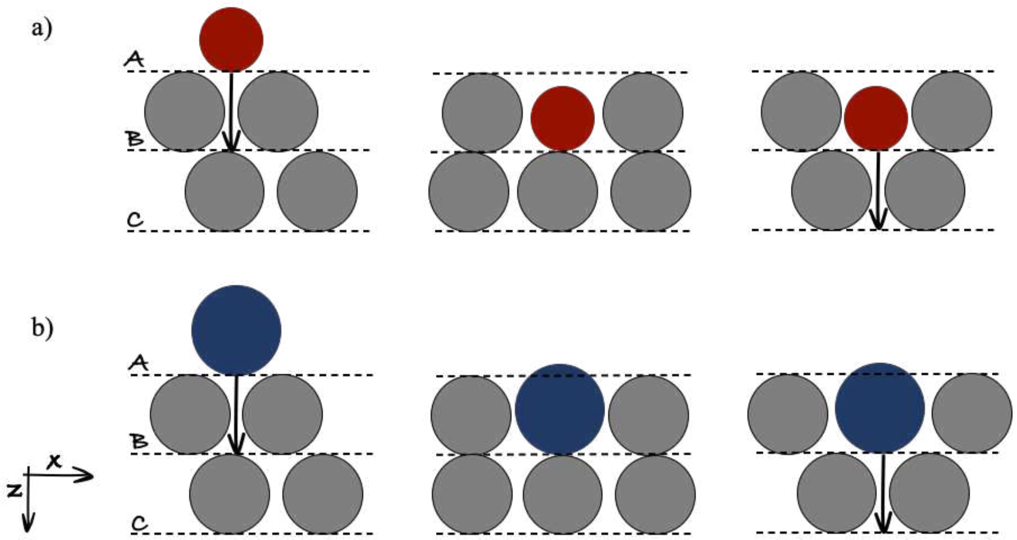

Figure 4.1: Schematic representation of a) a fine particle and b) a coarse particle percolating through a bed of middle-sized grains. If a particle in layer A finds a beneath void space that is large enough, it drops into layer B. Since each layer moves with different shear velocities, it could happen that the particle centre will lie again on a void space large enough and thus the particle will drop in layer C.

distances in the empty space of a random packing, $F(h)$, has an exponential form of the type [21]:

$$F(h) = \frac{1}{\bar{h}} \exp\left(-\frac{h}{\bar{h}}\right) . \tag{4.6}$$

To fall into the underlying layer of grains, a particle has to find an aperture greater than itself. Let us consider a small particle from layer A in a bed of middle-sized grains with diameter $\bar{d}$ (see Fig. 4.1-a). If the particle finds a sufficient large void space, it percolates in the underlying layer B. The particle will then be directed from layer B toward layer C when its centre lies within another sufficiently large capturing void. Similarly, also a large particle can drop from a layer into a void in the underlying layer if the void space is large enough (see Fig. 4.1-b). We assume that, when a particle falls into the underlying layer, independently by its own size, it covers on average a space equal to the local average diameter $\bar{d}$.

It is straightforward that smaller particles are more likely than larger particles to find an aperture great enough to fall in. Mathematically, the probability for the i-th particle to find an aperture greater than its own diameter in one direction is:

$$P(h \geq d_i) = \int_{d_i}^{\infty} F(h) \mathrm{d}h = \int_{d_i}^{\infty} \frac{1}{\bar{h}} \exp\left(-\frac{h}{\bar{h}}\right) \mathrm{d}h = \exp\left(-\frac{d_i}{\bar{h}}\right) . \tag{4.7}$$

The particle can percolate through the underlying voids only if the latter condition is satisfied in the two directions normal to the percolation direction (i.e. x and y). Thus, the falling probability is the combined effect of two independent events (i.e. P_x and P_y)

and reads:

$$P_i = P(h_x \geq d_i \cap h_y \geq d_i) = P_x P_y = \exp\left(-2\frac{3}{2}\frac{d_i}{\bar{d}}\frac{\nu}{1-\nu}\right) . \tag{4.8}$$

To conclude, Eq. 4.8 expresses the probability of the *i*-th particle to percolate when it lies in an incompressible and isotropic packing of spherical particles with local average diameter $\bar{d}$ and packing density ν.

4.3.2 Kinetic sieving

Be P_i the probability for a particle of size d_i of finding a void space in the underlying layer large enough to be captured in, and $(1-P_i)$ the probability of not finding it. In the former case, the particle will fall for a distance $\bar{d}$, whereas in the latter case the particle will stay in its own layer. The average percolation velocity must therefore be proportional to [22]:

$$v_{p,i} \propto \frac{\bar{d} \cdot P_i + 0 \cdot (1-P_i)}{t_f \cdot P_i + t_s \cdot (1-P_i)} , \tag{4.9}$$

where t_f and t_s are the falling and stop times, respectively. According to what reported in chapter 3, the falling time is $t_f \propto \sqrt{\bar{d} g^{-1}}$, whereas the stopping time is proportional to the inverse of the shear rate: $t_s \propto \dot{\gamma}^{-1}$. Since the stopping time is estimated to be two orders of magnitude larger than the falling time, the latter can be neglected and Eq. 4.9 simplifies to:

$$v_{p,i} \simeq A\dot{\gamma}\bar{d}\frac{P_i}{(1-P_i)} , \tag{4.10}$$

where A is a proportionality parameter that relies on interparticle friction mediated by the bulk porosity [23]. As it is possible to see, the percolation velocity $v_{p,i}$ depends on: local shear rate, local average diameter and local falling probability. Under the same $\bar{d}$, smaller particles percolate faster because characterized by larger P_i. On the other hand, the same sized particle percolates faster in a bed of larger grains because of the greater falling distance $\bar{d}$. Finally, an increase of $\dot{\gamma}$ leads to a more frequent generation of voids and so, to a greater $v_{p,i}$.

It is noteworthy that Eq. 4.10 differs from the one reported in the previous chapter on two grounds. There, the falling space was set equal to $d_c - d_f$. In dilute conditions, this allowed satisfying the zero velocity for the limiting case $d_f \to d_c$. Secondly, a third probability, P_z, is taken into account. Here, we are dealing with a more general case, the zero flux is satisfied when $\phi_i = 1$ and the falling distance is approximated as an average value $\bar{d}$. Thus, we have to resort neither to size differences nor to weighting probability P_z.

The percolation velocities act always in the negative z-direction, thus there must be another mechanism that gives rise to a counterflow so as to satisfy the overall mass conservation along z [4]. This mechanism is discussed in detail in the following section.

4.3.3 Squeeze expulsion and net velocities

When the instantaneous forces acting on an individual particle are sufficiently imbalanced, the particle is squeezed out from its own layer into an upper layer [4]. This mechanism, which is referred to as squeeze expulsion, is not size-preferential and hence, its contribution can be simply determined by the satisfaction of the overall mass conservation along z [4]. Thus, the sum of all mass fluxes must be equal to zero:

$$\sum_{i=1}^{N} \rho_i v_{p,i} + \rho v_{SE} = 0\,, \tag{4.11}$$

where N is the number of components in the mixture, ρ_i is the mass of component i per unit volume, ρ is the overall bulk density, and v_{SE} is the squeeze-expulsion velocity. Since all particles have the same intrinsic density ρ^*, and since we assumed constant solid volume fraction, we get:

$$\rho^* \nu \sum_{i=1}^{N} \phi_i v_{p,i} + \rho^* \nu v_{SE} = 0\,, \tag{4.12}$$

where ϕ_i is the volume ratio of i (i.e. $\sum \phi_i = 1$). Thus, the squeeze-expulsion velocity shared by all components is:

$$v_{SE} = -\sum_{i=1}^{N} \phi_i v_{p,i}\,. \tag{4.13}$$

The net size-driven segregation velocity $v_{i,NET}$ of each component is made of two contributions [4]:

$$v_{i,NET} = v_{p,i} + v_{SE}\,. \tag{4.14}$$

Introducing 4.10 and 4.13 into Eq. 4.14, gives:

$$v_{i,NET} = A\dot{\gamma}\bar{d}\left[\frac{P_i}{(1-P_i)} - \sum_{i=1}^{N} \phi_i \frac{P_i}{(1-P_i)}\right]\,, \tag{4.15}$$

that becomes, in the dimensionless form:

$$v^*_{i,NET} = A\left[\frac{P_i}{(1-P_i)} - \sum_{i=1}^{N} \phi_i \frac{P_i}{(1-P_i)}\right]\,. \tag{4.16}$$

As expected, the net segregation velocity of a species relative to the mean velocity of the bulk flow is strongly dependent on the local shear rate and mean particle diameter [4, 24]. The fluxes of the different-sized particles are asymmetric in concentration [1, 25], satisfy a summation constraint [17]

$$\sum_{i} v_{i,NET} \phi_i = 0\,, \tag{4.17}$$

and are zero for $\phi_i = 0$ and $\phi_i = 1$.

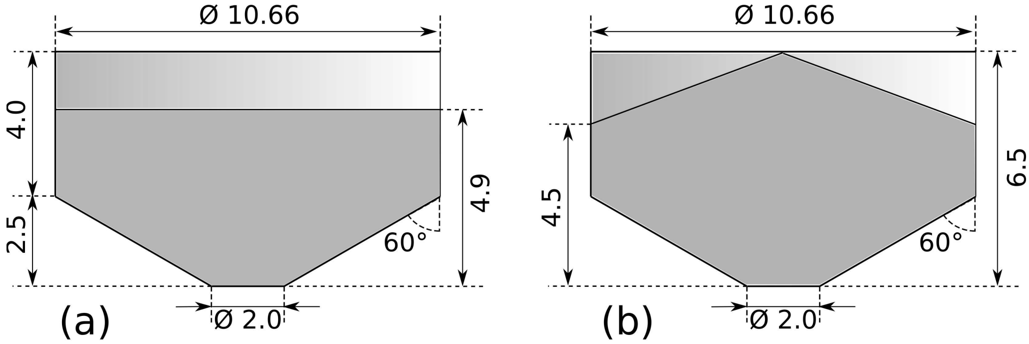

Figure 4.2: Schematic representation of the computational domain of the hopper with an initial profile of: a) random filling method and b) industrial filling method. The measures are given in cm.

Segregation determines a net flux of large particles migrating upwards and a net flux of fine particles moving downwards. If the reason why fine particles move preferentially downwards is clear and can be analytically described by the percolation model, the reason why coarse particles migrate preferentially upwards is not fully understood. Different explanations have been given in the literature such as the presence of an anisotropic contact network [26], an excessive pressure taken by the large particles that drives them to rise [26], a granular equivalent Saffman effect [27] and the presence of a buoyancy force analogous to the Archimedes' principle [28]. However, since the upward flux is the result of an overall mass balance, the correctness of the mathematical formulation is not biased by the lack of a universally accepted physical explanation [4].

4.4 Materials and methods

4.4.1 Numerical Implementation

Hoppers, silos and bins are the most common storage devices for granular material in industrial processes. During their filling and emptying, particle segregation may occur [29].

Here, we simulate a 2D axisymmetric hopper having 60^o wall-angles with respect to the vertical. The Cartesian coordinate system is defined with the x-axis laying horizontally and the z-axis laying vertically and pointing downward. The hopper is filled with ternary mixtures of particles homogeneously distributed. This means that segregation does not occur during the filling process. The composition of the standard mixture was 25:20:55 by volume of fine, intermediate and coarse grains. To capture the evolution of the solid free surface, we include a second phase made of ambient air on top. As in Yu and Saxén [30], we consider for the solid phase two filling methods: the random and the industrial filling methods. The two methods determine, respectively, a horizontal flat surface and the formation of a powder heap within the silo. A sketch of the two configurations is reported in Fig. 4.2. The geometry is discretized with a mesh having 2999 triangular elements and

$k' = 2\ \mathrm{s}^{-1}$	$\theta^* = 1.44\ \mathrm{s}^2\ \mathrm{m}^{-2}$	$\eta_0 = 0.5\ \mathrm{s}^{-1}$	$\nu = 0.6$	$A = 50$	$\mathcal{D} = 1\mathrm{e}{-6}\ \mathrm{m}^2\ \mathrm{s}^{-1}$

Table 4.1: Basic model parameters. The parameters of the rheological model (i.e. k', θ^*, η_0) have been calibrated according to Artoni et al. [18], Bertuola et al. [9] and Volpato et al. [3].

normal elements size (i.e. the longest edge of the element is ≈ 1.9 mm).

The parameters employed for the bulk flow are summarized in Tab. 4.1. As it is possible to see, k', as well as the granular temperature scale θ^*, are set as constants. For parameter A, we found after some trial simulations that $A = 50$ is a good value for the system under consideration.

4.4.2 Boundary and Initial Conditions

At the beginning, the material within the silos is stationary, so that the velocity field is zero everywhere within the domain. The same initial condition was imposed also for the top ambient air. The initial value of the granular temperature was set equal to the low value of $\theta = 0.12\ \mathrm{m}^2\mathrm{s}^{-2}$ for numerical reasons even if it should be strictly zero for granular matters at rest.

As boundary conditions, no-slip behaviour was imposed at the walls, and no penetration condition $u = 0$ is enforced. Then, we set 1 mm/s inlet velocity for air on the open top of the hopper. At the outlet, we imposed the atmospheric pressure. The resulting mass flow rate is in accordance with predictions made by the Beverloo equation [31]. For what concerns the segregation equations, we set no-flux of components through the lateral walls. About the granular temperature equation, we imposed the thermal insulation of the silos.

4.5 Results and discussion

4.5.1 Velocity field, granular temperature and segregation profiles

Our segregation model is built on the full coupling between segregation transport equations and rheology for the granular mixture. In this section, we look closely at the kinematic of the hopper discharge to ensure that the implemented rheology is appropriate. All the figures reported in this section refer to the case of hopper discharged after industrial filling (with heap formation) having 25:20:55 initial percentage of fine, intermediate and coarse particles.

Fig. 4.3 shows, on top, the velocity field of the bulk solid at four different discharge stages (i.e. $\tilde{M}$ is the normalized mass discharged defined as the ratio between the mass of material discharged and the total mass initially filled within the silo) and, on the bottom, the maps of the shear rate for the same values of $\tilde{M}$. As it is possible to see, the velocity field is characteristic of a funnel flow since there are significant velocity differences across the width of the hopper from the central core to the sidewalls with stagnant material at

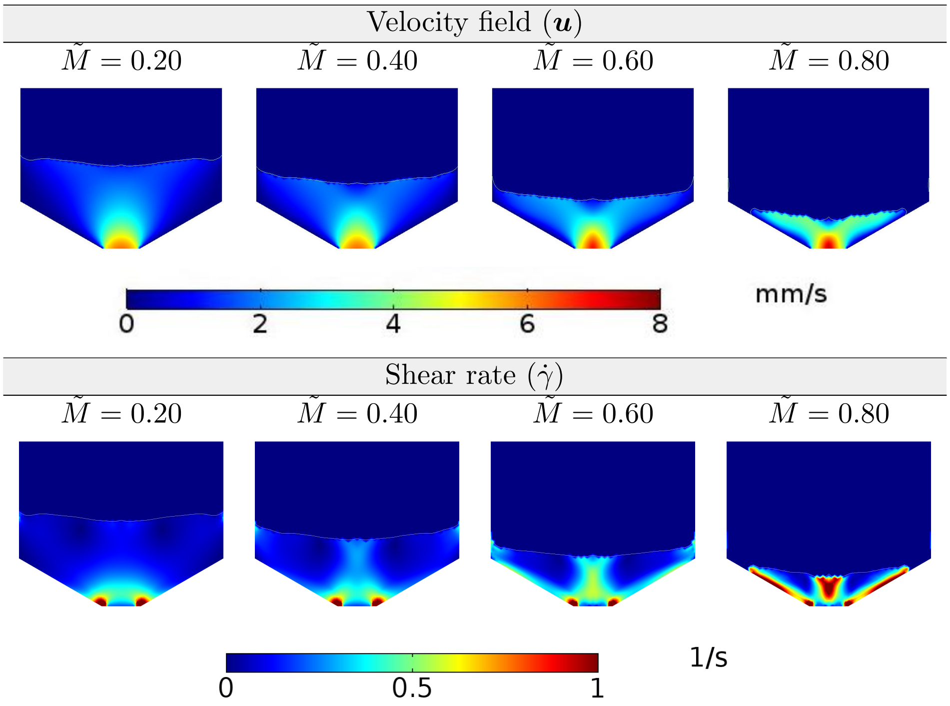

Figure 4.3: Profiles of the bulk velocity field (on top) and of the shear rate (on bottom) at 20%, 40%, 60% and 80% of normalized mass discharge $\tilde{M}$. The velocity is expressed in mm/s. The shear rate is expressed in s^{-1}.

the walls. In particular, the region of higher velocity extends through the orifice into the cone of the free surface [10]. About the shear rate, in the beginning, it is higher close to the orifice where the dynamic of the system is faster. Approaching the end of the discharge process, the stagnant zone becomes thinner, the velocity magnitude becomes higher at the outlet, and the shear rate becomes progressively more important near the sidewalls. Note that, despite the presence of the initial heap, the free surface becomes v-shaped after the beginning of the discharge process. These profiles qualitatively agree with empirical knowledge and with DEM simulations [30].

Fig. 4.4 shows the vertical velocity profiles of the bulk solid at different bed heights and at 20% normalized mass discharged. In addition, the inset shows the corresponding horizontal components. Since the silo is axisymmetric, only the left half of the profiles are reported. These velocity profiles are in qualitative agreement with the corresponding existing results reported in the literature [10].

We can conclude that the velocity pattern, the formation of the v-shaped free-surface as well as the mobility of the materials are sufficiently well described by the generalized version of the Artoni et al.'s rheology [18].

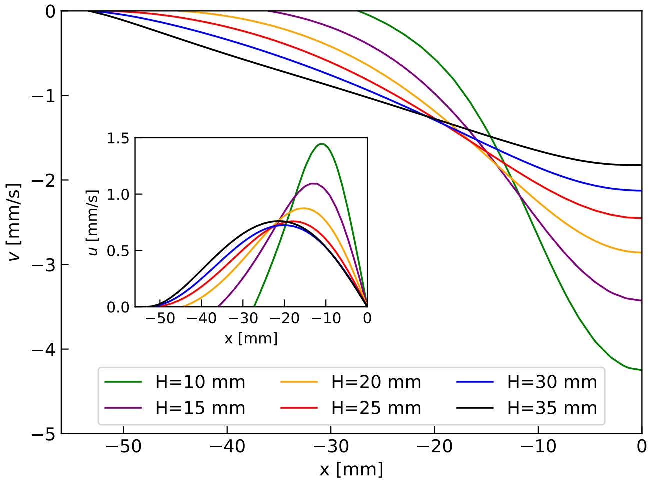

Figure 4.4: Vertical and horizontal (inset) bulk velocity profiles of the left half of the hopper at different bed heights for the case with industrial filling under initial mass percentage of fine, intermediate and coarse of 25%, 20% and 55%. The profiles are for t=9s, namely after 20% of the total mass discharge.

Fine particles diameter	d_f	1.5	mm
Intermediate particles diameter	d_m	2.4	mm
Coarse particles diameter	d_c	3.4	mm
Intrinsic solid density	ρ^*	2285	kg/m^3
Friction coefficient	μ	0.5	-

Table 4.2: Particle diameters, density and effective friction coefficient [30].

4.5.2 Model validation

Experimental data for multi-component mixtures of grains exiting a silo are scarce. Here, we compare our model predictions against independent experimental and DEM simulation data by Yu and Saxén [30]. In their study, they focused on the size-segregation of ternary mixtures of particles during discharge from a blast furnace hopper. The properties of the pellets are given in Tab. 4.2. In the following figures, the symbols reflect the experimental and DEM simulation data by Yu and Saxén [30] while the solid lines represent our model predictions. The x-axis is the normalized mass discharged $\tilde{M}$.

Fig. 4.5 shows the discharge profile of fine, intermediate and coarse particles considering 25:30:45 initial composition and the random filling method. In the beginning, the bulk solid is well-mixed. Then, because of the shear rate, size-driven segregation takes place. The coarse particles accumulate in the central region of the pile while fine particles concentrate at the inclined sidewalls. Such a segregated system is advected by the mean flow toward the hopper outlet. This determines, after 20% of normalized mass discharged, an enrichment of coarse particles in the outflow. Approaching the end of the discharge process, also the fine particles previously driven toward the sidewalls move toward the

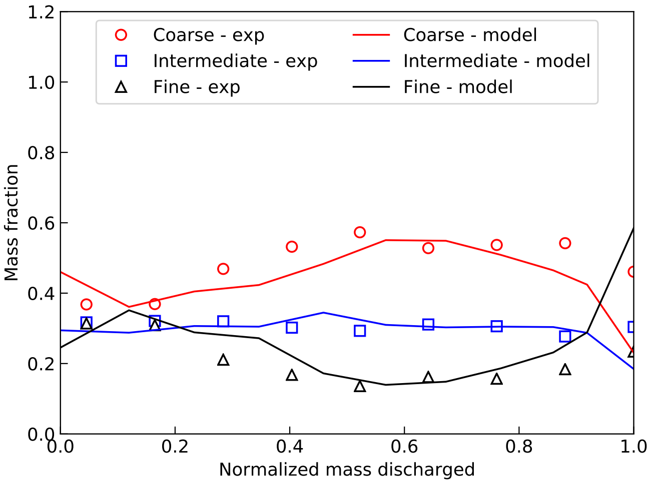

Figure 4.5: Comparisons of pellet mass fractions in hopper outflow measured in the experiments of Yu and Saxén [30] (data points) and CFD (continuous lines) under initial mass of fine, intermediate and coarse of 25%, 30% and 45%.

outlet. Note that, the composition of the intermediate particles at discharge remains approximatively constant during all the discharge process. All the three profiles reported in Fig. 4.5 are in good agreement with the experimental data. The main discrepancies concern the very last stage of the discharge and are mainly due to differences in wall-particle friction coefficient. This aspect will be discussed later on.

From now on, we focus on hopper discharge after industrial filling. This means that the solid matter forms a heap within the silo. Fig. 4.6 shows the discharge profile for a ternary mixture having 25:20:55 percent of fine, intermediate and coarse particles, respectively. We can see that the concentration of the three components remains constant until almost 30% of the normalized mass is discharged. At that point, the concentration of coarse particles slightly increases: the large particles, that were segregated in the central region of the pile, reach the outlet. A further discharge leads to the drainage of the lateral region which is rich in fines. Our model predictions generally agree well with the observations of Yu and Saxén [30] until almost 80% of the total mass discharged. As discharge continues, the model overestimates the amount of coarse particles (and thus underestimates the amount of fine particles) at the outlet. These discrepancies may be due to the solid flow rheology that may not describe well the velocity field near the surface (i.e. when low solid mass remains within the system) or, more likely, due to the no-slip boundary condition imposed at the lateral walls.

In their work, Yu and Saxén [30] changed the roughness of the wall by changing the friction coefficient between wall and particles. They found that different wall-particle static friction coefficients result in different discharge profiles, especially at the end of the discharge process. As it is possible to see in Fig. 4.7, the amount of fines exiting the hopper increases more sharply for $\mu_{s,p-w} = 0.5\%$ and 0.9% than for $\mu_{s,p-w} = 0.01\%$ and 0.1%.

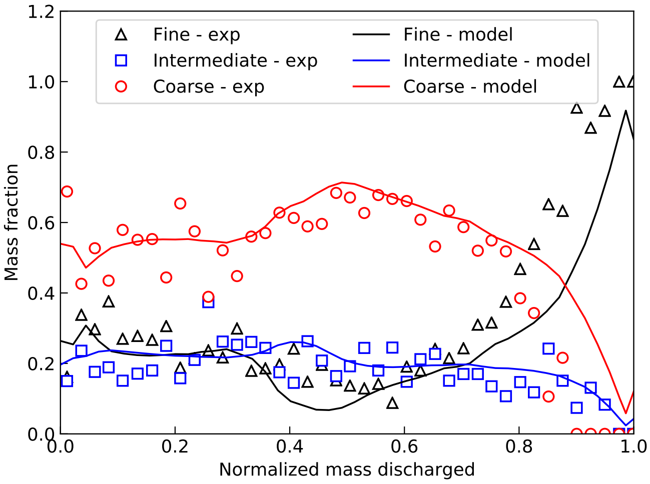

Figure 4.6: Comparisons of Yu and Saxén's [30] DEM simulations (markers) with the model (solid lines) for a hopper with industrial filling under the initial mass of fine, intermediate and coarse of 25%, 20% and 55%.

This is because, the higher the resistance of the walls, the less is the probability of sliding across the wall, and the greater is the extent of segregation. Since the predictions made by our theoretical model lie in between the two limiting cases found by Yu and Saxén [30], it is reasonable relating the discrepancies to the no-slip boundary condition. To account for different wall-particle friction coefficients in CFD software, one could include some resistive forces, empirical corrections or 3D-modelled rough surfaces.

To demonstrate the potentiality of the size-segregation model described in this paper, we also considered the effect of the number of fines, keeping a constant mass ratio of coarse and intermediate particles. Tab. 4.3 reports all the experimental concentrations simulated.

Fig. 4.8 compares the discharge profiles between model prediction and literature data for the case of the hopper with industrial filling and initial mixture composition of 5:24:71 of fine, intermediate and coarse particles. When the discharge process starts, the small amount of fines moves toward the walls in the so-called stagnant zone. Thus, at discharge, there is a reduction of fines. For what concerns the intermediate and coarse particles, their size difference is smaller, and their relative segregation behaviour is less significant. At the end of the discharge process, also the stagnant particles are advected by the main flow toward the exit of the silo. This leads to an enrichment in the outflow of fine and intermediate particles and a depletion of coarse particles. Again, the model can well predict the segregation patterns.

The comparison for the case with 45:14:41 initial mixture composition is reported in Fig. 4.9. Because of the higher relative amount of fine and coarse particles, the extent of segregation is higher than before. However, we can distinguish the same patterns: the exiting composition is almost constant at the beginning, then there is an enrichment of

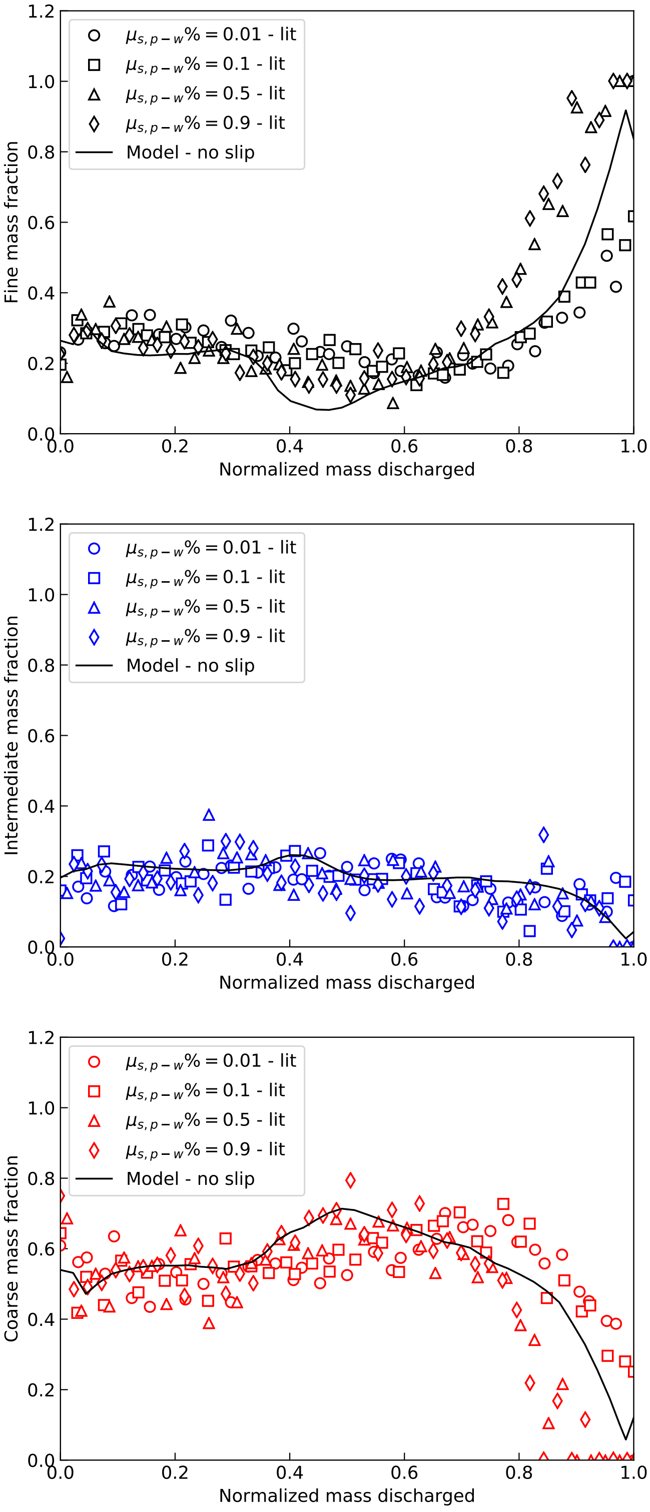

Figure 4.7: Comparisons of Yu and Saxén's [30] DEM simulations (markers) with the model (solid lines) for a hopper with industrial filling and considering the effect of wall-particle static friction ($\mu_{s,p-w}$). The initial mass of fine, intermediate and coarse are 25%, 20% and 55% respectively.

$m_f\%$	$m_m\%$	$m_c\%$	$\bar{d}_0$ [mm]	Fig.
5	24	71	3.065	4.8
25	20	55	2.725	4.6
45	14	41	2.405	4.9
65	9	26	2.075	4.10

Table 4.3: Different mixtures tested. The mass ratio between intermediate and coarse particles is kept constant, whereas the amount of fines is changed. The segregation is evaluated for a hopper with industrial filling.

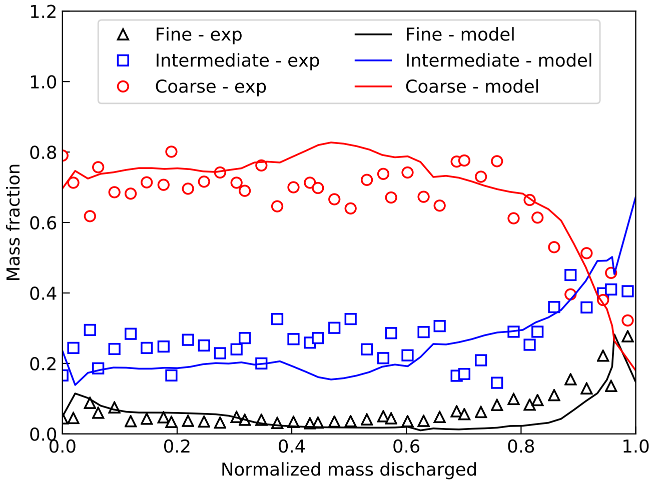

Figure 4.8: Comparisons of Yu and Saxén's [30] DEM simulations (markers) with the model (solid lines) for a hopper with industrial filling under initial mass of fine, intermediate and coarse of 5%, 24% and 71%.

coarse particles followed by an enrichment of fines. In this case, there are more significant discrepancies between model prediction and literature data: after 70% of mass discharged, the amount of fines exiting the hopper is underestimated while the amount of coarser is overestimated. This is because, in our CFD simulations the resistance of the walls is lower and, as a consequence, the lower is the extent of segregation.

In Fig. 4.10, we have reported another comparison between Yu and Saxén's [30] DEM simulations and our theory, but with 65:9:26 initial percentage of fine, intermediate and coarse particles, respectively. Again, the model predictions are qualitatively and quantitatively accurate.

We have also evaluated the effect of diameter ratio D_R, which is defined as the ratio between the coarse and the fine particles. The concentration profiles at discharge for the case with $D_R = 1.30$ are reported in Fig. 4.11. The diameter of fines, intermediates and coarse are equal to $d_S = 2.6$ mm, $d_M = 3.0$ mm and $d_L = 3.4$ mm. The relative concentrations of the components are 25:20:55 percentage by mass (i.e. as in the standard case). In this case, the segregation behaviour is less significant than in the case characterized by $D_R = 2.26$ (see Fig. 4.6) due to the slighter size difference. However, we can still see a

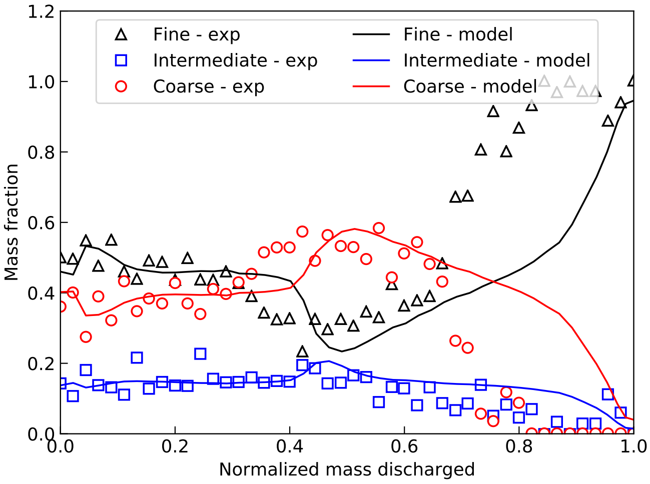

Figure 4.9: Comparisons of Yu and Saxén's [30] DEM simulations (markers) with the model (solid lines) for a hopper with industrial filling under initial mass of fine, intermediate and coarse of 45%, 14% and 41%.

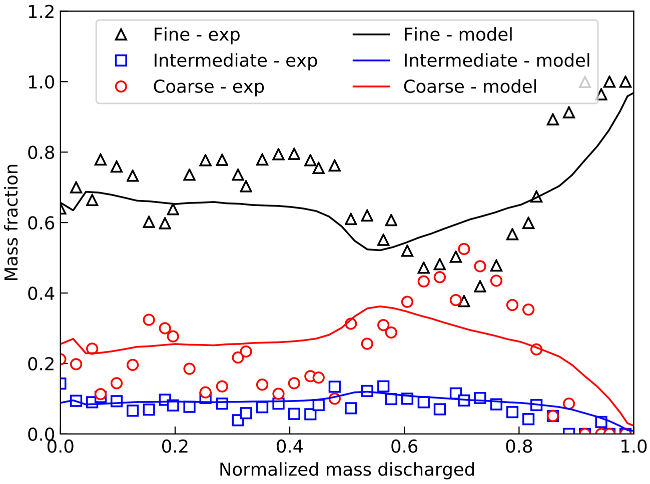

Figure 4.10: Comparisons of Yu and Saxén's [30] DEM simulations (markers) with the model (solid lines) for a hopper with industrial filling under initial mass of fine, intermediate and coarse of 65%, 9% and 26%.

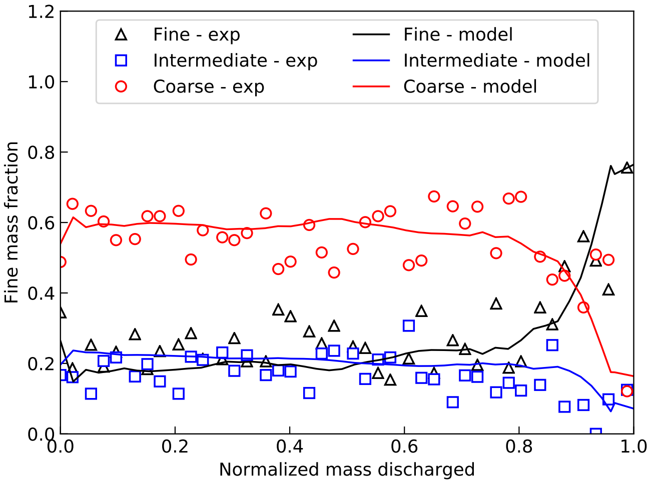

Figure 4.11: Comparisons of Yu and Saxén's [30] DEM simulations (markers) with the model (solid lines) for a hopper with industrial filling under initial mass of fine, intermediate and coarse of 25%, 20% and 55%. The particle diameters are $d_S = 2.6$ mm, $d_M = 3.0$ mm and $d_L = 3.4$ mm, thus $D_R = 1.3$.

significant increase in fines at the end of the discharge. This segregation pattern is well captured by the segregation model.

We have evaluated the performance of the model by calculating the root-mean-square error (RMSE) and the normalized root-mean-square error (NRMSE) for each component of each previous figure:

$$RMSE_i = \sqrt{\frac{\sum_{j=1}^{n} \left(\hat{y}_{i,j} - y_{i,j}\right)^2}{n}}\,, \tag{4.18}$$

$$NRMSE_i = \frac{RMSE_i}{\bar{y}_i}\,, \tag{4.19}$$

where $\hat{y}_{i,j}$ indicate the predicted values, n is the number of data points and $\bar{y}_i$ is the average experimental volume fraction of i. The results are reported in Tab. 4.4. In short, the comparison between literature data and theory shows that the multi-component segregation model describes generally well the segregation features.

We report in Fig. 4.12 the average diameter profiles for different mass fractions of fines and at different stages of the discharge process. Consistently with previous experimental observations [10, 32], segregation occurs with coarse particles in the central region where the flow is faster, fine particles close to the sidewalls and intermediate particles in the region sandwiched in between. The extent of segregation increase with the proceeding of the discharge process. Furthermore, when only 5% of fines are present, segregation is less significant: the mixture is made predominantly of intermediate and coarse particles whose diameter ratio is low. By looking at the segregation patterns, we can also distinguish the four main regions characteristic of a funnel flow [32, 33] that are: 1) a stagnant zone close to the sidewalls where fine particles accumulate, 2) a mobile zone in the central core that

		Fine	Intermediate	Coarse
Fig. 4.5	RMSE	0.12	0.04	0.09
	NRMSE	0.59	0.15	0.19
Fig. 4.8	RMSE	0.04	0.08	0.08
	NRMSE	0.57	0.29	0.12
Fig. 4.6	RMSE	0.13	0.05	0.12
	NRMSE	0.36	0.28	0.25
Fig. 4.9	RMSE	0.21	0.05	0.17
	NRMSE	0.36	0.43	0.53
Fig. 4.10	RMSE	0.11	0.03	0.10
	NRMSE	0.15	0.34	0.44
Fig. 4.11	RMSE	0.09	0.06	0.09
	NRMSE	0.31	0.36	0.16

Table 4.4: Root mean square error (RMSE) and normalized root mean square error (NRMSE) of all the comparisons.

is rich in coarse particles, 3) a linear surface flow and 4) a cross-over region.

To conclude, the model works for multi-component mixtures with different component concentrations and different diameter ratios. As expected, the extent of segregation is more significant for higher relative concentrations of fine and coarse particles and for higher D_R. The segregation model has only one drawback: it relies on a fitting parameter, A. As argued by Volpato et al. [22], its value could depend on particle properties such as particle sphericity and surface roughness therefore, a further study is required for independently estimating A.

4.5.3 Net segregation velocities and asymmetric flux functions

Golick and Daniels [34] observed that the segregation rate is not symmetric: a fine particle in a matrix of coarse grains segregates faster than a coarse particle in a matrix of fine grains. Furthermore, the maximum velocity for the coarse particles occurs when there are other coarse particles nearby rather than when they are isolated [25, 35]. This yields flux functions that are asymmetric with respect to the local particle concentration and non-convex with an inflexion point. To address the non-convex asymmetry of the segregation flux, Gajjar and Gray [25] proposed a cubic law of the type:

$$F(\phi_f) = A_\gamma \phi_f (1-\phi_f)(1-\gamma\phi_f)\,, \tag{4.20}$$

with γ, which represents the amount of asymmetry, bounded in between $0.5 \le \gamma \le 1$ [25]. The values of A_γ and γ are dependent upon the actual particle properties such as the diameter ratio itself [36]. Notice that, this formulation has been used as a practical

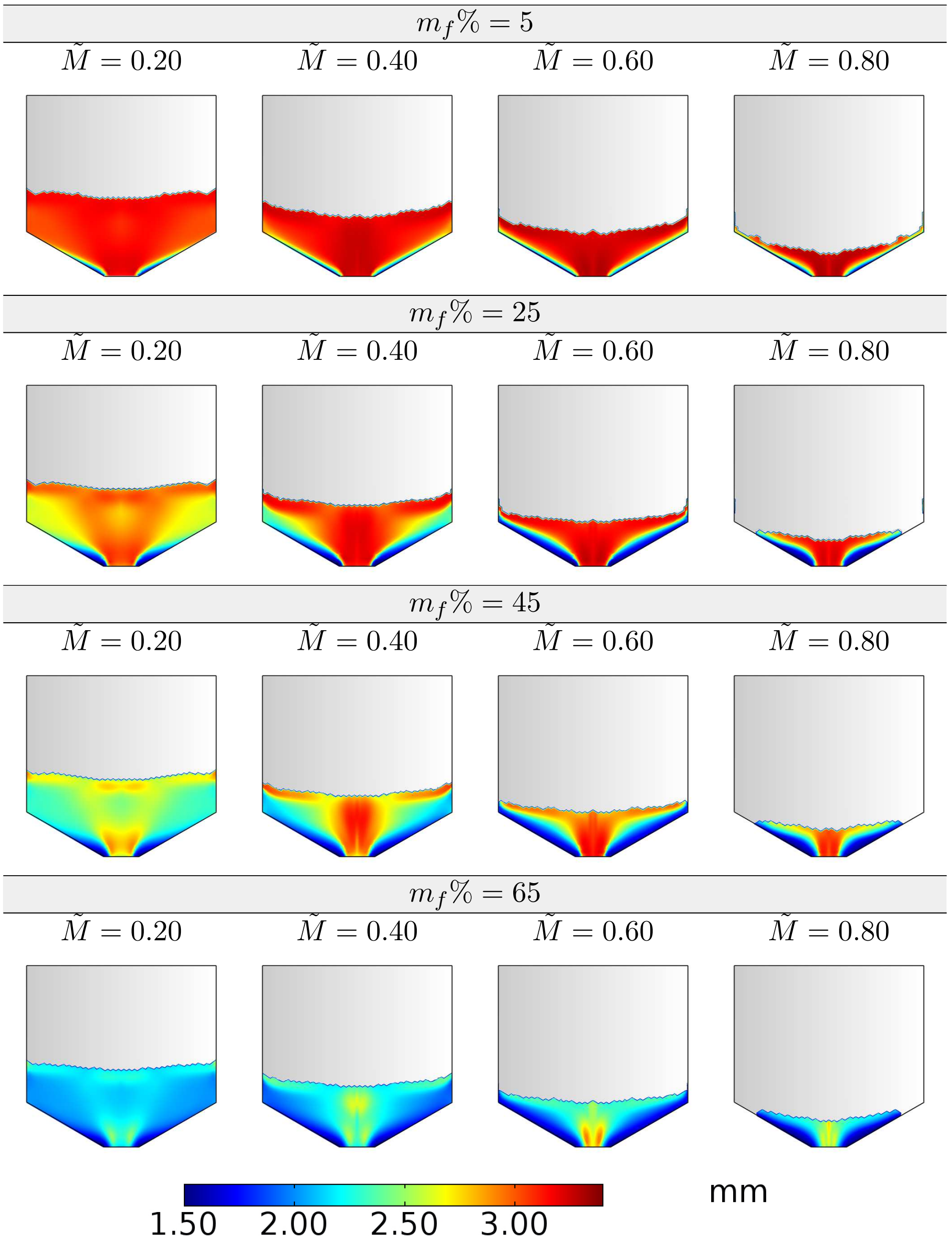

Figure 4.12: Profiles of the average diameter after (by column) 20%, 40%, 60% and 80% of normalized mass discharge $\tilde{M}$. The initial mass of fine is (by row) 5%, 25%, 45% and 65%.

example and it does not come from experimental evidence.

In this section, we show that our segregation rate, which instead has been developed from physical insights, is asymmetric and that the maximum coarse-particle rise velocity occurs at $\phi_{crit} \neq 1$. Furthermore, we show that the flux function is a singly non-convex asymmetric function. If we expand the net segregation velocity (Eq. 4.15) for the case of a bi-disperse granular system composed of fine and coarse particles, we obtain respectively:

$$v_{f,NET} = A\dot{\gamma}\bar{d}(1-\phi_f)\left(\frac{P_f}{1-P_f} - \frac{P_c}{1-P_c}\right), \tag{4.21}$$

$$v_{c,NET} = -\frac{(1-\phi_c)}{(1-\phi_f)} v_{f,NET}\,. \tag{4.22}$$

If we then define the odds of a particular outcome (i.e falling or not falling in our specific case) as:

$$R_{pf} \equiv \frac{P_f}{1-P_f} \text{ and } R_{pc} \equiv \frac{P_c}{1-P_c}, \tag{4.23}$$

the net segregation velocity for the fine particles (Eq. 4.21) becomes:

$$v_{f,NET} = A\dot{\gamma}\bar{d}(1-\phi_f)\left(R_{pf} - R_{pc}\right). \tag{4.24}$$

Using a chemical similarity, we can say that the shear rate $\dot{\gamma}$ is analogous to a kinetic constant (since it quantifies the rate of segregation) whereas the difference $R_{pf} - R_{pc}$ constitutes the segregation driving force. The sign of $R_{pf} - R_{pc}$ also determines whether the particle is going to rise or fall with respect to the direction of gravity. Since for bi-disperse granular materials, the segregation flux $F(\phi_i)$ for species i is defined as [37]:

$$F(\phi_i) = v_{i,NET}\phi_i\,, \tag{4.25}$$

we get:

$$F(\phi_f) = A\dot{\gamma}\bar{d}\phi_f(1-\phi_f)\left(R_{pf} - R_{pc}\right). \tag{4.26}$$

This flux function bears some similarities with Eq. 4.20 and it is well approximated by the following quartic function:

$$F(\phi) = \mathcal{A}(\phi^4 - \phi) - \mathcal{B}(\phi^3 - \phi^2)\,. \tag{4.27}$$

The main advantage of the latter formulation is that it relies on two parameters that are dependent only upon the diameter ratio: $\mathcal{A} = -0.215D_R^2 + 0.441D_R - 0.246$ and $\mathcal{B} = 0.649D_R^2 - 1.357D_R + 0.759$.

Fig. 4.13 shows the segregation flux function for three different diameter ratios: $D_R = 1.30$, $D_R = 1.80$ and $D_R = 2.26$. The squared data represents our model and are fitted to both Eq. 4.20 (solid lines) and the quartic function in Eq. 4.27 (dashed lines). For the case of $D_R = 1.3$, the best fitting is achieved with Eq. 4.20. However, for higher size

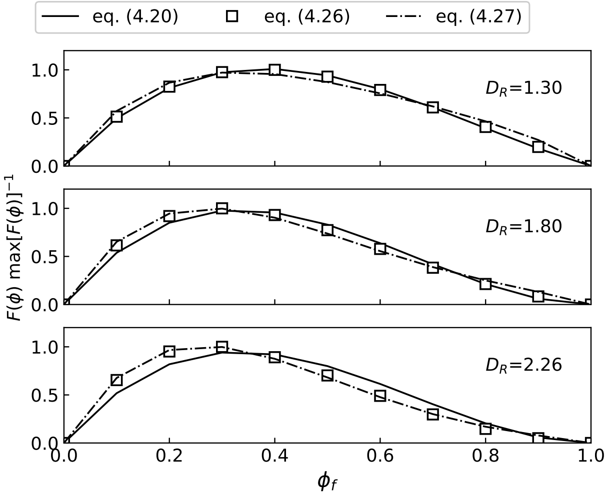

Figure 4.13: Normalized segregation flux function as a function of the fine particle concentration for binary mixtures with (from top to bottom) $D_R = 1.30$, $D_R = 1.80$ and $D_R = 2.26$. The model outcomes (squared data) are fitted with both the cubic flux function reported in Eq. 4.20 (see [25]) and the quartic flux function (Eq. 4.27).

ratios, the trend is clearly better predicted by Eq. 4.27. This is because the parameter γ that appears in Eq. 4.20 is physically dependent on the size ratio and quickly reaches the limiting value of 1.

Let us now consider a ternary system. In this case, the segregation flux for the fine, intermediate and coarse particles reads respectively:

$$F_f = A\dot{\gamma}\bar{d}\phi_f \left[\phi_m R_{pm}\left(\frac{R_{pf}}{R_{pm}} - 1\right) + \phi_c R_{pc}\left(\frac{R_{pf}}{R_{pc}} - 1\right)\right], \tag{4.28}$$

$$F_m = A\dot{\gamma}\bar{d}\phi_m \left[\phi_f R_{pf}\left(\frac{R_{pm}}{R_{pf}} - 1\right) + \phi_c R_{pc}\left(\frac{R_{pm}}{R_{pc}} - 1\right)\right], \tag{4.29}$$

$$F_c = A\dot{\gamma}\bar{d}\phi_c \left[\phi_f R_{pf}\left(\frac{R_{pc}}{R_{pf}} - 1\right) + \phi_m R_{pm}\left(\frac{R_{pc}}{R_{pm}} - 1\right)\right]. \tag{4.30}$$

As it is possible to see, the flux functions are dependent upon the particle diameters and the local particle concentration. Furthermore, the dependence of F on the concentration is higher than quadratic because the concentration appears also within the odds. Fig. 4.14 shows the model-predicted $F/(A\dot{\gamma})$ of ternary mixture of particles for the following three cases:

1. $d_S = 2.6$, $d_M = 3.0$ and $d_L = 3.4$ mm (i.e. $D_R = d_L/d_S = 1.3$),
2. $d_S = 1.89$, $d_M = 2.65$ and $d_L = 3.4$ mm (i.e. $D_R = 1.8$),
3. $d_S = 1.50$, $d_M = 2.40$ and $d_L = 3.4$ mm (i.e. $D_R = 2.26$).

As it is possible to see, at constant shear rates, the higher the size ratio, the higher the magnitude of the flux function for a given concentration. Furthermore, there is a net flux function of small particles downward and a net flux function of coarse particles moving upwards. The intermediate particle can instead segregate both upwards or downwards according to the mixture composition. It is also interesting to see that, the amount of asymmetry of the flux function diminishes with increasing the percentage of intermediate particles. Furthermore, there exist a combination of concentrations at which the intermediate particles, on average, do not migrate (they move neither upward nor downward).

We have demonstrated that our model can well capture the concentration-dependent asymmetry characteristic of the particle size segregation flux. Furthermore, for the case of binary mixtures, we have proposed a further formulation for the flux function that works for all size ratios and that does not rely on fitting parameters. This has huge potential in improving continuum models for predicting segregation.

4.6 Conclusions

In this study, a new continuum model for size-driven segregation in multi-component mixtures of grains has been implemented. The model is based on a full coupling between solid flow rheology of granular materials and segregation transport equations. The main originality of the work lies in the new closure for the segregation velocity that is based on probabilistic assumptions.

The model is implemented for simulating the segregation behaviour of ternary mixtures of grains during discharge from a storage hopper. The outcomes of the model are compared with independent data taken from the literature. The model predictions are in good agreement with experiments and DEM simulations data. Some discrepancies arise only at the final stage of the discharge process. However, we found that these discrepancies are due to the wall-particle friction coefficient. The model can also well predict the singly no-convex asymmetric behaviour of the flux function.

To conclude, the model is well-suited for predicting the segregation of multi-component granular mixtures in any geometry and flow configuration. It can be successfully applied to a range of mixture compositions and diameter ratios, and it can well capture the kinematic of the solid flow. The main drawback of the segregation model is that it relies on one fitting parameter, A. Notice that, further works are required to understand on theoretical grounds the squeeze expulsion mechanism.

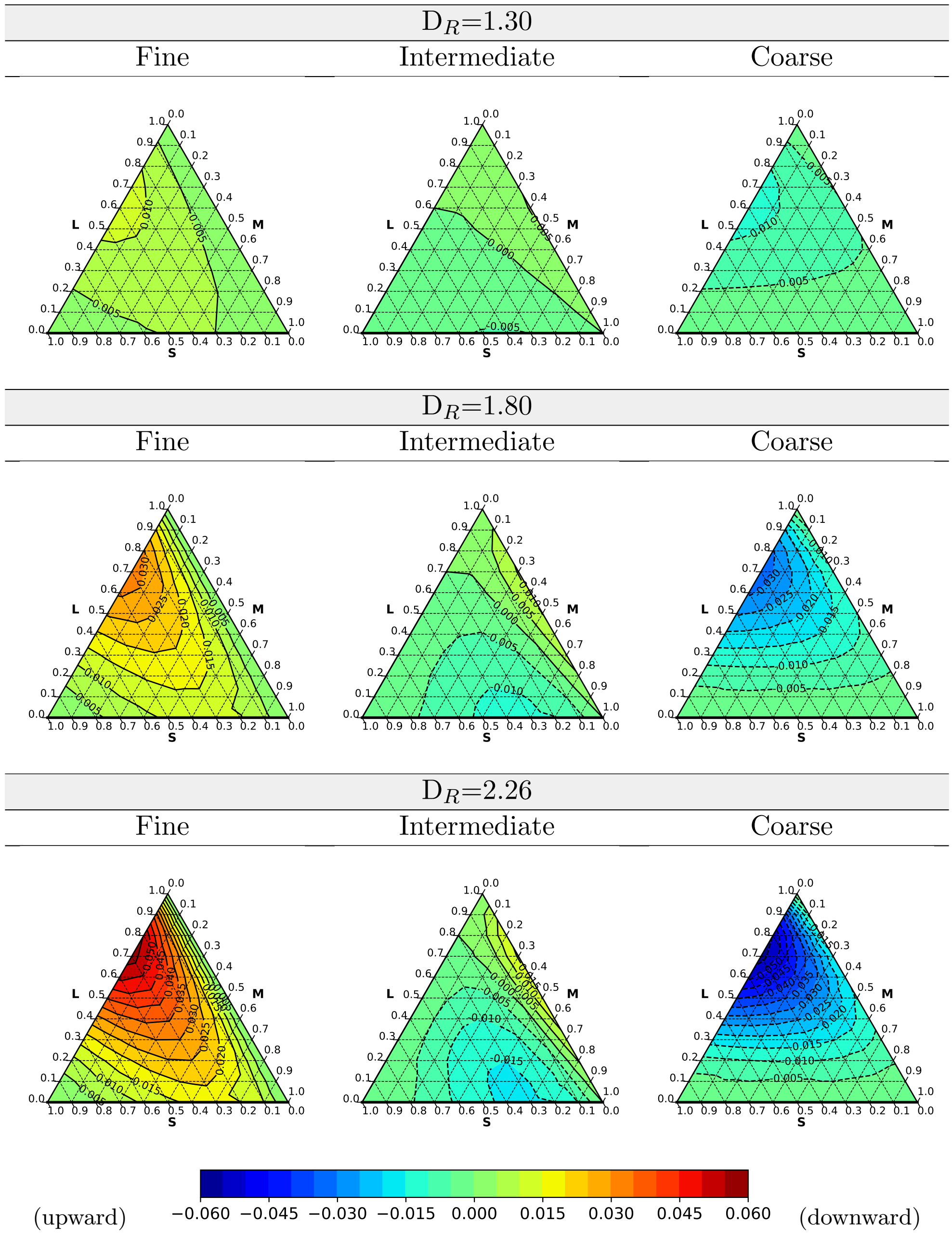

Figure 4.14: Ternary contour plots of $F/(A\dot{\gamma})$ for (by column) the fine, intermediate and coarse particles when considering a ternary mixture. The flux have been predicted (by row) for three different size ratios: $D_R = 1.3$, $D_R = 1.8$ and $D_R = 2.26$.

Bibliography

[1] P. B. Umbanhowar, R. M. Lueptow, and J. M. Ottino. Modeling segregation in granular flows. *Annual Review of Chemical and Biomolecular Engineering*, 10:129–153, 2019.

[2] C. P. Schlick, Y. Fan, P. B. Umbanhowar, J. M. Ottino, and R. M. Lueptow. Granular segregation in circular tumblers: Theoretical model and scaling laws. *Journal of Fluid Mechanics*, 765:632–652, 2015.

[3] S. Volpato, P. Canu, and A. C. Santomaso. Simulation of free surface granular flows in tumblers. *Advanced Powder Technology*, 28(3):1028–1037, 2017.

[4] S. B. Savage and C. K. K. Lun. Particle size segregation in inclined chute flow of dry cohesionless granular solids. *Journal of Fluid Mechanics*, 189:311–335, 1988.

[5] V. N. Dolgunin, A. N. Kudy, and A. A. Ukolov. Development of the model of segregation of particles undergoing granular flow down an inclined chute. *Powder Technology*, 96(3):211–218, 1998.

[6] S. Wiederseiner, N. Andreini, G. Épely-Chauvin, G. Moser, M. Monnereau, J. M. N. T. Gray, and C. Ancey. Experimental investigation into segregating granular flows down chutes. *Physics of Fluids*, 23(1):013301, 2011.

[7] J. M.N.T. Gray and A. R. Thornton. A theory for particle size segregation in shallow granular free-surface flows. *Proceedings of the Royal Society A: Mathematical, Physical and Engineering Sciences*, 461(2057):1447–1473, 2005.

[8] J. M. N. T. Gray and V. A. Chugunov. Particle-size segregation and diffusive remixing in shallow granular avalanches. *Journal of Fluid Mechanics*, 569:365–398, 2006.

[9] D. Bertuola, S. Volpato, P. Canu, and A. C. Santomaso. Prediction of segregation in funnel and mass flow discharge. *Chemical Engineering Science*, 150:16–25, 2016.

[10] H. Xiao, Y. Fan, K. V. Jacob, P. B. Umbanhowar, M. Kodam, James F. Koch, and R. M. Lueptow. Continuum modeling of granular segregation during hopper discharge. *Chemical Engineering Science*, 193:188–204, 2019.

[11] A. R. Thornton, J. M. N. T. Gray, and A. J. Hogg. A three-phase mixture theory for particle size segregation in shallow granular free-surface flows. *Journal of Fluid Mechanics*, 550:1–25, 2006.

[12] J. M.N.T. Gray and C. Ancey. Multi-component particle-size segregation in shallow granular avalanches. *Journal of Fluid Mechanics*, 678:535–588, 2011.

[13] B. Marks, P. G. Rognon, and I. Einav. Grainsize dynamics of polydisperse granular segregation down inclined planes. *Journal of Fluid Mechanics*, 690:499–511, 2012.

[14] C. P. Schlick, A. B. Isner, B. J. Freireich, Y. Fan, P. B. Umbanhowar, J. M. Ottino, and R. M. Lueptow. A continuum approach for predicting segregation in flowing polydisperse granular materials. *Journal of Fluid Mechanics*, 797:95–109, 2016.

[15] Z. Deng, P. B. Umbanhowar, J. M. Ottino, and R. M. Lueptow. Continuum modelling of segregating tridisperse granular chute fow. *Proceedings of the Royal Society A: Mathematical, Physical and Engineering Sciences*, 474(2211), 2018.

[16] M. Tirapelle, A. C. Santomaso, and L. Mazzei. Cfd-pbe coupled model for size-driven segregation in polydisperse granular flows. *Chemical Engineering Science*, page 117065, 2021.

[17] T. Barker, M. Rauter, E. S. F. Maguire, C. G. Johnson, and J. M. N. T. Gray. Coupling rheology and segregation in granular flows. *Journal of Fluid Mechanics*, 909, 2021.

[18] R. Artoni, A. C. Santomaso, and P. Canu. Simulation of dense granular flows: Dynamics of wall stress in silos. *Chemical Engineering Science*, 64(18):4040–4050, 2009.

[19] Y. Fan, C. P. Schlick, P. B. Umbanhowar, J. M. Ottino, and R. M. Lueptow. Modelling size segregation of granular materials: the roles of segregation, advection and diffusion. *Journal of Fluid Mechanics*, 741:252–279, 2014.

[20] P. Mills and P. Snabre. Settling of a suspension of hard spheres. *EPL*, 25(9):651, 1994.

[21] A. Pavlovitch, R. Jullien, and P. Meakin. Geometrical properties of a random packing of hard spheres. *Physica A: Statistical Mechanics and its Applications*, 176(2):206–219, 1991.

[22] S. Volpato, M. Tirapelle, and A. C. Santomaso. Modeling and experimental investigation of shear-induced particle percolation in diluted binary mixtures. *Physical Review E*, 102(1):1–8, 2020.

[23] M. Tirapelle, S. Volpato, and A. C. Santomaso. Shear-induced particle segregation in binary mixtures: Verification of a percolation theory. *Particuology*, 57:214–222, 2021.

[24] J. Bridgwater, W. S. Foo, and D.J. Stephens. Particle Mixing and Segregation in Failure Zones - Theory and Experiment. *Powder Technology*, 41:147–158, 1985.

[25] P. Gajjar and J. M. N. T. Gray. Asymmetric flux models for particle-size segregation in granular avalanches. *Journal of fluid mechanics*, 757:297, 2014.

[26] L. Jing, C. Y. Kwok, and Y. F. Leung. Micromechanical origin of particle size segregation. *Physical review letters*, 118(11):118001, 2017.

[27] K. Van Der Vaart, M. P. Van Schrojenstein Lantman, T. Weinhart, S. Luding, C. Ancey, and A. R. Thornton. Segregation of large particles in dense granular flows suggests a granular Saffman effect. *Physical Review Fluids*, 3(7):1–12, 2018.

[28] L. Jing, J. M. Ottino, R. M. Lueptow, and P. B. Umbanhowar. Modified Archimedes' principle predicts rising and sinking of intruders in sheared granular flows. *arXiv*, 2 (2):22069, 2019.

[29] G. H. Ristow. *Pattern formation in granular materials*. Springer Science & Business Media, 2000.

[30] Y. Yu and H. Saxén. Experimental and dem study of segregation of ternary size particles in a blast furnace top bunker model. *Chemical engineering science*, 65(18): 5237–5250, 2010.

[31] W. A. Beverloo, H. A. Leniger, and J. Van de Velde. The flow of granular solids through orifices. *Chemical engineering science*, 15(3-4):260–269, 1961.

[32] M. C. Garcia, H. J. Feise, S. Strege, and A. Kwade. Segregation in heaps and silos: Comparison between experiment, simulation and continuum model. *Powder Technology*, 293:26–36, 2016.

[33] A. Samadani, A. Pradhan, and A. Kudrolli. Size segregation of granular matter in silo discharges. *Physical Review E*, 60(6):7203–7209, 1999.

[34] L. A. Golick and K. E. Daniels. Mixing and segregation rates in sheared granular materials. *Physical review E*, 80(4):042301, 2009.

[35] K. van der Vaart, P. Gajjar, G. Epely-Chauvin, N. Andreini, J. M. N. T. Gray, and C. Ancey. Underlying asymmetry within particle size segregation. *Physical review letters*, 114(23):238001, 2015.

[36] D. R. Tunuguntla, T. Weinhart, and A. R. Thornton. Comparing and contrasting size-based particle segregation models. *Computational particle mechanics*, 4(4):387–405, 2017.

[37] R. P. Jones, A. B. Isner, H. Xiao, J. M. Ottino, P. B. Umbanhowar, and R. M. Lueptow. Asymmetric concentration dependence of segregation fluxes in granular flows. *Physical Review Fluids*, 3(9):1–17, 2018.

Chapter 5

Size segregation in polydisperse granular mixtures

In chapter 4, we proposed a new continuum model for predicting segregation in multi-component mixtures of particles differing by size. However, real granular systems are not always made up of discrete size classes but are rather characterized by broad particle size distributions [1]. Thus, in this chapter, we present a theory for modelling segregation in polydisperse granular mixtures.

This work was done under the supervision of Dr Luca Mazzei of the University College London (UCL).

Parts of this chapter have been published:

M. Tirapelle, A. C. Santomaso, and L. Mazzei (2022). CFD-PBE coupled model for size-driven segregation in polydisperse granular flows. *Chemical Engineering Science*, 247, 117065, https://doi.org/10.1016/j.ces.2021.117065.

5.1 Introduction

Here, we propose a continuum model for segregation in polydisperse granular mixtures. This is a particular open area of research that is very important for understanding real industrial and geophysical systems [2]. To account for particle polydispersity and to describe the evolution in time and space of the particle size distribution, we use the Population Balance Equation (PBE) [3]. Although in theory PBEs can be solved analytically, only a few analytical solution strategies have been developed. Therefore, Population Balance Equations are usually solved numerically. Many numerical methods are available, such as the method of Laplace transforms, the method of moments, the method of weighted residuals and the Monte Carlo method [3, 4]. The Method of Moments, or MOM, is the most attractive one because it provides good results at a low computational cost [3]. It consists in tracking the lower-order moments of the distribution function with transport equations. In its classical form, the MOM has a few drawbacks. It requires that the functional form of the distribution function remain the same during the process. Furthermore, a moment closure problem arises: for any given set of moments the modeller wishes to track, higher-order moments feature in the transport equations [5, 6]. In the Quadrature Method of Moments (QMOM), the closure problem is overcome via a quadrature-based approximation of the particle size distribution. This formulation of the MOM was first developed by McGraw [7] for modelling the evolution of aerosols, and then further developed by Marchisio and co-workers for modelling crystal growth, aggregation and breakage [8, 9]. This approach still has a few drawbacks: the reconstruction of the distribution function from a finite set of moments is impossible unless one knows a-priori the functional form of the Particle Size Distribution (PSD), and the computational cost is higher than in MOM since weights and nodes have to be back-calculated from the moments of the distribution at each time step in each cell of the computational domain [3, 10, 11]. Furthermore, when a number of moments greater than four is tracked, the higher-order moments corrupt leading to non-physical values of quadrature nodes [11]. To overcome the disadvantages of the QMOM, Marchisio and Fox [12] proposed the Direct Quadrature Method of Moments (DQMOM). This differs from the QMOM because it tracks directly the weights and nodes of the quadrature approximation rather than tracking the moments of the PSD [3]. However, since both methods adopt the same approximation of the PSD, they are theoretically equivalent [1]. The Finite-size domain Complete set of trial functions Method Of Moments (FCMOM) by Strumendo and Arastoopour [10] is another promising formulation since it does not require specific assumptions for the distribution function and it converges fast to the solution of the PBE. It differs from the other approaches because it still solves the PBE in terms of its lower moments, but then reconstructs the distribution function itself [3]. However, since the FCMOM assumes that all particles, independently of their internal properties (e.g. size), are convected with an average phase velocity, it cannot be applied to model size-driven segregation (indeed to model size segregation, each quadrature class must be advected with its own velocity field).

Here, we implement the version of DQMOM developed by Mazzei et al. [13], in which the average phase velocity is replaced with a size-conditioned velocity. To determine the size-conditioned velocities, Mazzei et al. [13] used the averaged dynamical equations of multiphase flows, whereas we close them constitutively using a segregation-remixing model. The transport equations obtained from the DQMOM are then integrated within an Eulerian-Eulerian framework and solved in a Computational Fluid Dynamics (CFD) software.

The coupled CFD-PBE model is implemented to simulate the segregation dynamics of an inert, dry and cohesionless polydisperse powder, initially uniformly mixed, flowing down an inclined plane. To test the accuracy of the model, we compare its results to those of a Discrete Element Method (DEM) model. Even if the CFD-PBE model appears to be complex, it predicts well the evolution in time and space of the particle size distribution for a wide range of bed depths. Its main advantage with respect to DEM is that the required computation time is lower.

5.2 The population balance equation

The spatial and temporal evolutions of the particulate phase internal variable distribution function can be mathematically described at the mesoscopic level by the Generalized Population Balance Equation (GPBE) [5]. In what follows, we first express the GPBE in terms of Volume Density Function (VDF). Then, we reduce to one the dimensionality of the internal state space (see Section 5.2.1) and we approximate the VDF with a quadrature formula (see Section 5.2.3). The reduced PBE features an unclosed term: the size-conditioned velocity. As closure relation, we use a segregation-remixing model taken from the literature (see Section 5.2.2). The problem reduces to solving $2n$ transport equations for quadrature weights and weighted nodes where n is the number of classes in the quadrature approximation.

5.2.1 The Generalized PBE

In its classical form, the population-balance equation (PBE) is expressed in terms of the number density function, $f_n(\boldsymbol{\xi};\boldsymbol{x},t)$ [3, 13]:

$$\frac{\partial}{\partial t} f_n(\boldsymbol{\xi};\boldsymbol{x},t) + \nabla_x \cdot \left[f_n(\boldsymbol{\xi};\boldsymbol{x},t)\,\boldsymbol{v}\right] + \nabla_{\boldsymbol{\xi}} \cdot \left[f_n(\boldsymbol{\xi};\boldsymbol{x},t)\,\dot{\boldsymbol{\xi}}\right] = S_n(\boldsymbol{\xi};\boldsymbol{x},t) \ , \tag{5.1}$$

where $\boldsymbol{x}$ is the position vector in real space, $\boldsymbol{\xi} \equiv (\xi_1 ..., \ \xi_n)$ is the internal-coordinate vector (or property vector) and $\dot{\boldsymbol{\xi}}$ is the continuous rate of change in phase space [14]. In Eq. 5.1 the terms on the left-hand side are, in order: accumulation, advection in real space due to the velocity field $\boldsymbol{v}$ and advection in the internal state space. The source term on the right-hand side represents discontinuous jumps in phase space due to breakage, coalescence and/or reaction [14].

If the number density function includes also the particle-velocity vector as an internal mesoscale variable, the PBE becomes the generalized population-balance equation (GPBE):

$$\begin{gathered}\frac{\partial}{\partial t} f_n(\boldsymbol{v},\boldsymbol{\xi};\boldsymbol{x},t) + \nabla_x \cdot \left[f_n(\boldsymbol{v},\boldsymbol{\xi};\boldsymbol{x},t)\,\boldsymbol{v}\right] + \nabla_{\boldsymbol{v}} \cdot \left[f_n(\boldsymbol{v},\boldsymbol{\xi};\boldsymbol{x},t)\,\boldsymbol{A}_p\right] + \\ \nabla_{\boldsymbol{\xi}} \cdot \left[f_n(\boldsymbol{v},\boldsymbol{\xi};\boldsymbol{x},t)\,\dot{\boldsymbol{\xi}}\right] = S_n(\boldsymbol{v},\boldsymbol{\xi};\boldsymbol{x},t) \ .\end{gathered} \tag{5.2}$$

where $\boldsymbol{A}_p$ is the continuous rate of change of particle velocity (i.e. the velocity of the particles in the velocity subspace). Note that in the GPBE, there are never terms of diffusion in physical spaces. However, there could be diffusion terms in the velocity phase (e.g. in the case of inertial particles subjected to Brownian motion) [14]. The GPBE can also be written in terms of volume density functions, $f_v\left(\boldsymbol{v}, \boldsymbol{\xi}; \boldsymbol{x}, t\right) \equiv f_n\left(\boldsymbol{v}, \boldsymbol{\xi}; \boldsymbol{x}, t\right) v_p$. Multiplying the equation above by the particle volume, v_p, yields [15]:

$$\begin{gathered}\frac{\partial}{\partial t} f_v\left(\boldsymbol{v}, \boldsymbol{\xi}; \boldsymbol{x}, t\right) + \nabla_x \cdot \left[f_v\left(\boldsymbol{v}, \boldsymbol{\xi}; \boldsymbol{x}, t\right) \boldsymbol{v}\right] + \nabla_{\boldsymbol{v}} \cdot \left[f_v\left(\boldsymbol{v}, \boldsymbol{\xi}; \boldsymbol{x}, t\right) \boldsymbol{A}_p\right] + \\ \nabla_{\boldsymbol{\xi}} \cdot \left[f_v\left(\boldsymbol{v}, \boldsymbol{\xi}; \boldsymbol{x}, t\right) \dot{\boldsymbol{\xi}}\right] v_p = S_v\left(\boldsymbol{v}, \boldsymbol{\xi}; \boldsymbol{x}, t\right) \; .\end{gathered} \tag{5.3}$$

Note that, in this case, the source term accounts for discontinuous jumps both in the velocity state space due to particle collisions and in the size space caused by aggregation and breakage. Furthermore, v_p is a constant with respect to $\boldsymbol{v}$, $\boldsymbol{x}$ and t and thus, it is not included under the sign of partial derivation [15].

To model segregation, let us consider a particle population characterized by two internal coordinates: the particle size ξ (a scalar quantity) and the particle velocity $\boldsymbol{v}$ (a vector quantity). The volume density function $f_v\left(\boldsymbol{v}, \xi; \boldsymbol{x}, t\right)$ represents the volume of particles with size ξ in the range $\mathrm{d}\xi$ and velocity $\boldsymbol{v}$ in the range $\mathrm{d}\boldsymbol{v}$ that are, at time t, contained in the volume $\mathrm{d}\boldsymbol{x}$ around $\boldsymbol{x}$. If neither reactions nor attrition occur (i.e. ξ does not vary continuously and the particles have zero velocity in size space), the GPBE governing the evolution of the volume density function for the system under investigation is [13]:

$$\begin{gathered}\frac{\partial}{\partial t} f_v\left(\boldsymbol{v}, \xi; \boldsymbol{x}, t\right) + \nabla_x \cdot \left[f_v\left(\boldsymbol{v}, \xi; \boldsymbol{x}, t\right) \boldsymbol{v}\right] + \\ \nabla_{\boldsymbol{v}} \cdot \left[f_v\left(\boldsymbol{v}, \xi; \boldsymbol{x}, t\right) \boldsymbol{A}_p\left(\boldsymbol{v}, \xi; \boldsymbol{x}, t\right)\right] = S_v\left(\boldsymbol{v}, \xi; \boldsymbol{x}, t\right) \; .\end{gathered} \tag{5.4}$$

Solving Eq. 5.4 is extremely difficult: it is an integro-differential equation with respect to the internal variables and its dimensionality is higher than the classical transport equations (it is four-dimensional in its internal state space) [3, 10, 13]. To reduce the dimensionality of the internal state space, we integrate out the coordinate $\boldsymbol{v}$, so Eq. 5.4 reduces to:

$$\frac{\partial}{\partial t} \hat{f}_v\left(\xi; \boldsymbol{x}, t\right) + \nabla_x \cdot \left[\hat{f}_v\left(\xi; \boldsymbol{x}, t\right) \tilde{\boldsymbol{v}}(\xi; \boldsymbol{x}, t)\right] = 0 \, , \tag{5.5}$$

where, by definition, it is:

$$\hat{f}_v\left(\xi; \boldsymbol{x}, t\right) \equiv \int_{\Omega_v} f_v\left(\boldsymbol{v}, \xi; \boldsymbol{x}, t\right) \mathrm{d}\boldsymbol{v} \, , \tag{5.6}$$

$$\hat{f}_v\left(\xi; \boldsymbol{x}, t\right) \tilde{\boldsymbol{v}}(\xi; \boldsymbol{x}, t) \equiv \int_{\Omega_v} f_v\left(\boldsymbol{v}, \xi; \boldsymbol{x}, t\right) \boldsymbol{v} \mathrm{d}\boldsymbol{v} \, , \tag{5.7}$$

with $\Omega_v \equiv \mathbb{R}$ denoting the domain of variation of $\boldsymbol{v}$. In the reduced PBE (Eq. 5.5), since the particle velocity is no longer an internal coordinate, the source term vanishes because no discontinuous jumps take place in the size space (i.e. particles neither aggregate nor break) and $\hat{f}_v\left(\xi; \boldsymbol{x}, t\right)$ is a monovariate VDF with particle size being its only internal state variable. There is, however, an unclosed term: the mean velocity conditioned on the particle size $\tilde{\boldsymbol{v}}(\xi;\boldsymbol{x},t)$. To close $\tilde{\boldsymbol{v}}$ one must either solve a balance equation, as done by Mazzei et al. [13], or use a constitutive relation. In this chapter, we employ a constitutive relation.

5.2.2 Size-conditioned velocity

In dense, gravity-driven, free-surface flows of granular avalanches with dissimilar grains, segregation takes place. Two are the competitive mechanisms characterising segregation: gravity-driven size segregation and diffusive remixing caused by the random motion of the particles as they collide and shear over one another [16–18]. Gravity-driven size segregation is the combination of kinetic sieving and squeeze expulsion; it results in a net segregating flux of the smaller particles downwards and the larger particles upwards [17]. Competing against segregation, there is diffusive remixing [18]. To account for remixing, one includes a diffusional term in the model, and therefore an associated diffusion coefficient $\mathcal{D}$. Unfortunately, there is no theory on diffusion that applies to dense polydisperse granular flows, so here we assumed that diffusion is isotropic and that $\mathcal{D}$ is a constant (i.e. it does not even depend on the particle size). Particles are then conveyed by the main solid flow, whose velocity (i.e. the Eulerian velocity of the mixture) is governed by the dynamical equation of the mixture.

In light of these considerations, three terms contribute to the mass flux of the particles in a gravity-driven size segregating system: 1) a segregative flux caused by kinetic sieving and squeeze expulsion, 2) a diffusive flux responsible for remixing and 3) an advective flux that conveys particles down-slope. We can thus write:

$$\begin{gathered}\hat{f}_v(\xi;\boldsymbol{x},t)\tilde{\boldsymbol{v}}(\xi;\boldsymbol{x},t) = \hat{f}_v(\xi;\boldsymbol{x},t)\boldsymbol{v}_s(\xi;\boldsymbol{x},t) + \\ \hat{f}_v(\xi;\boldsymbol{x},t)\boldsymbol{v}_b(\boldsymbol{x},t) - \mathcal{D}\nabla_x \hat{f}_v\,(\xi;\boldsymbol{x},t)\ ,\end{gathered} \tag{5.8}$$

where $\boldsymbol{v}_b(\boldsymbol{x},t)$ is the Eulerian velocity of the solid mixture and $\boldsymbol{v}_s(\xi;\boldsymbol{x},t)$ is the size-dependent segregation velocity.

If we consider a chute flow, the coordinate system has the x-, y- and z-axis in the stream-wise, span-wise and surface normal direction, respectively. Thus, the y-component of the segregation velocity is much smaller than the other two components (i.e. $v_{s,y} \approx 0$ is negligible) and the segregation velocity in Cartesian index notation reads:

$$\boldsymbol{v}_s(\xi;\boldsymbol{x},t) = v_{s,x}(\xi;\boldsymbol{x},t)\boldsymbol{e}_x + v_{s,z}(\xi;\boldsymbol{x},t)\boldsymbol{e}_z\,. \tag{5.9}$$

To model the x- and z-components of the segregation velocity, different segregation laws can be employed, since a general and valid description of the continuum segregation model is still lacking. In this study, we arbitrarily choose the expression proposed by Marks et al.

[19]:

$$v_{s,x}(\xi;\boldsymbol{x},t)=\dot{\gamma}\left(\frac{g\cdot\sin\theta}{c}\right)(f_c-1)\ , \tag{5.10}$$

$$v_{s,z}(\xi;\boldsymbol{x},t)=\dot{\gamma}\left(\frac{g\cdot\cos\theta}{c}\right)(f_c-1)\ , \tag{5.11}$$

where g is the acceleration due to gravity, θ is the angle of inclination with respect to the horizon, $\dot{\gamma}$ is the shear rate and c is a coefficient of inter-particle drag with unit of $1/\mathrm{s}^{-2}$. About c, its nature is still poorly understood, so we assume that c is constant. We also assume that the scaling factor for the multicomponent case, f_c, scales with the characteristic length of the particle, namely with the particle size ξ [19, 20]:

$$f_c=\frac{\xi}{\int_0^\infty \hat{f}_v(\xi;\boldsymbol{x},t)\xi\mathrm{d}\xi}\,. \tag{5.12}$$

Note that one could employ other forms for the percolation velocity. Introducing Eq. 5.8 in the reduced population balance equation (Eq. 5.5) gives:

$$\frac{\partial}{\partial t}\hat{f}_v+\nabla_x\cdot\left(\hat{f}_v\boldsymbol{v}_b\right)+\nabla_x\cdot\left(\hat{f}_v\boldsymbol{v}_s\right)-\mathcal{D}\nabla_x^2\hat{f}_v=0\,. \tag{5.13}$$

This equation governs the evolution of the monovariate VDF, $\hat{f}_v\,(\xi;\boldsymbol{x},t)$. The model relies on two parameters: the drag coefficient (i.e. c) and the diffusivity. We will see in Section 5.2.3 that, because of the inclusion of diffusion, a source term will appear in the DQMOM transport equations.

5.2.3 Direct Quadrature Method of Moments

There are many solution methods for population balance equations such as the method of Laplace transform, the method of moments, the method of weighted residuals and the Monte Carlo method [3]. However, for practical needs, knowing the evolution of the first few moments of the VDF is enough to fulfil engineering requirements [4]. Thus, in this study, we solve the population balance equation with the direct quadrature method of moments. The volume density function $\hat{f}_v$ in Eq. 5.13 is approximated as a summation of n Dirac delta functions:

$$\hat{f}_v\approx\sum_{\alpha=1}^{n}\phi_\alpha(\boldsymbol{x},t)\delta\left(\xi-\xi_\alpha(\boldsymbol{x},t)\right)\ , \tag{5.14}$$

where n is the number of classes of the quadrature approximation, while ϕ_α and ξ_α are the weights and nodes of the α-th quadrature class, respectively.

We assume that the void fraction $\varepsilon\equiv 1-\nu$ is uniform within the solid domain and equal to 0.37. Thus, the overall solid volume fraction is everywhere equal to $\nu=0.63$. Because of this assumption, we could work in terms of void-free VDF (i.e. the sum of its weights is one), and so void-free quadrature weights in the quadrature formula. From now on, we refer to $\hat{f}_v$ as void-free VDF. Introducing the void-free VDF as expressed in Eq. 5.14 into Eq. 5.13 gives:

$$\begin{gathered}\frac{\partial}{\partial t}\left(\sum_{\alpha=1}^{n}\phi_\alpha\delta\left(\xi-\xi_\alpha\right)\right)+\nabla_x\cdot\left(\sum_{\alpha=1}^{n}\phi_\alpha\delta\left(\xi-\xi_\alpha\right)\boldsymbol{v}_b\right)+\\ \nabla_x\cdot\left(\sum_{\alpha=1}^{n}\phi_\alpha\delta\left(\xi-\xi_\alpha\right)\boldsymbol{v}_{s,\alpha}\right)-\mathcal{D}\nabla_x^2\left(\sum_{\alpha=1}^{n}\phi_\alpha\delta\left(\xi-\xi_\alpha\right)\right)=0\,,\end{gathered}\tag{5.15}$$

where $\boldsymbol{v}_{s,\alpha}(\boldsymbol{x},t)$ is the segregation velocity of the particles belonging to the quadrature class α. Since both $\phi_\alpha(\boldsymbol{x},t)$ and $\xi_\alpha(\boldsymbol{x},t)$ are functions of the real space coordinates and the time, Eq. 5.15 yields:

$$\begin{gathered}\sum_{\alpha=1}^{n}\Big[c_\alpha^{\phi}(\boldsymbol{x},t)\delta\left(\xi-\xi_\alpha\right)-(c_\alpha^{\phi\xi}(\boldsymbol{x},t)-\xi_\alpha c_\alpha^{\phi}(\boldsymbol{x},t))\delta'\left(\xi-\xi_\alpha\right)\Big]=\\ \sum_{\alpha=1}^{n}\left[\mathcal{D}\delta''\phi_\alpha\nabla_x\xi_\alpha\cdot\nabla_x\xi_\alpha\right]\,,\end{gathered}\tag{5.16}$$

where by definition it is:

$$\frac{\partial}{\partial t}\phi_\alpha+\nabla_x\cdot(\phi_\alpha\boldsymbol{v}_b)+\nabla_x\cdot(\phi_\alpha\boldsymbol{v}_{s,\alpha})-\mathcal{D}\nabla_x^2\phi_\alpha\equiv c_\alpha^{\phi}\,,\tag{5.17}$$

$$\frac{\partial}{\partial t}\sigma_\alpha+\nabla_x\cdot(\sigma_\alpha\boldsymbol{v}_b)+\nabla_x\cdot(\sigma_\alpha\boldsymbol{v}_{s,\alpha})-\mathcal{D}\nabla_x^2\sigma_\alpha\equiv c_\alpha^{\sigma}\,,\tag{5.18}$$

with $\sigma_\alpha\equiv(\phi_\alpha\xi_\alpha)$ being the α-*th* weighted node. Complete proof of the derivation of the DQMOM transport equations (i.e. Eqs. 5.17 and 5.18) is given in A.3 of Appendix A.

Equation 5.16 expresses the population balance equation for a monovariate population of particles whose size-conditioned velocity is closed as reported in Section 5.2.2. The unknown functions are $\phi_\alpha(\boldsymbol{x},t)$ and $\xi_\alpha(\boldsymbol{x},t)$, namely the weights and the nodes of the quadrature approximation. Also, the source terms $c_\alpha^{\phi}(\boldsymbol{x},t)$ and $c_\alpha^{\phi\xi}(\boldsymbol{x},t)$ are unknowns, but they can be determined by computing the moment transforms of the PBE, namely by forcing the quadrature-based VDF to agree with the first $2n$ integer moments of the actual VDF [6]. By definition, the *k-th* order integer moment of $\hat{f}_v$, with $\hat{f}_v$ approximated as reported in Eq. 5.14, reads:

$$\mathscr{M}_k\equiv\int_0^\infty\xi^k\hat{f}_v\left(\xi;\boldsymbol{x},t\right)\mathrm{d}\xi\approx\sum_{\alpha=1}^{n}\phi_\alpha(\boldsymbol{x},t)\xi_\alpha^k(\boldsymbol{x},t)\,.\tag{5.19}$$

If we apply this transform to each term of Eq. 5.16 (for proof, refer to A.4 of Appendix

A), we obtain a linear algebraic system in the $2n$ unknown source terms c_α^ϕ and $c_\alpha^{\phi\xi}$:

$$\begin{gathered}\sum_{\alpha=1}^{n} c_\alpha^\phi \xi_\alpha^k + k\sum_{\alpha=1}^{n}(c_\alpha^{\phi\xi} - \xi_\alpha c_\alpha^\phi)\xi_\alpha^{k-1} = \\ k(k-1)\sum_{\alpha=1}^{n} \mathcal{D}\phi_\alpha \xi_\alpha^{k-2} \nabla_x \xi_\alpha \cdot \nabla_x \xi_\alpha\,,\ k \in [0, 2n-1]\ .\end{gathered} \tag{5.20}$$

If we employ a two-node quadrature approximation, we obtain four source terms:

$$\begin{cases} c_1^\phi(\boldsymbol{x},t) = -6(\chi_1 - \chi_2)(\xi_1 - \xi_2)^{-2}\,, \\ c_1^{\phi\xi}(\boldsymbol{x},t) = [2\chi_2(2\xi_1 + \xi_2) - 2\chi_1(\xi_1 + 2\xi_2)](\xi_1 - \xi_2)^{-2}\,, \\ c_2^\phi(\boldsymbol{x},t) = -c_1^\phi(\boldsymbol{x},t)\,, \\ c_2^{\phi\xi}(\boldsymbol{x},t) = -c_1^{\phi\xi}(\boldsymbol{x},t)\,, \end{cases} \tag{5.21}$$

where the subscript 1 or 2 indicates the quadrature class, and χ_α is equal to:

$$\chi_\alpha \equiv \mathcal{D}\phi_\alpha \nabla_x \xi_\alpha \cdot \nabla_x \xi_\alpha\,. \tag{5.22}$$

Once the source terms are known, solving the PBE reduces to solving Eqs. 5.17 and 5.18 for each quadrature class. If one wants to track directly the evolution in time and space of the quadrature nodes instead of the weighted nodes, the transport equation would be:

$$\frac{\partial}{\partial t}\xi_\alpha + \boldsymbol{v}_b \cdot \nabla_x \xi_\alpha + \boldsymbol{v}_{s,\alpha} \cdot \nabla_x \xi_\alpha - \mathcal{D}\nabla_x^2 \xi_\alpha = c_\alpha^\xi\,, \tag{5.23}$$

with the source term equal to:

$$c_\alpha^\xi \equiv \frac{c_\alpha^\sigma - c_\alpha^\phi \xi_\alpha + 2\mathcal{D}\nabla_x \phi_\alpha \cdot \nabla_x \xi_\alpha}{\phi_\alpha}\,. \tag{5.24}$$

This is formally demonstrated in A.3 of Appendix A.

As explained in Mazzei [6], the diffusive terms generate the source terms. In our case, spatial diffusion arises in the transport equations because $\boldsymbol{v}_\alpha$ has been closed using the segregation-remixing model, which is made of two competitive mechanisms: gravity-driven segregation and diffusive remixing. Thus, since we have diffusion, we also have generation. Furthermore, diffusion consents micromixing: each element can interact with the other elements within the domain so that powders are allowed to mix also at the microscopic length scale [6, 13].

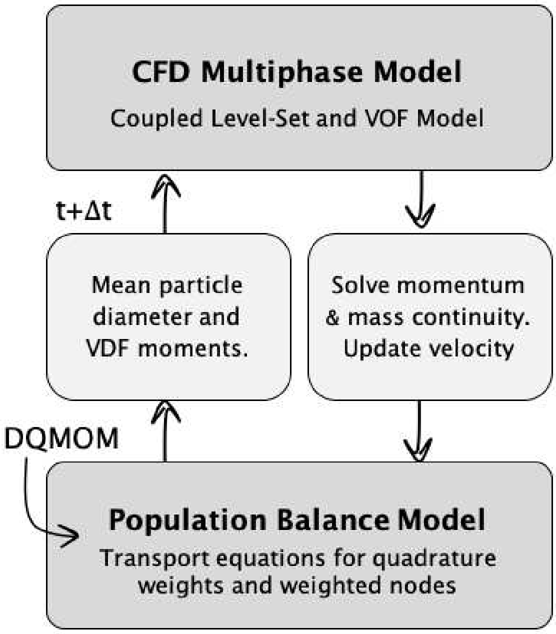

Figure 5.1: Schematic diagram of the CFD-PBE coupled model. The PBE is solved by adopting the DQMOM.

5.3 Multiphase fluid dynamic model

5.3.1 CFD-PBE coupling

Process operations such as storage, conveying, mixing and sizing of particles range from small scale (e.g. pharmaceutical industries) to large scale (e.g. minerals industries). Simulating large-scale systems via DEM may be unfeasible because of the required computational effort and time. However, to cope with a full-scale industrial system, one can use computational fluid dynamic simulations. For this reason, we developed a segregation CFD-PBE coupled model to be implemented in a CFD code. The flowchart of the CFD-PBE coupled model is reported in Fig. 5.1. We simulated a two-phase system consisting of two phases: the granular mixture flowing down an inclined plane, and the air lying above the mixture. We used the VOF modelling approach, which allows calculating the velocity and volume fraction profiles in the two phases. The volume fraction is uniform in the bulk of each phase, varying only near the interface between the two phases. The velocity field in the granular phase coincides with $\boldsymbol{v}_b$, the bulk velocity featuring in the PBE (see Eq. 5.13). Once the segregation fluxes are obtained, the PBE is solved by adopting the DQMOM. Since segregation determines changes in the local rheology, and consequently the flow, the nodes and weights of the quadrature approximations are then fed back into the CFD model and used to update the local rheology of the bulk solid at the subsequent time step.

5.3.2 Multifluid dynamical equations

We considered a polydisperse powder flowing down an inclined plane under gravity and in ambient conditions. We limited our investigation to a two-dimensional incompressible granular flow. As already mentioned, we assumed that the mean solid volume fraction is constant within the powder bed [21]. Because of these assumptions, the polydisperse granular material can be represented as a single continuous phase. The second phase is instead superficial ambient air. The two phases do not interpenetrate, and mass transfer does not occur.

As Eulerian-Eulerian multiphase model, we employed the coupled level-set and volume of fluid (VOF) method, a numerical technique designed for immiscible fluids that allows tracking the position of the interface. In the VOF method, pressure and velocity field are found by solving the mass and momentum conservation equations (Eqs. 2.20 and 2.21) with density and viscosity defined respectively as:

$$\rho = (1-\alpha_s)\rho_{air} + \alpha_s \rho_s \,, \tag{5.25}$$

$$\eta = (1-\alpha_s)\eta_{air} + \alpha_s \eta_s \,, \tag{5.26}$$

where α_s is the volume fraction of solid. The discontinuity across the interface is smooth, whereas, away from the interface, air and solid maintain their characteristic properties [22, 23]. The volume fraction of the solid phase is obtained by solving the transport equation:

$$\frac{\partial \alpha_s}{\partial t} + \nabla \cdot (\alpha_s \boldsymbol{u}) = 0 \,, \tag{5.27}$$

whereas, the volume fraction of air is $\alpha_{air} = 1 - \alpha_s$. As concerns the interface between air and solid, it is captured by the level-set method (see Section 2.3.3).

5.3.3 Effective stress tensor

The closure of the effective stress tensor is achieved by the implementation of the incompressible $\mu(I)-$ rheology proposed by the Groupement De Recherche Milieux Divisés [24] since it is a well-established rheology for chute flows. As discussed in Section 2.2.2.2, the incompressible $\mu(I)$ rheology states that the friction coefficient μ is rate-dependent and scales with the inertial number I (see Eq. 2.41) [24, 25]. For polydisperse granular materials, we proposed the following expression for I:

$$I = \frac{\bar{\mathcal{D}}\dot{\gamma}}{\sqrt{p/\rho^*}} \,, \tag{5.28}$$

where $\bar{\mathcal{D}}$ is the average diameter of the PSD (see Eq. 2.50). Note that, to implement this rheology in Ansys Fluent, we resorted to customized user defined functions.

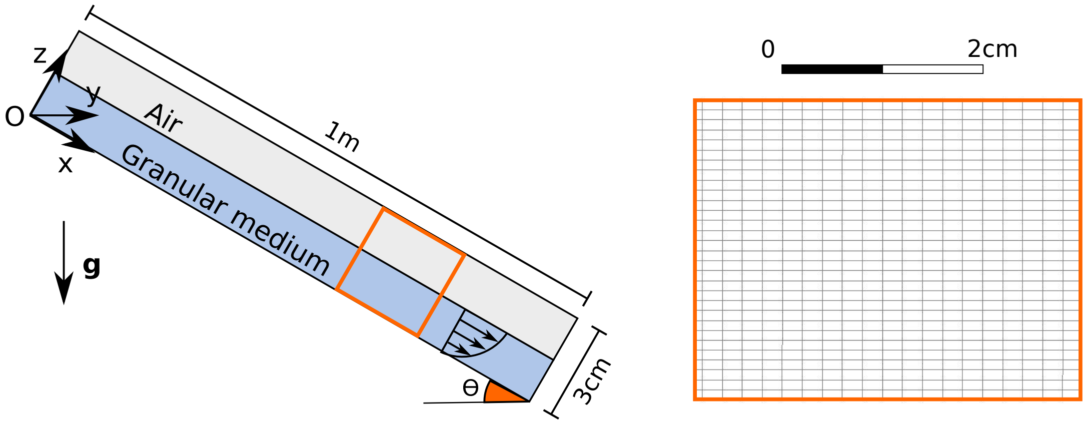

Figure 5.2: On the left: a sketch of the simulated system and the coordinate system. The blue shaded area represents the solid phase and θ is the inclination angle of the chute. On the right: a piece of the 2D mesh employed in the CFD simulation.

5.4 Materials and methods

5.4.1 CFD implementation

The CFD-PBE coupled model was implemented in a CFD code to predict the evolution of the PSD of a polydisperse system flowing down an inclined plane. This section gives detailed information about the framework and numerical scheme.

5.4.1.1 Framework

We considered a polydisperse powder flowing down an inclined plane. The angle of inclination is $\theta = 30^o$ with respect to the horizon and the powder is subjected to gravity. Fig. 5.2 reports a sketch of the system. The granular material is represented as a single solid phase, with a bulk density equal to $\rho_s = 1260$ kg/m^3. This choice is motivated by the fact that the solid volume fraction is assumed uniform and constant within the powder bed. Even though all the particles are advected within the bulk flow, we could track the downward relative motion between particles of different sizes thanks to the DQMOM transport equations (see Section 5.2.3). The primary phase, air, is represented with a density of 1.225 kg/m^3 and a viscosity of $1.7894{\cdot}10^{-5}$ Pa s.

5.4.1.2 Numerical scheme

To run the simulations, we used the commercial CFD code Ansys Fluent 17.2. As multi-fluid model, we employed the coupled level-set and volume of fluid method. The primary phase is ambient air whereas the secondary phase is the bulk solid. The solid phase is composed of a polydisperse mixture of grains whose particle size distribution is approximated with a two-node quadrature formula. The quadrature weights and the quadrature weighted nodes were treated as user scalars, and their transport equations (Eqs. 5.17 and

5.18) were added to the default equations of the code. We also implemented the closure for the solid frictional viscosity through user-defined functions.

We used the pressure-based solver, which is recommended for low-speed incompressible flows. To convert scalar transport equations into algebraic equations that are numerically solvable, the code adopts a finite-volume discretization scheme. For what concerns spatial discretization, we used the Least Squares Cell-Based algorithm. We set a second-order accurate level-set method, whereas momentum and user-defined scalars were discretized through a first-order upwind scheme. Temporal discretization was first-order accurate and implicit. To couple pressure and velocity, we adopted the SIMPLE (Simultaneous Solution of Non-linearly Coupled Equations) algorithm. We then adopted the compressive interface capturing scheme, which is particularly suitable for flows with high ratios of viscosities between the phases. The pressure values at the cell face were interpolated by a body-force-weighted scheme. To compute the flow variables, we used a maximum of 20 iterations for each time step. Setting the tolerance of all the variables equal to 10^{-3}, we usually attained convergence within the iteration limit. The time step was set to 10^{-3} s.

5.4.1.3 Boundary and initial conditions

The simulation domain is an inclined chute 1 m long and 3 cm high represented as a two-dimension computational grid. The effect of the front and back walls is therefore neglected. The mesh is uniform almost everywhere, with 15090 cells of 2 x 1 mm size (see Fig. 5.2). We assigned a no-slip boundary condition at the bottom wall [26, 27] and 100 Pa gauge pressure at the domain upper boundary and outlet boundary. Concerning the inflow, after several trial experiments, we saw that a good feed rate to induce a stable flow [27] can be obtained by imposing a constant inlet velocity of 0.35 m/s for the solid phase.

In its initial state, the bulk solid is uniformly well-mixed and fill the chute height up to $H = 1.5$ cm. To assign the initial conditions, we need to know the values of the n quadrature weights and n quadrature nodes at time 0 and everywhere within the computational domain. For this purpose, we had first to calculate the first $2n$ order moments by implementing Eq. 5.19 to the volume density function of the particle size distribution (which is known). Since the quadrature approximation is Gaussian, the quadrature nodes and weights can be efficiently obtained from the moments of the density function by adopting the product-difference algorithm of Gordon [7]. Fig. 5.3 shows the continuous particle size distribution of our granular system considering 10 different size classes (in reality the PSD is usually determined by sieve analysis and thus expressed in terms of discrete sizes) and its two-node representation. The values of its first four integer moments are reported, together with quadrature nodes and weights, in Tab. 5.1. Note that the zeroth-order moment is equal to one since we are considering a void-free VDF. Finally, since the inflow is constant and uniform, we imposed constant fluxes of the user-defined scalars at the solid inlet.

We ran the CFD simulation assuming constant drag and diffusion coefficients. Fol-

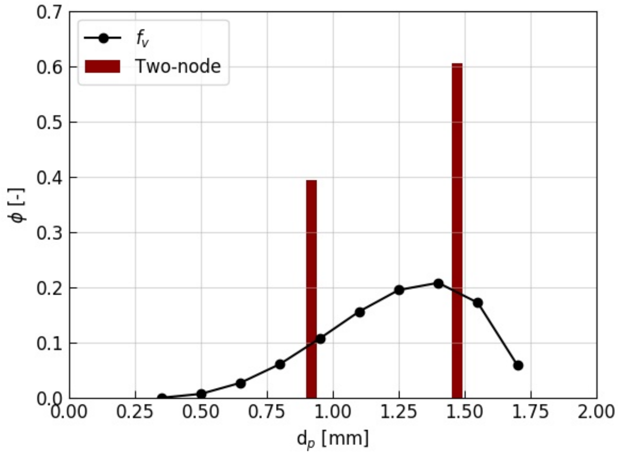

Figure 5.3: The simulated PSD is expressed in terms of 10 different size classes and a two-node representation. The positions and the heights of the vertical lines represent the Dirac delta functions of the quadrature formula.

Moments of the VDF			
$\mathcal{M}_0$ [-]	$\mathcal{M}_1$ [mm]	$\mathcal{M}_2$ [mm^2]	$\mathcal{M}_3$ [mm^3]
1	1.2535	1.6440	2.2346
Quadrature nodes and weights			
ξ_1 [mm]	ϕ_1 [-]	ξ_2 [mm]	ϕ_2 [-]
0.92	0.394	1.47	0.606

Table 5.1: Values of the VDF moments, quadrature nodes and weights obtained from the PSD reported in Fig. 5.3

lowing Marks et al. [19], the diffusion coefficient had to be of the order of magnitude of $\mathcal{D} \sim 10^{-5}$ m^2/s. About the drag coefficient, suitable values that lead to reasonable segregation velocities are about $c \sim 10^4 - 10^5$ s^{-2}. Thus, we imposed $\mathcal{D} = 1.2 \cdot 10^{-5}$ m^{2}s^{-1} and $c = 6 \cdot 10^4$ s^{-2}. Furthermore, we set $\mu_s = 0.176$, $\mu_2 = 0.643$ and $I_0 = 0.279$.

5.4.2 DEM validation

The challenge is to validate the results of the CFD-PBE coupled model. A valuable tool to test and calibrate continuum models when experimental observations are unfeasible (e.g. it is difficult to measure the evolving particle-size distribution of polydisperse systems during flow) is represented by Discrete Element Method (DEM) simulations [28]. The 3D soft-sphere simulation was implemented in LIGGGHTS®-PUBLIC. As contact force model, we employed the non-linear spring-dashpot model developed by Hertz and Mindlin [29, 30] with constant directional torque (for detail refer to Section 2.2.1). We simulated only a sector of the full geometry thus, periodic boundary conditions were imposed in both the stream-wise (x) and span-wise (y) directions. To avoid plug flow, the bottom

Variable	**Symbol**	**Value**
Particle density [kg/m^3]	ρ_s^*	2000
Young's modulus [MPa]	E	26
Poisson ratio	σ	0.25
Sliding friction coefficient	μ_s	0.56
Rolling friction coefficient	μ_r	0.001
Restitution coefficient	e_n	0.60
Number of particles	N_T	3000
Time step [s]	Δt	1e−6
Boundary conditions	−	p p f

Table 5.2: A summary of the DEM simulation parameters. The Young's modulus, Poisson ratio and restitution coefficient are taken from Jain et al. [32].

wall must be a rough surface. To model roughness, we fixed some particles to the base [31].

The system was filled with a total of 3000 particles, all having the same intrinsic density ($\rho^* = 2000\text{kg/m}^3$). Unlike Marks et al. [19], who simulated a polydisperse mixture of spheres distributed uniformly, we implemented a non-uniform particle size distribution (i.e. the 10 different size classes reported in Fig. 5.3). The computational time step was set equal to 10^{-6} s, smaller than the critical time step (see 2.2.1.3). The simulation parameters and the material properties are summarized in Tab. 5.2.

The simulation was initialized with gravitational acceleration acting in the negative z-direction (i.e. the plane is horizontal). The particles were generated within the simulation domain and let settle by gravity. Once settled, the gravity vector was rotated to simulate the inclination angle θ. At that point, particles started to avalanche down-slope.

5.5 Results and discussion

In this section, we report in order: the results from the CFD simulation, the results from the DEM simulation and their comparison. In both cases, to evaluate segregation, we divide the domain into three superimposed layers: a bottom layer, a top layer and a middle layer sandwiched in between. Each layer is 4 mm high in the z-direction.

5.5.1 CFD-PBE coupled model simulations

Let us consider three investigation windows referred to as A, B and C that are located close to the inlet, in the middle, and near the outlet of the domain, respectively. A visual representation of these windows can be seen in Fig. 5.4, whereas Figs. 5.5 and 5.6 represent the profiles of the quadrature weights and quadrature nodes in the three locations after 1 and 8 seconds, respectively. We can see that the segregation features enhance with time

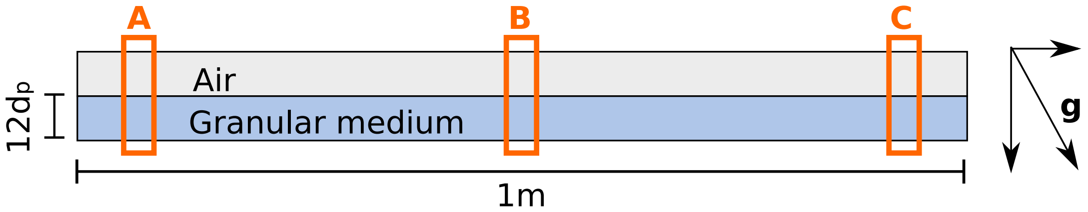

Figure 5.4: Sketch of the simulation domain. A, B and C indicate the three locations where the quadrature weights and quadrature nodes are mapped in Figs. 5.5 and 5.6.

and along the flow direction until a steady-state configuration is reached. Furthermore, closer to the bottom wall the flow is enriched with smaller particles.

As already mentioned, the CFD simulations give as output the values of the quadrature weights and nodes in each computational cell of the domain. From these values, we can obtain the cell values of the first four integer moments by implementing Eq. 5.19. Starting from the numerical profiles of the VDF moments, we can then determine the average values of the moment in each layer of the computational domain. As an example, Fig. 5.7 shows the evolution in time of the first raw moment, which represents the mean particle diameter, considering an investigation window positioned 0.8 ± 0.1 m from the inlet (as the inflow is constant and homogeneous). We can distinguish three inversely graded segregated layers characterized by finer particles at the bottom, coarser grains on top, and medium-sized particles in between. This means that, as expected, smaller particles have, on average, a net downward motion. Particles segregate by size and segregation is even more pronounced at the bottom where the shear rate is higher. The corresponding average values of the two quadrature nodes evolving in time, still for the three layers, is shown in Figs. 5.8 and 5.9.

5.5.2 DEM simulation

The DEM simulation treats a section 2 cm long and 1 cm wide of the full geometry considered in the CFD simulation; this is because simulating the entire geometry would require more than $1.5 \cdot 10^5$ particles.

Fig. 5.10 displays three snapshots of the simulation, where the different colours denote different sized particles. At time $t = 0$ s particles are homogeneously distributed, whereas at time $t = 6$ s the system has already reached its final steady state.

Unlike continuum models, the results of DEM simulations yield the position of each particle at any given time. This allowed us to determine the numerical fraction of each size class in each layer, to reconstruct the PSD in terms of volume density function (see. Fig. 5.11), and to calculate the first four moments of the distribution. The smaller particles collect preferentially close to the bottom, whereas the top is richer in bigger particles. From the VDF moments, we back-calculated the two weights and two nodes of the distribution by employing the product-difference algorithm of Gordon [33]. These are used in the following section for model validation.

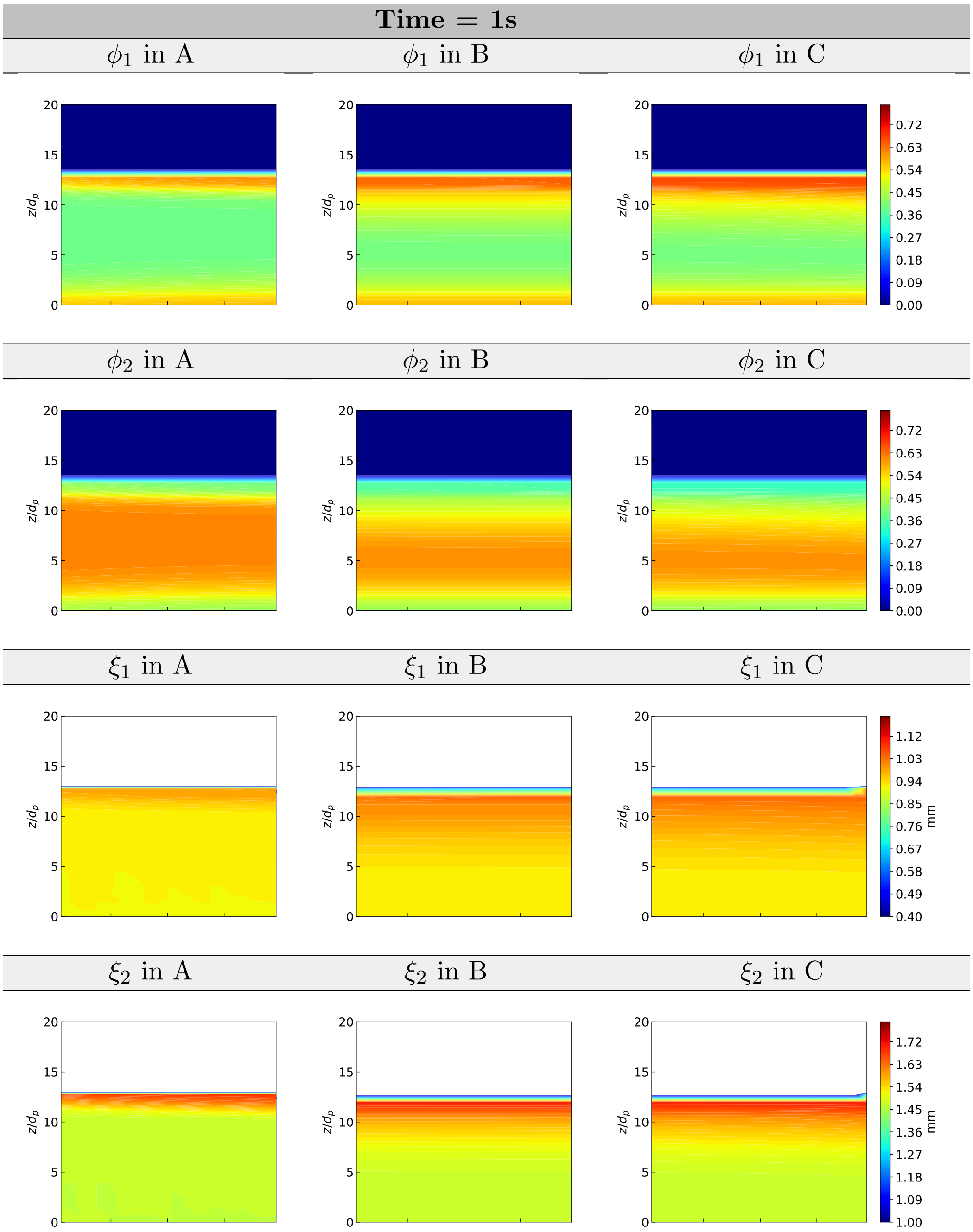

Time = 1s

ϕ_1 in A ϕ_1 in B ϕ_1 in C

ϕ_2 in A ϕ_2 in B ϕ_2 in C

ξ_1 in A ξ_1 in B ξ_1 in C

ξ_2 in A ξ_2 in B ξ_2 in C

Figure 5.5: Contour plot of (by row) the quadrature weights and quadrature nodes at $t = 1$s and (by column) at the three different locations represented in Fig. 5.4.

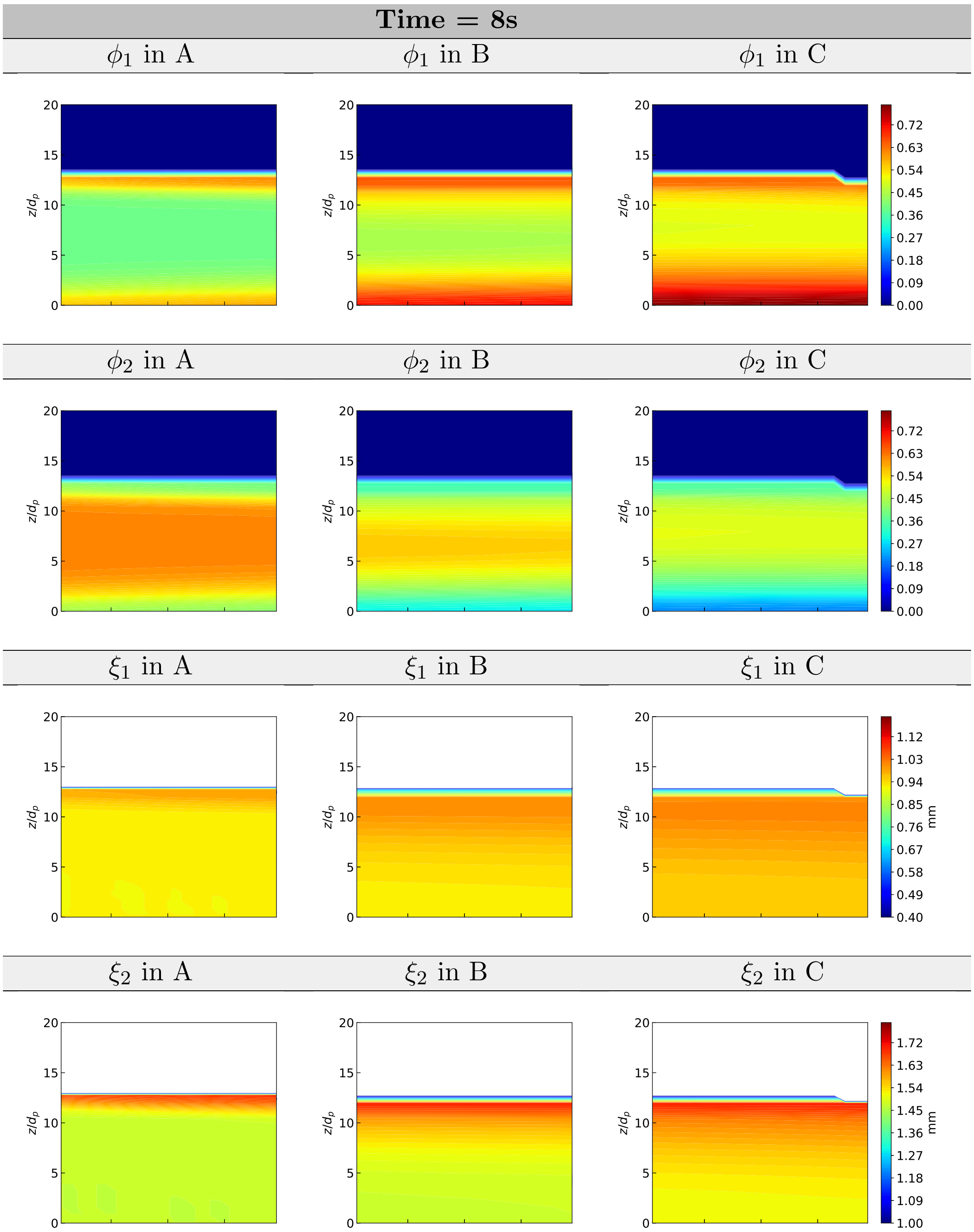

Figure 5.6: Contour plot of (by row) the quadrature weights and quadrature nodes at $t = 8$s and (by column) at the three different locations represented in Fig. 5.4.

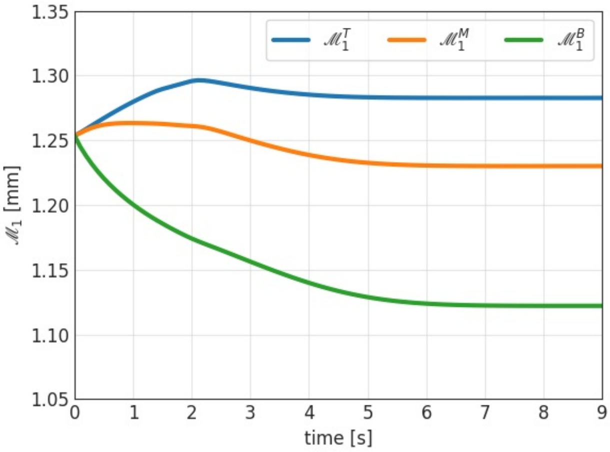

Figure 5.7: Evolution of the first-order moment of the PSD in the bottom, middle and top layers obtained by solving the CFD-PBE coupled model.

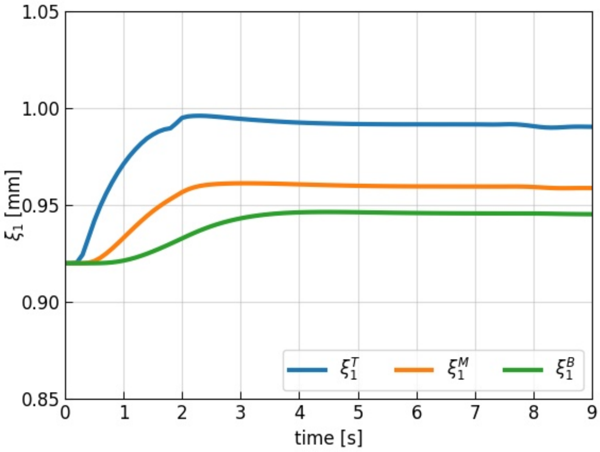

Figure 5.8: Evolution of the first quadrature node in the bottom, middle and top layer obtained by solving the CFD-PBE coupled model.

5.5.3 Confirming the model

First, we wanted to verify that the velocity field is correctly predicted by the rheological model. We, therefore, performed preliminary simulations both in CFD and DEM considering a monodisperse bed of particles, all having diameters equal to the mean particle diameter of the distribution reported in Fig. 5.3 (i.e. $\bar{\mathcal{D}} = 1.25$ mm). Fig. 5.12 shows the streamwise velocity profile (i.e. the x component of the velocity vector as a function of the z coordinate) of the mono-sized bed of grains at steady state in the two cases. The velocity profiles agree, with an R-squared value of 0.994. Thus the shear rate profile, which induces segregation, must be similar, and the two granular flows comparable.

Fig. 5.13 reports the evolution of quadrature weights (first column) and weighted

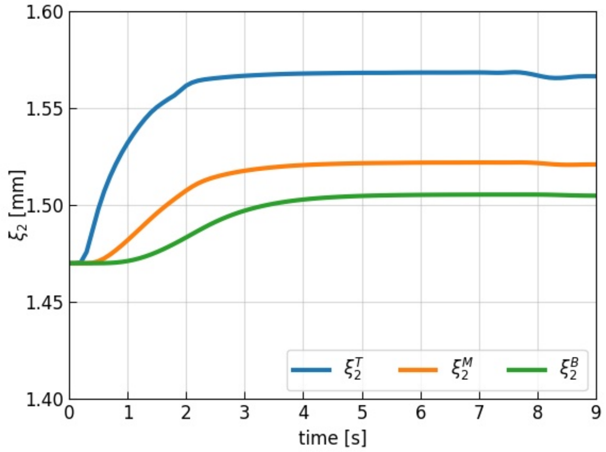

Figure 5.9: Evolution of the second quadrature node in the bottom, middle and top layer obtained by solving the CFD-PBE coupled model.

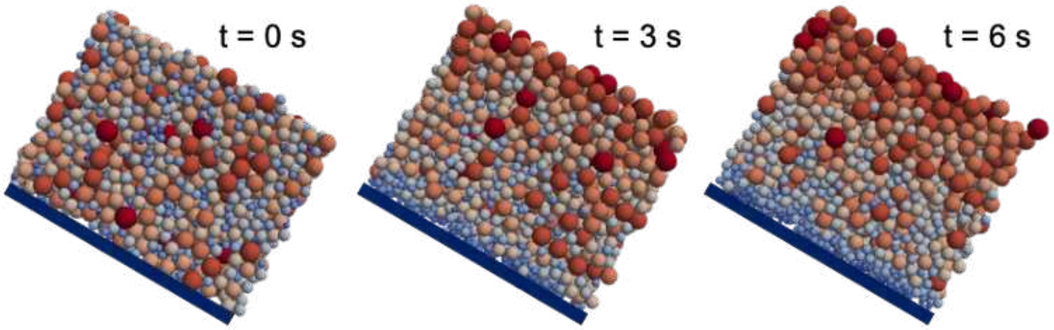

Figure 5.10: Snapshots from the DEM simulation. The system is filled with 3000 particles characterized by the volume density PSD reported in Fig. 5.3. The colours denote the particle diameter. At $t = 0$ s, the sample is well mixed. At time $t = 6$ s, the system has reached steady-state and the segregation profile has fully developed.

nodes (second column) obtained from both our CFD-PBE coupled model (coloured lines) and DEM simulations (black lines). The results refer to the top, middle and bottom layers and show that segregation is less pronounced on top, where the shear rate is smaller, and increases as the bottom wall is approached. The CFD-PBE coupled model predicts well the evolution of both weights and weighted nodes in the middle and top layers, but not in the bottom layer. This disagreement will be discussed in the following section.

Figs. 5.14, 5.15 and 5.16 report the PSDs and their two-node quadrature representations achieved after 6 s in the bottom, middle and top layers, respectively. The vertical lines, whose positions and heights are the quadrature nodes and quadrature weights, represent the Dirac delta functions of the quadrature formulas. As we can see, the results of the CFD-PBE and DEM simulations agree very well in the middle layer, and quite well in the top layer. However, the results differ in the bottom layer. There, the positions

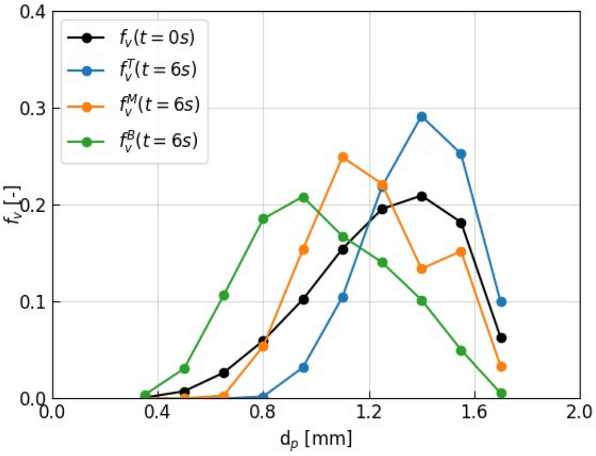

Figure 5.11: Particle size distribution at $t = 0$ s (black line), and after 6 s (coloured lines) in the three layers from DEM simulations.

indicate the quadrature nodes are over-estimated. Moreover, if the weight of the first node is overestimated, the weight of the second node is underestimated.

Thus, despite our CFD-PBE coupled model works for a range of conditions, it fails under some circumstances. The limitations of our model are not directly related to the CFD-PBE framework but rather to the assumptions we made of: constant and isotropic diffusion, constant drag coefficient, and uniform and constant bed porosity.

5.5.4 Discussion

In this section, we justify the observed discrepancies on theoretical grounds by examining the assumptions we employed in the CFD-PBE model regarding diffusion, drag coefficient and bed porosity.

In granular flows, diffusion has mainly been studied for monodisperse particle systems. According to Utter and Behringer [34], who studied the random motion of monodisperse grains in a two-dimensional Couette shearing experiment, the self-diffusivity is proportional to the local shear rate and the square of the particle radius (i.e. $\mathcal{D} \propto \dot{\gamma} d^2$). In chute flows of bidisperse disks, Berton et al. [35] observed that the diffusive process is independent of the particle size and that the diffusion coefficient associated with each layer increases linearly with the layer height. Since the shear rate decreases when the height increases, being maximum at the wall, it follows that $\mathcal{D}$ should not depend on the particle size and should decrease with the shear rate. This disagrees with what Utter and Behringer [34] reported. More recently, Chassagne et al. [36] showed that the diffusion coefficient should depend on the inertial number.

The articles just cited reveal that the process of particle diffusion in dense monodisperse granular media is still unclear and reliable constitutive equations are unavailable. For dense polydisperse granular media, this is all the more true [36]. This is why we decided

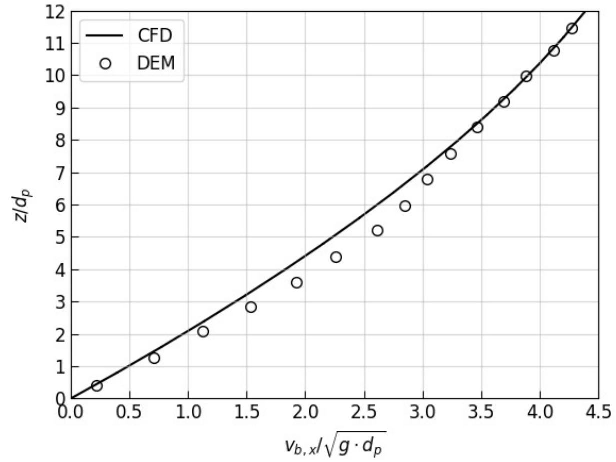

Figure 5.12: Comparison of the dimensionless streamwise velocity profile as a function of z/d_p obtained with DEM and CFD simulations.

to model the process as isotropic using a constant coefficient of diffusion. To better address the problem of inhomogeneous diffusion coefficients, one could carry out simulations based on a classical random walk [35].

In this work, we further assumed a linear drag law with constant drag coefficient c, even though c is expected to be a function of the Reynolds number (Re), Froude number (Fr), particle concentration, particle size, restitution coefficient and flow depth [37, 38]. The absence of constitutive equations accounting for these dependencies [19] justifies our modelling choice.

Finally, even if it is well-known that the packing porosity varies with the size distribution of the materials involved [39], we neglected this effect. Accounting for variations in the local porosity would require a more expensive multiphase model than the coupled level-set and volume of fluid (VOF) method.

To prove that the inconsistency of the results is due to the assumptions we made and not to the CFD-PBE coupling framework, we have reported in Fig. 5.17 the evolution of weights and weighted nodes obtained at the bottom layer for different values of the parameters $\mathcal{D}$ and a constant value of the drag coefficient (i.e. $c = 6{\cdot}10^4$ s^{-1}). As expected, the higher the diffusion coefficient, the lower the degree of segregation. Analogously, Fig. 5.18 reports the evolution of weights and weighted nodes obtained at the bottom layer for different values of the drag coefficient and same diffusion (i.e. $\mathcal{D} = 1.2 \cdot 10^{-5}$m^{2}s^{-1}). At increasing values of the drag coefficient, the segregation process becomes slower and less pronounced. Thus, to quantitatively change the results in the bottom layer, one should at least define drag and diffusion coefficients as functions of the bed depth.

All these considerations suggest that the main features of the CFD-PBE model are correct; the evolution of weights and weighted nodes is well predicted for a high portion of the flow depth. Nevertheless, to improve the accuracy of the model, in particular in the

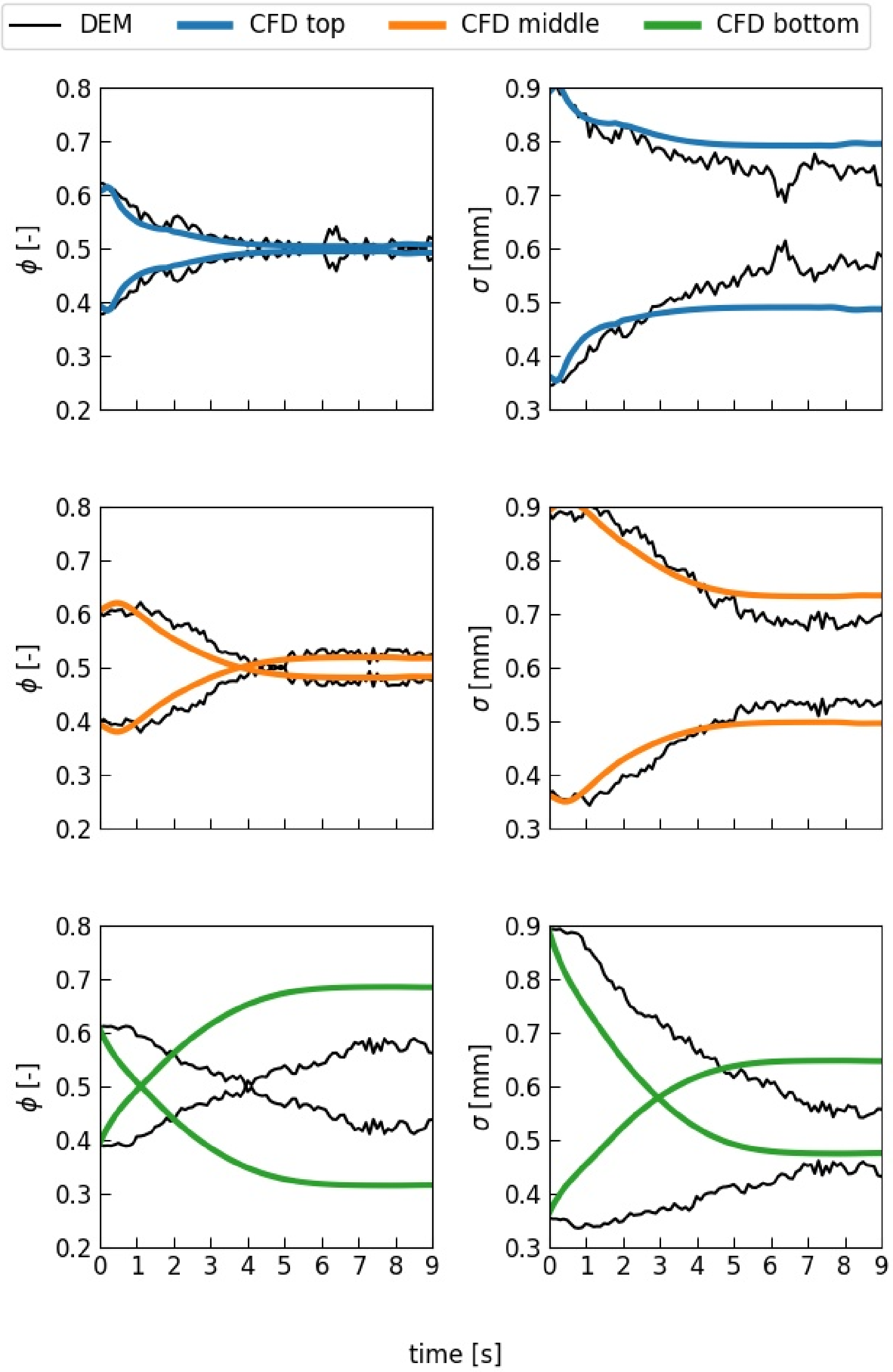

Figure 5.13: Evolution of the quadrature weights (on the left) and weighted nodes (on the right) obtained from the segregation CFD-PBE coupled model (coloured lines) and the DEM simulation (black line). The results refer to the top, middle and bottom layers.

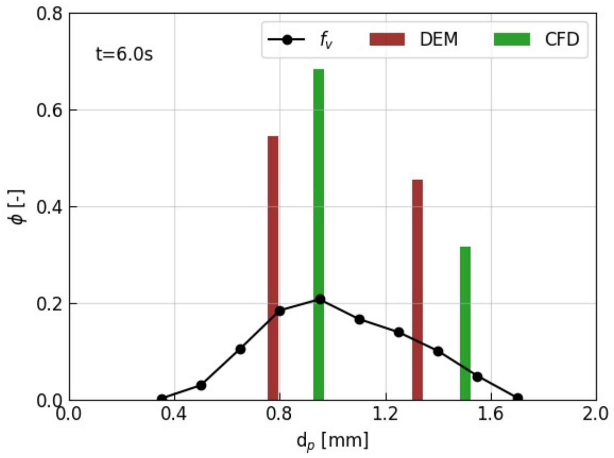

Figure 5.14: PSD at the bottom of the chute after $t = 6$ s. The red lines represent the two-node representation obtained from the DEM simulation, while the green lines are the two-node representation obtained from the CFD simulation.

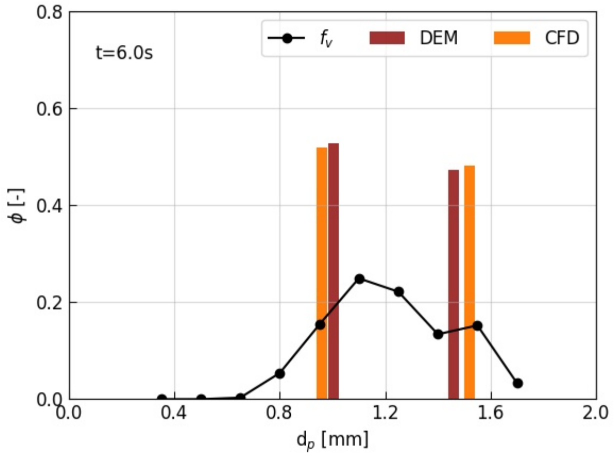

Figure 5.15: PSD in the middle layer at $t = 6$ s. The red lines represent the two-node representation obtained from the DEM simulation, while the orange lines are the two-node representation obtained from the CFD simulation.

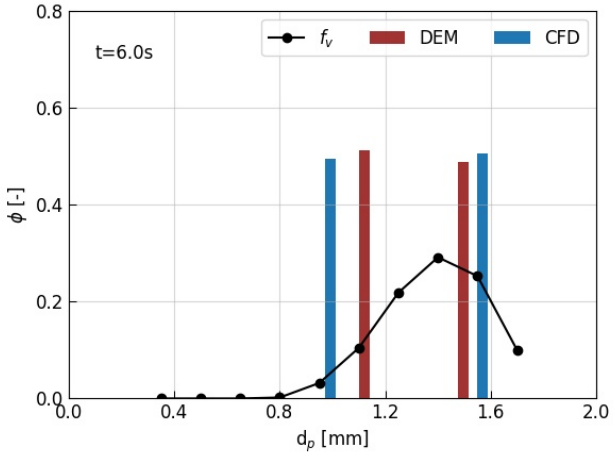

Figure 5.16: PSD in the top layer at $t = 6$ s. The red lines represent the two-node representation obtained from the DEM simulation, while the blue lines are the two-node representation obtained from the CFD simulation.

region close to the wall, we must describe the gravity-induced segregation process and the shear-induced diffusion process more accurately. This requires more physical insight into these processes and more reliable constitutive equations.

5.6 Conclusions

In this chapter, we presented a new CFD-PBE coupled model for describing segregation in dense polydisperse granular flows. The PBE was solved with the direct quadrature method of moments proposed by Marchisio and Fox [12]. We adopted a two-node quadrature approximation of the particle size distribution and used a segregation-remixing model to close the size-conditioned particle velocity. The $2n$ resulting transport equations were then implemented in Ansys fluent. To track the interface between the granular medium and air, we used the coupled level-set and VOF method. To determine the velocity field in the granular mixture, we employed the rheological model of Jop et al. [25]. To test the model, we modelled segregation in a granular mixture with an arbitrary polydisperse grain size distribution flowing down an inclined plane and we compared the results to those of DEM simulations. This geometry was chosen for its importance and simplicity but our results should be broadly applicable to other dense granular flows.

We found that, the CFD-PBE coupled model predicts reasonably well the segregation process. It has a considerable benefit and, unlike DEM, allows simulating large polydisperse powder systems with reasonable computational cost. This is a relevant step forward for the scale-up and design of all those industrial applications that employ granular materials in large quantities as it happens, for instance, in agriculture, chemical engineering industries and mining.

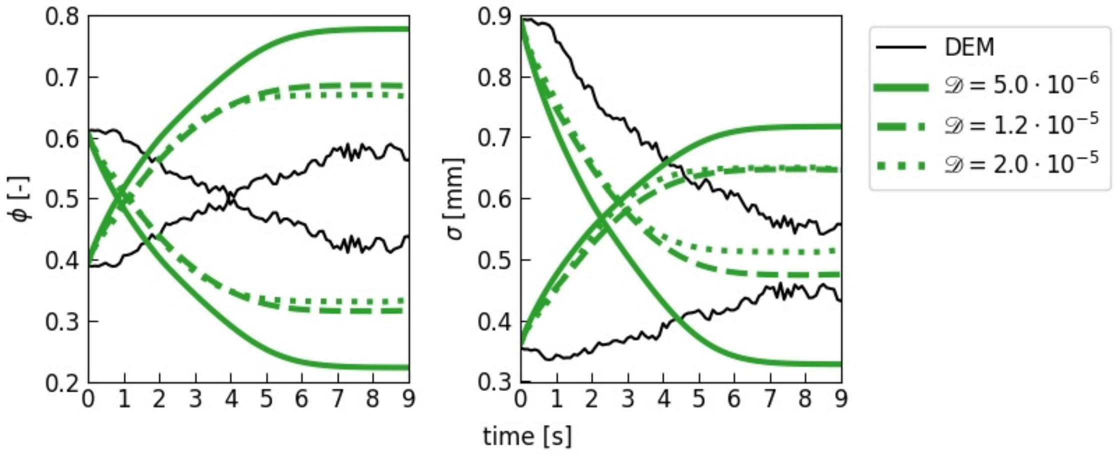

Figure 5.17: Evolution of weights (on the left) and weighted nodes (on the right) in the bottom layer obtained with constant drag ($c = 6 \cdot 10^4 \mathrm{s}^{-1}$) and different values of the parameters $\mathcal{D}$ using the CFD-PBE coupled model. The solid black lines represent the DEM results and are reported for comparison.

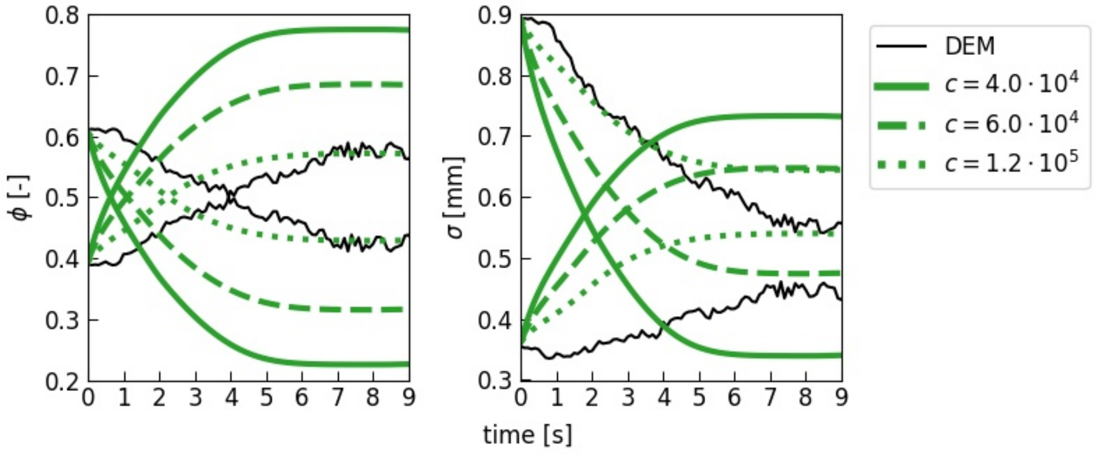

Figure 5.18: Evolution of weights (on the left) and weighted nodes (on the right) in the bottom layer obtained with different values of the drag coefficient and same diffusivity ($\mathcal{D} = 10^{-5} \mathrm{m}^2 \mathrm{s}^{-1}$) using the CFD-PBE coupled model. The solid black lines represent the DEM results and are reported for comparison.

Despite its advantages, the model has a few drawbacks. The employed segregation-remixing model relies on a drag coefficient and a diffusion coefficient that we set as constants. This is because, even though there are a lot of studies, results are often controversial, and many fundamental questions still remain to be answered. Further research is needed to gain a better understanding of the effect of diffusivity and drag coefficient.

Bibliography

[1] L. Mazzei. Segregation dynamics of dense polydisperse fluidized suspensions modeled using a novel formulation of the direct quadrature method of moments. *Chemical Engineering Science*, 101:565–576, 2013.

[2] J. M. N. T. Gray. Particle Segregation in Dense Granular Flows. *Annu. Rev. Fluid Mech*, 50(1):407–33, 2018.

[3] H. Arastoopour, D. Gidaspow, and E. Abbasi. *Computational Transport Phenomena of Fluid-Particle Systems*. Springer, 2017.

[4] D. Ramkrishna. *Population Balances: Theory and Applications to Particulate Systems in Engineering*. Elsevier, 2000.

[5] D. L Marchisio and R. O. Fox. *Multiphase reacting flows: modelling and simulation*. Springer, 2007.

[6] L. Mazzei. Limitations of quadrature-based moment methods for modeling inhomogeneous polydisperse fluidized powders. *Chemical Engineering Science*, 66(16): 3628–3640, 2011.

[7] R. McGraw. Description of aerosol dynamics by the quadrature method of moments. *Aerosol Science and Technology*, 27(2):255–265, 1997.

[8] D. L. Marchisio, J. T. Pikturna, R. O. Fox, R. D. Vigil, and A. A. Barresi. Quadrature method of moments for population-balance equations. *AIChE Journal*, 49(5):1266–1276, 2003.

[9] D. L. Marchisio, R. D. Vigil, and R. O. Fox. Quadrature method of moments for aggregation-breakage processes. *Journal of Colloid and Interface Science*, 258(2): 322–334, 2003.

[10] M. Strumendo and H. Arastoopour. Solution of PBE by MOM in finite size domains. *Chemical Engineering Science*, 63(10):2624–2640, 2008.

[11] L. Mazzei, D. L. Marchisio, and P. Lettieri. New Quadrature-Based Moment Method for the Mixing of Inert Polydisperse Fluidized Powders in Commercial CFD Codes. *AIChE Journal*, 58(10):3054–3069, 2012.

[12] D. L. Marchisio and R. O. Fox. Solution of population balance equations using the direct quadrature method of moments. *Journal of Aerosol Science*, 36(1):43–73, 2005.

[13] L. Mazzei, D. L. Marchisio, and P. Lettieri. Direct quadrature method of moments for the mixing of inert polydisperse fluidized powders and the role of numerical diffusion. *Industrial and Engineering Chemistry Research*, 49(11):5141–5152, 2010.

[14] D. L. Marchisio and R. O. Fox. *Computational models for polydisperse particulate and multiphase systems*. Cambridge University Press, 2013.

[15] L. Mazzei. *Eulerian modelling and computational fluid dynamics simulation of mono and polydisperse fluidized suspension*. PhD thesis, UCL (University College London), 2008.

[16] J. Bridgwater. Fundamental powder mixing mechanisms. *Powder Technology*, 15(2): 215–236, 1976.

[17] S. B. Savage and C. K. K. Lun. Particle size segregation in inclined chute flow of dry cohesionless granular solids. *Journal of Fluid Mechanics*, 189:311–335, 1988.

[18] J. M. N. T. Gray and V. A. Chugunov. Particle-size segregation and diffusive remixing in shallow granular avalanches. *Journal of Fluid Mechanics*, 569:365–398, 2006.

[19] B. Marks, P. G. Rognon, and I. Einav. Grainsize dynamics of polydisperse granular segregation down inclined planes. *Journal of Fluid Mechanics*, 690:499–511, 2012.

[20] D. R. Tunuguntla, O. Bokhove, and A. R. Thornton. A mixture theory for size and density segregation in shallow granular free-surface flows. *Journal of Fluid Mechanics*, 749:99–112, 2014.

[21] J. M.N.T. Gray and A. R. Thornton. A theory for particle size segregation in shallow granular free-surface flows. *Proceedings of the Royal Society A: Mathematical, Physical and Engineering Sciences*, 461(2057):1447–1473, 2005.

[22] E. Olsson, G. Kreiss, and S. Zahedi. A conservative level set method for two phase flow II. *Journal of Computational Physics*, 225(1):785–807, 2007.

[23] M. Dianat, M. Skarysz, and A. Garmory. A Coupled Level Set and Volume of Fluid method for automotive exterior water management applications. *International Journal of Multiphase Flow*, 91:19–38, 2017.

[24] G. D. R. MiDi. On dense granular flows. *European Physical Journal E*, 14(4):341–365, 2004.

[25] P. Jop, Y. Forterre, and O. Pouliquen. A constitutive law for dense granular flows. *Nature*, 441:727–730, 2006.

[26] D. Hirshfeld and D. C. Rapaport. Molecular dynamics studies of grain segregation in sheared flow. *Physical Review E*, 56(2):2012–2018, 1997.

[27] L. E. Silbert, J. W. Landry, and G. S. Grest. Granular flow down a rough inclined plane: Transition between thin and thick piles. *Physics of Fluids*, 15(1):1–10, 2003.

[28] T. Weinhart, S. Luding, and A. R. Thornton. From discrete particles to continuum fields in mixtures. *AIP Conference Proceedings*, 1542(1):1202–1205, 2013.

[29] P. C. Johnson and R. Jackson. Frictional-collisional constitutive relations for granular materials, with application to plane shearing. *Journal of Fluid Mechanics*, 176:67–93, 1987.

[30] R. D. Mindlin. Compliance of elastic bodies in contact. *Journal of Applied Mechanics*, 16:259–268, 1949.

[31] X. M. Zheng and J. M. Hill. Molecular dynamics modelling of granular chute flow: Density and velocity profiles. *Powder Technology*, 86(2):219–227, 1996.

[32] A. Jain, M. J. Metzger, and B. J. Glasser. Effect of particle size distribution on segregation in vibrated systems. *Powder Technology*, 237:543–553, 2013.

[33] R. G. Gordon. Error bounds in equilibrium statistical mechanics. *Journal of Mathematical Physics*, 9(5):655–663, 1968.

[34] B. Utter and R. P. Behringer. Self-diffusion in dense granular shear flows. *Physical Review E - Statistical, Nonlinear, and Soft Matter Physics*, 69:1–12, 2004.

[35] G. Berton, R. Delannay, P. Richard, N. Taberlet, and A. Valance. Two-dimensional inclined chute flows: Transverse motion and segregation. *Physical Review E*, 68(5): 51303, 2003.

[36] R. Chassagne, R. Maurin, J. Chauchat, J. M. N. T. Gray, and P. Frey. Discrete and continuum modelling of grain size segregation during bedload transport. *Journal of Fluid Mechanics*, 895, 2020.

[37] P. Gauer, D. Issler, K. Lied, K. Kristensen, H. Iwe, E. Lied, L. Rammer, and H. Schreiber. On full-scale avalanche measurements at the ryggfonn test site, norway. *Cold Regions Science and Technology*, 49(1):39–53, 2007.

[38] A. Panaitescu, X. Clotet, and A. Kudrolli. Drag law for an intruder in granular sediments. *Physical Review E*, 95(3):1–7, 2017.

[39] N. Ouchiyama and T. Tanaka. Porosity estimation from particle size distribution. *Industrial and Engineering Chemistry Fundamentals*, 25(1):125–129, 1986. ISSN 01964313.

Chapter 6

Density-driven segregation

Among the different particle properties that can drive segregation, there is particle density. Unlike the previous chapters, this one focuses on density-driven segregation in dense bidisperse mixtures of particles under non-uniform shear rates.

This work was done with the help and assistance of Dr Riccardo Artoni and Dr Patrick Richard from the Gustave Eiffel University, in France. The experiments were carried out in the Aggregates and Materials Processing Laboratory (GPEM) of IFSTTAR, site of Nantes.

Parts of this chapter have been published:

M. Tirapelle, A. C. Santomaso, P. Richard, and R. Artoni (2021a). Experimental investigation and numerical modelling of density-driven segregation in an annular shear cell. *Advanced Powder Technology*, 32, 1305–1317, https://doi.org/10.1016/j.apt.2021.02.020.

M. Tirapelle, A. C. Santomaso, P. Richard, and R. Artoni (2021b). Shear-driven density segregation: an experimental study. In *EPJ Web of Conferences*, 249, 03021. EDP Sciences, https://doi.org/10.1051/epjconf/202124903021.

6.1 Introduction

Granular materials composed of particles with different sizes, densities, shapes, or surface properties may experience unexpected segregation when subjected to process vibration or shear [1]. Even though particle size is known to be the most relevant factor determining segregation, the effect of large density differences may also be of importance for some industries. Because of density-driven segregation, lighter particles are likely to rise, heavier particles sink, and the mixture un-mixes [2].

Several studies have been conducted with a view to understanding density-driven segregation in dense granular flows using both experiments [3–9] and the Discrete Element Method simulations [10–14]. Furthermore, numerous theoretical models have been reported in the literature [9, 11, 12, 14, 15]. In developing such models, two different approaches have been used. The first one, which is based on the Kinetic Theory of Granular Flow (KTGF), predicts well segregation in the case of low or moderate solid fractions, however, it breaks down quantitatively in the case of densely packed flows [13]. The second type of models, which are based on a hydrodynamic balance of forces (i.e. drag and buoyancy), can successfully reproduce gravity-driven segregation although they are phenomenologically based [2, 11]. Density-driven segregation has been studied in a variety of systems, among which there are fluidized beds [16, 17], vertically vibrated cylinders [18], rotating cylinders [8, 19, 20], inclined chutes [10, 12, 15], split-bottom cells [7] and shear cells [21–24].

In this chapter, we experimentally investigate density-difference-driven segregation for a range of density ratios and a range of mixture composition. The experiments are conducted in an annular shear cell with rotating bumpy bottom that yields an exponential shear profile. The cell is similar to that used in Savage and Sayed [21] and Wildman et al. [22]; furthermore, it has been used by May et al. [23] to study shear-driven size segregation and by Artoni et al. [24] to assess stresses, shear localization and wall friction of confined dense granular flows. We have chosen this geometry because of its numerous advantages. It determines a continuous granular flow with well-defined initial and final states. Moreover, the velocity profile that develops within the powder bed decays exponentially with depth (from the rotating shearing bottom to the top lid) determining a non-uniform shear rate. To the author's knowledge, nobody has studied density-driven segregation in this type of system before.

Here, we also develop a continuum model for describing density-driven segregation of dense granular flows that is based on a balance of forces. We use a segregation-diffusion transport equation, constitutive relations for the closure of effective viscosity and friction coefficient, and a segregation velocity analogous to Stokes' law. The model, which is validated against experimental findings, can successfully predict density-driven segregation at different density ratios and component volumetric fractions, provided that, the degree of exponential decay appearing in the velocity profile is correctly estimated. We have also found that density segregation is very sensitive to the shear localization features and that, at low load, a transverse friction coefficient may induce a three-dimensional flow pattern.

6.2 Experimental campaign

The experiments were designed to investigate density-driven segregation in binary mixtures of equal-sized particles with different densities, for a range of density ratios, δ_R, and initial mixture compositions. In this section, we provide detailed information about experimental set-up, employed materials and measurement methods.

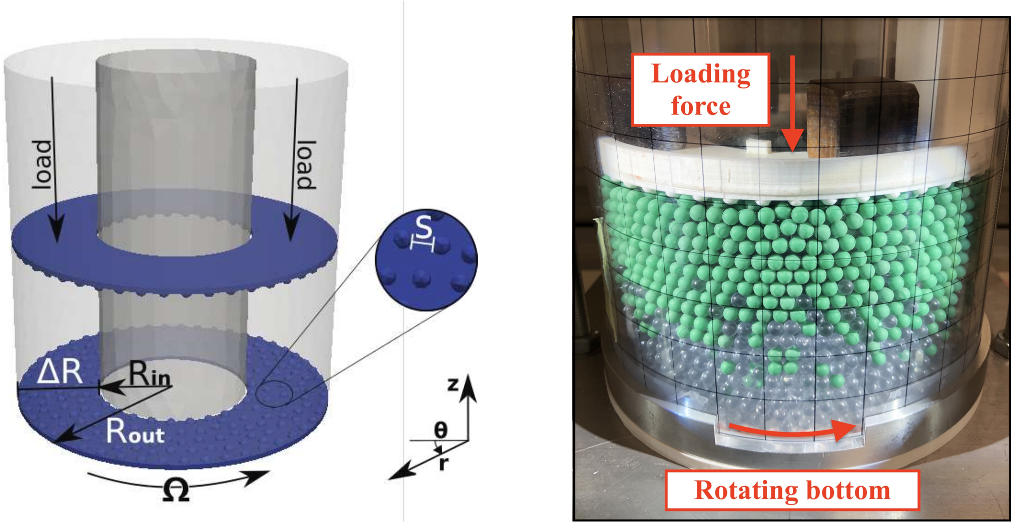

Figure 6.1: (On the left) Sketch of the annular shear cell and the coordinate system. Particles are filled in the annular region with a thickness equal to ΔR in between the two horizontal bumpy walls. The bottom wall rotates at a rotational speed Ω; whereas on the top lid, an additional load is applied. (On the right) Photograph of the experimental setup filled with a 50:50 mix of grains by volume.

6.2.1 Experimental set-up and operative conditions

The experiments are performed in an annular shear cell with a rotating bottom and an overloaded top wall. The cell is made of two coaxial poly-methyl methacrylate (PMMA) cylinders. The smallest cylinder has outer diameter equal to 90 mm, whereas the largest cylinder has inner diameter equal to 190 mm. The annular region is therefore 50 mm thick. The top and bottom walls are 3D printed in poly-lactic acid (PLA). To increase the friction between walls and grains and to reduce sliding, the walls were designed with hemispheres of diameter 6 mm placed on a continuous random triangulation with a mean distance of 12 mm between their edges. The bottom wall is fixed on a rotating plate that rotates at a constant rotational speed of $\Omega = 23.44$ rpm. The top wall is free to move vertically, but cannot rotate. On top, a load of $M_w = 1.093$ kg provides confinement. A sketch of the experimental apparatus is reported in Fig. 6.1.

The experiments are conducted with binary mixtures of same-sized spherical particles of diameter $d_p \approx 6$ mm and different densities. We employed particles made of Stainless Steel, Ceramic, Glass, filled Polyoxymethylene and Polypropylene (see Fig. 6.2). At the beginning of each experiment, the cell is filled with a layer of light particles crowned by an upper layer of more massive particles, for a total bed height of $H = 90$ mm, namely 15 particle diameters (see Fig 6.1-on the right).

Table 6.1 shows all the combinations of density ratio and heavy particle volumetric fraction, $\phi_{h,0}$, for which segregation has been evaluated. For each test, the amount of grains filled in the cell, M_g, is reported in kg.

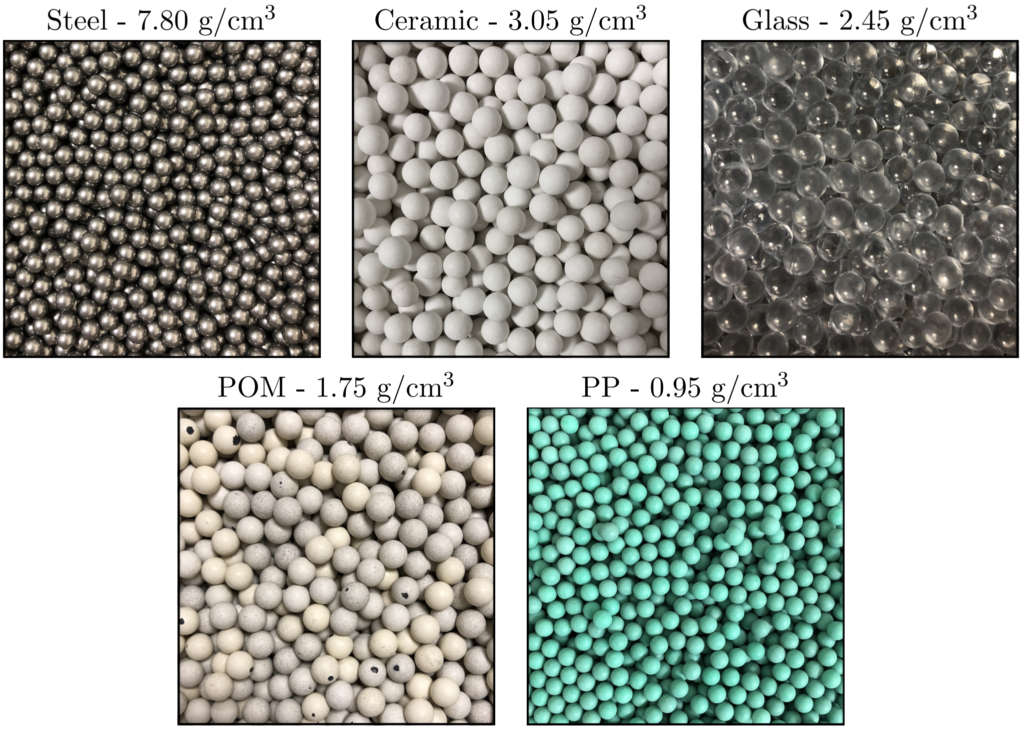

Figure 6.2: Photographs of the materials and their corresponding densities. In order: Steel, Ceramic, Glass, filled Polyoxymethylene and Polypropylene. Their particle diameters are: 6.0 ± 0.025 mm for steel, 6.0 ± 1.0 mm for ceramic (however we measured $d_{10} = 5.6$ mm and $d_{90} = 6.3$ mm), 6.0 ± 0.3 mm for glass, 5.9 ± 0.1 mm for filled Polyoxymethylene and 6.0 ± 0.05 mm for Polypropylene.

				M_g [kg]				
ID	Heavy p.	Light p.	δ_R	10%	25%	50%	75%	90%
S-PP	Steel	Polypropylene	8.25	—	—	5.25	7.30	8.54
S-POM	Steel	Filled POM	4.46	2.83	3.92	5.73	7.55	8.64
C-PP	Ceramic	Polypropylene	3.70	—	—	2.67	3.43	3.89
G-PP	Glass	Polypropylene	2.59	—	—	2.04	2.49	2.76
POM-PP	Filled POM	Polypropylene	1.85	—	—	1.62	—	—
G-POM	Glass	Filled POM	1.40	—	—	2.52	—	—

Table 6.1: Details of the experimental conditions. The columns report, from left to right, the combination ID, the heavy component, the light component, their density ratio δ_R and $\phi_{h,0}$. For the tested combinations, the total mass of grains M_g filled in the cell is reported in kg.

6.2.2 Post-processing image analysis

The segregation process is filmed through the transparent side-wall by a commercial camera (a GoPro Hero 4 black) running at 0.5 or 1.5 fps. In the case of $\delta_R = 1.40$, 1.85 and 2.59, indeed, the segregation process is such slow that 0.5 fps is small enough to capture the main features of segregation. At the two sides of the camera, two homogeneous light-emitting diodes (LED) light the system. Once taken, the images are transferred from the camera to the computer and subjected to post-processing image analysis.

The procedure for the post-processing image analysis consists of un-distorting, cropping and converting from the RGB colour space to Grey each frame. The particles are detected thanks to the HoughCircles tool [25], which gives as output the diameters of the particles and the coordinates of their centres. To discern heavy and light particles, the cropped RGB images are also converted in the HSV or LAB colour-space and subjected to threshold segmentation. These images are used as masks for discriminating between different material types. An example of a processed frame is shown in Fig. 6.3. On the left, we can see the frame after being undistorted. On the right, we can see the detected particles, differentiated by type (i.e. Steel and Polypropylene).

Once the type and position of each particle in each frame is determined, the temporal evolution of the heavy particle concentration through the depth of the cell is reconstructed. The investigation window spans the entire height of the particle bed ($H = 15d_p$) and is $9d_p$ wide (i.e. small enough to reduce the effect of the wall curvature). This window is subdivided into 15 discrete horizontal layers, each one being one particle diameter high. The concentration of the heavy component in a given layer is calculated as the number fraction of heavy particles having their centre within that layer. To reduce the noise in the concentration profiles, the moving average technique is applied over time.

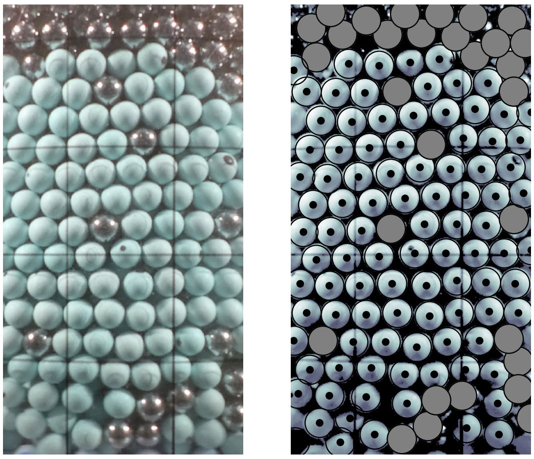

Figure 6.3: On the left: an example of a cropped and undistorted picture. On the right: the draw of the detected particles distinguished for density.

6.3 Density-driven segregation model

In this section, we propose a new continuum model for describing the density-driven segregation of dense granular flows. The model, which is based on a balance of forces, is similar to the segregation model previously proposed by Tripathi and Khakhar [11], however, our formulation is characterized by a significant reduction in complexity: we introduce neither the effective temperature nor a coupling with a rheological model for describing the flow field.

6.3.1 Segregation velocity

Let us consider a heavy particle having diameter d_p and intrinsic density ρ_h^* in a medium composed of lighter particles with the same diameter and intrinsic density ρ_l^*. At steady-state, the force of gravity is balanced by a buoyancy force and a viscous drag force:

$$\boldsymbol{F_g} = \boldsymbol{F_b} + \boldsymbol{F_d} \, . \tag{6.1}$$

If we model each term of the above formulation, we obtain:

$$\frac{\pi}{6} d_p^3 \rho_h^* \boldsymbol{g} = \frac{\pi}{6} d_p^3 \bar{\rho} \boldsymbol{g} + 6\pi\eta \frac{d_p}{2} w_h \, , \tag{6.2}$$

where $\boldsymbol{g} = 9.81$ m/s^2 is the gravitational acceleration that acts in the direction of fall, $\bar{\rho}$ is the averaged intrinsic density of the solid mixture and w_h is the falling (or segregation) velocity. For a binary mixture of different density particles, and considering constant overall solid volume fraction, $\bar{\rho}$ is obtained by weighting the intrinsic density of each component by the corresponding volumetric fraction (see Eq. 2.52):

$$\bar{\rho} = \rho_h^* \phi_h + \rho_l^* \phi_l \, . \tag{6.3}$$

Thus, solving Eq. 6.2 for the falling velocity of the heavy particle yields:

$$w_h = \frac{d_p^2 \boldsymbol{g}}{18\eta} \left[(1 - \phi_h) \left(\rho_h^* - \rho_l^* \right) \right] \, . \tag{6.4}$$

It is worthwhile to highlight that this velocity is analogous to the terminal velocity of a sphere that falls under gravity in a viscous medium as predicted by Stokes' law [26]. After manipulation, we obtain the following segregation velocities for the heavy and light components when subjected to shear in a dense bi-dispersed granular flow:

$$w_h = k \frac{d_p^2 \boldsymbol{g}}{18\eta} \left[\rho_h^* \left(1 - \phi_h\right) \left(1 - \frac{1}{\delta_R}\right) \right] \, , \tag{6.5}$$

$$w_l = k \frac{d_p^2 \boldsymbol{g}}{18\eta} \left[\rho_l^* \left(1 - \phi_l\right) \left(1 - \delta_R\right) \right] \, . \tag{6.6}$$

These formulas reveal that the higher the density difference, the higher the driving force leading to segregation. Moreover, segregation is faster when a particle is surrounded by a larger amount of grains of the other component. The proportionality parameter k accounts for the fact that in a binary mixture of grains, particles are not diluted. Furthermore, different frictional properties may influence the particle flow behaviour. To model segregation, those segregation velocities should be implemented within advection-diffusion segregation equations.

6.3.2 Segregation equation

For describing the changes in the local constituent concentration due to segregation, each species has to satisfy a transport equation (see Eq. 2.57). In an annular shear cell, segregation is significant only along the direction of gravity thus, the advection-diffusion segregation equation becomes:

$$\frac{\partial \phi_i}{\partial t} + \frac{\partial}{\partial x} u\phi_i + \frac{\partial}{\partial y} v\phi_i + \frac{\partial}{\partial z} w\phi_i = -\frac{\partial w_i \phi_i}{\partial z} + \frac{\partial}{\partial z}\left(\mathcal{D}\frac{\partial \phi_i}{\partial z}\right) , \tag{6.7}$$

where the subscript i can be h or l for heavy and light components, respectively, w_i is the segregation velocity (i.e. Eqs. 6.5 and 6.6), $\mathcal{D}$ is the diffusion coefficient and the velocity $\boldsymbol{v} = (u, v, w)$ is the velocity of the bulk solid. Since in an annular shear cell, the flow is basically unidirectional in the azimuthal direction θ and varies only in the vertical z-direction, the bulk velocity reads $\boldsymbol{v} = (0, v(z), 0)$ and Eq. 6.7 reduces to a 1D transport equation for the volume concentration:

$$\frac{\partial \phi_i}{\partial t} = -\frac{\partial w_i \phi_i}{\partial z} + \frac{\partial}{\partial z}\left(\mathcal{D}\frac{\partial \phi_i}{\partial z}\right) . \tag{6.8}$$

The diffusion coefficient in Eq. 6.8 accounts for the random particle motion. It is due to random particle collisions and it depends on local shear rate and particle diameter [11, 27]. The dependence of $\mathcal{D}$ on the overburden pressure is negligible in the case of both size and density bi-dispersed flow [28]. Thus, we express $\mathcal{D}$ as [27]:

$$\mathcal{D} = b\dot{\gamma}{d_p}^2 , \tag{6.9}$$

where b is a constant that is usually assumed to be equal to 0.041 [27]. To characterize the shear rate $\dot{\gamma}$, the velocity field must be known. Instead of solving the momentum equation (the inclusion of density differences within the momentum equation would have implied that the velocity field is compressible and would have led to more complex models), the velocity field is determined directly from analytic solutions.

In an annular shear cell, the velocity profile of the particles in a monodisperse material decays exponentially with the bed height so that it is well described by an exponential profile of the type [23, 24]:

$$v(z) = v_1 + (v_0 - v_1)\exp\left(-\frac{z}{\delta}\right), \tag{6.10}$$

where v is the particles horizontal velocity, v_0 and v_1 are the velocities of the bottom wall and the slip velocity at the top wall, respectively; and δ is the coefficient of the exponential decay that depends linearly on particle size [24]. Since there is no information in the literature, we assume that the velocity has the same profile also in the case of density bidisperse mixtures. Owing to the non-uniformity of the velocity gradient, the shear stress is not constant throughout the domain. To obtain the shear rate, the velocity profile is differentiated as:

$$\dot{\gamma}(z) = \frac{dv}{dz} = \frac{d}{dz}\left[v_1 + (v_0 - v_1)\exp\left(-\frac{z}{\delta}\right)\right]. \tag{6.11}$$

Since the velocity profile is approximately time-independent, except for an initial transient [23], we considered the shear rate profile time-invariant.

6.3.3 Constitutive relations

In its definition, the segregation velocity contains the effective solid viscosity, η. To close the effective viscosity, we have implemented the law proposed by Jop et al. [29] that reads:

$$\eta(|\dot{\gamma}|, p) = \frac{\mu(I)p}{|\dot{\gamma}|}, \tag{6.12}$$

where μ is the friction coefficient and p is the local pressure [29]. This relation holds true in the intermediate dense regime of flow, that is the regime observed in our experiments. The closure of $\mu(I)$ is achieved by implementing the original $\mu(I)-$rheology proposed by the Groupement De Recherche Milieux Divisès [30] with $\mu_{min} = \tan(20.90^o)$, $\mu_2 = \tan(32.76^o)$ and $I_0 = 0.36$. As discussed in Section 2.2.2.2, the $\mu(I)-$rheology states that the friction coefficient is rate-dependent and scales with the inertial number I [29, 30]. For density bidisperse granular materials, we have proposed a new expression for I as a function of the local averaged density of the solid mixture:

$$I = |\dot{\gamma}| d_p \sqrt{\frac{\bar{\rho}}{p}}. \tag{6.13}$$

The pressure, which appears in both Eq. 6.12 and Eq. 6.13, evolves in time and varies with depth according to:

$$p(z,t) = p_{load} + g\int_h^H \rho_b(z,t)dz, \tag{6.14}$$

where p_{load} is the pressure load due to the loading force applied on the top wall and $\rho_b(z,t)$ is the bulk density. The bulk density reads:

$$\rho_b(z,t) = \bar{\rho}(z,t)\nu\,. \tag{6.15}$$

The overall solid volume fraction, namely ν, is assumed constant and set equal to 0.6. The assumption of being constant is reasonable since the bed is confined by an overload. Furthermore, unlike size segregation, the local porosity does not change accordingly to the local concentration of each species (i.e. all particles have the same diameter). Note that, the value $\nu = 0.6$ comes from experimental evidence.

6.3.4 Initial and boundary conditions

The continuum model is implemented in a finite element commercial code (COMSOL multiphysics) to predict segregation driven by density in binary mixtures of particles, for the same density ratios and initial particle concentrations that have been investigated experimentally. The initial condition corresponds to the initial experimental configuration, so the heavy particle concentration in space, at time $t = 0$, is represented with the following step function:

$$\phi_h(z,0) = \begin{cases} 0 & 0 \leq z \leq \bar{z} \\ 1 & \bar{z} \leq z \leq H\,. \end{cases} \tag{6.16}$$

The location of the interface between light and heavy components, $\bar{z}$, depends on the initial mixture composition. Across $\bar{z}$, the concentration jump has been smoothed with a second-order continuous smoothing function. This guarantees the continuity of the first and second-order derivatives and hence, avoids discontinuous solutions. Then, to ensure that particles do not get through the upper and lower boundaries, we have imposed the no-flux boundary condition at the top and bottom walls:

$$\mathcal{D}\frac{\partial \phi_i}{\partial z} - w_i = 0\,. \tag{6.17}$$

6.4 Results and discussion

This section deals with experimental results, model validation and discussion. As concerns the experiments, only one repetition for each tested condition is presented even if preliminary experiments have been performed to check the test repeatability. To validate the model, the numerical results are compared against the experimental findings.

6.4.1 Experimental results

As a first macroscopic assessment of the evolution of segregation, we analyse the concentration profiles of the heavy component in the lower layer of the investigation window.

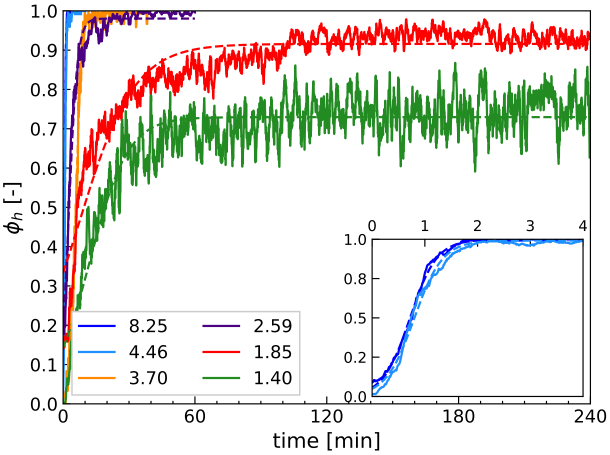

Figure 6.4: Evolution of the concentration profiles of the heavy grains at the bottom. The profiles are shown for different density ratios δ_R. In all cases, the experiments were started by filling the bottom half of the cell with the lighter material, and the top half of the cell with the denser material (50% initial overall concentration). In the inset, the 8.25 and 4.46 density ratio curves are represented on a larger scale. Note that all solid lines represent the experimental results, whereas the dashed lines are fitted with Eq. 6.18.

The assessment is done for six different density ratios and 50:50 mixture composition of the heavy and light components. The resulting profiles are displayed in Fig. 6.4. When the granular material flows, all particles start diffusing and segregating: heavy grains percolate downward, whereas light particles rise through the bed driven by the buoyant force. The heavy particle concentration grows from 0, passes through 50% concentration, and then reaches the steady-state. Such a system has moved from the initially segregated configuration to a well-mixed state until re-segregating again. The driving force leading to segregation is higher in the case of higher density ratios and dominates over diffusion. For smaller density ratios, diffusion gains always more importance over segregation. For this reason, the lower the δ_R, the lower the final ϕ_h reached (e.g. ϕ_h settles at around 73% for $\delta_R = 1.40$ and at 100% for $\delta_R = 8.25$).

In order to extract some parameters describing the process dynamics, the experimental profiles are fitted by solving the Least Squares Minimization problem with the following hyperbolic tangent function:

$$f(t) = \frac{A}{2} \cdot \left[1 - \tanh\left(-\frac{t - t_0}{\tau - t_0}\right)\right] , \tag{6.18}$$

where t_0 and τ are, respectively, the time required to reach 50% and 88% of the final heavy particle concentration, named A. The fitting curves are represented as dashed lines in Fig. 6.4 together with the raw data. In Fig. 6.5, the parameters A and τ of the hyperbolic tangent function are reported as a function of the density ratio. A can be estimated with

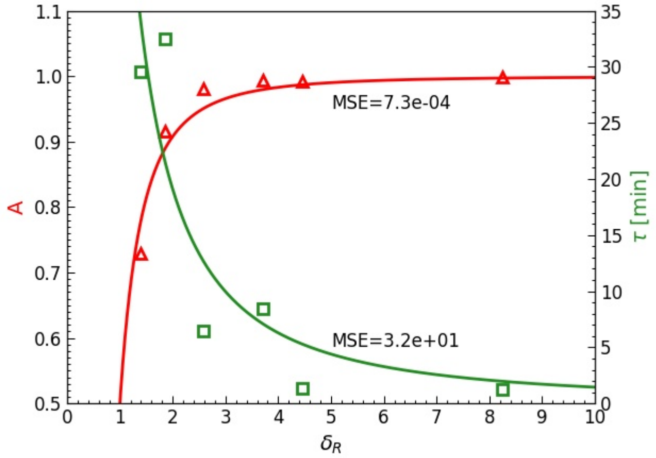

Figure 6.5: The fitting parameters A and τ are plotted as a function of the density ratio for $\phi_h = 50\%$. The first parameter refers to the left y-axis, whereas the latter refers to the right y-axis. The Mean Squared Errors (MSE) are also reported.

good accuracy (Mean Squared Error equal to $7.3 \cdot 10^{-4}$) with the following function:

$$A = 1 - \frac{1}{2 \cdot \delta_R^{\beta}} \qquad \delta_R > 1\,, \tag{6.19}$$

where $\beta = 2.27$ is an exponent characterizing the sensitivity of the final segregation state on the density ratio. For what concerns τ, it follows an exponential decay but, as the MSE reveals, its trend is not so accurate. In the limit of $\delta_R = 1$ (i.e. when the two species have the same density), the system is always perfectly mixed ($\phi_h = 50\%$) and segregation never occurs (diffusional mixing prevents separation). On the other hand, when δ_R becomes very large, the time required to reach the re-segregated state tends to 0, and segregation happens almost instantaneously.

To see in more detail how heavy particle concentration evolves in the entire flow depth, we have reconstructed the temporal evolution of the heavy particle concentration through the depth of the cell. The resulting contour maps are reported from Fig. 6.6 to Fig. 6.9 for increasing volume fractions, respectively. The contour maps are characterised by 100 contour regions and, to reduce the noise, concentrations have been smoothed over time by applying the moving average. In all cases, we can see that the time required by the heavy particles to reach the bottom is smaller than the time required by the lighter particles to reach the top. Furthermore, the final fully segregated state is, in general, reached faster in the case of higher δ_R and for 50:50 mixture composition. Nevertheless, the time required to reach the final configuration is higher for $\delta_R = 1.85$ than for $\delta_R = 1.40$, despite the higher density ratio. This is because, for $\delta_R = 1.85$, the total mass of grains is lower under the same load and determines a thinner shear band. This proves that the segregation rate depends on a combined effect of density ratio and loading mass. At the interface particles

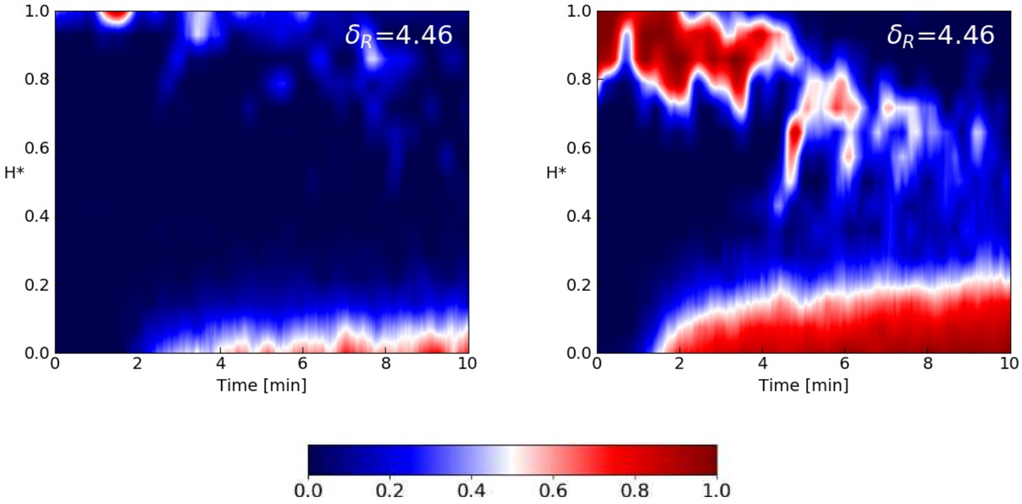

Figure 6.6: Experimental measurements of the heavy particle concentration distributions in time and as a function of the dimensionless cell height, H^* for $\phi_{h,0} = 10\%$ (on the left) and $\phi_{h,0} = 25\%$ (on the right). In both cases, $\delta_R = 4.46$. The colour bar refers to ϕ_h.

Pair	$\phi_{h,0}$	Mg [kg]	Mw/Mg [–]	Mw+Mg [kg]
C-PP	50%	2.67	0.41	3.77
G-PP	50%	2.04	0.54	3.14
G-POM	50%	2.52	0.44	3.62

Table 6.2: The segregation model has been tested for these three cases that are characterized by a similar $\tilde{M} = M_w/M_g$ [-]. M_g and M_w are expressed in kg.

partially mix due to diffusion. The interface is sharper for higher δ_R and smoother for lower δ_R where diffusive remixing competes always more against segregation.

6.4.2 Validation of the theoretical model

Rather than deforming uniformly, granular materials under shear stresses develop shear bands, zones of intense shear close to essentially rigid regions [31]. Very little is known about the shear band and how the microstructure of individual grains affects movements in densely packed material [31]. Mueth et al. [31] found that at high packing density and slow shear rate, the key characteristics of the granular microstructure determine the shape of the velocity profile. Artoni et al. [24] demonstrated that the exponential decay appearing in the velocity profile (i.e. the δ appearing in Eq. 6.10) is strictly related to the ratio between the mass loaded on the system and the mass of the grains: $\tilde{M} \equiv M_w/M_g$.

For this reason, the segregation model is verified for three cases having a similar $\tilde{M}$, as reported in Tab. 6.2. According to Artoni et al. [24], the values of δ are set equal to $\delta = 0.18H$, $0.20H$ and $0.22H$. As it concerns k, preliminary tests showed that $k = 0.5$, 0.6 and 0.7 are reasonable values. The optimal values of k and δ are obtained from a full factorial design of simulations with root-mean-square deviation as a key performance

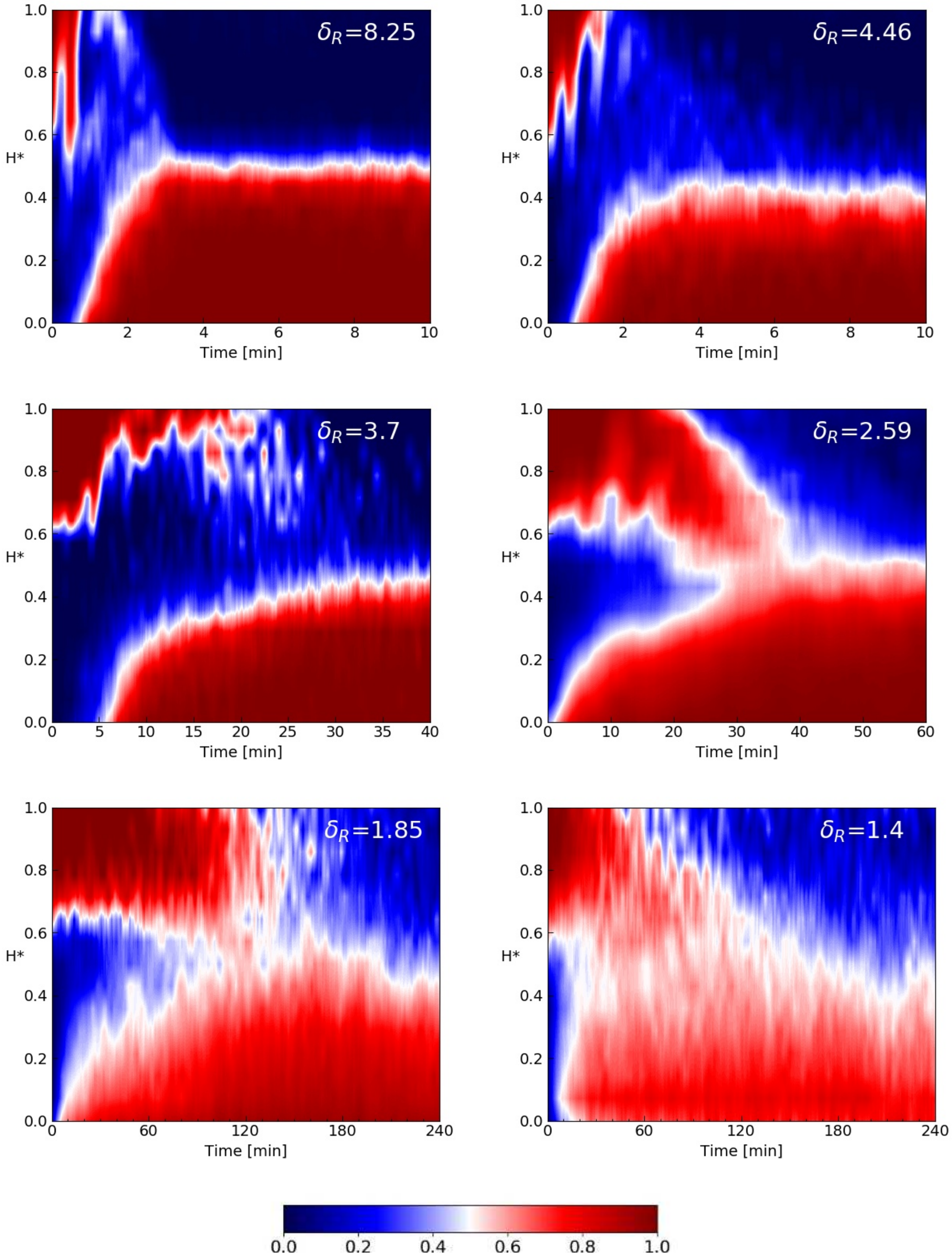

Figure 6.7: Experimental measurements of the heavy particle concentration distributions in time for $\phi_{h,0} = 50\%$ at decreasing density ratio.

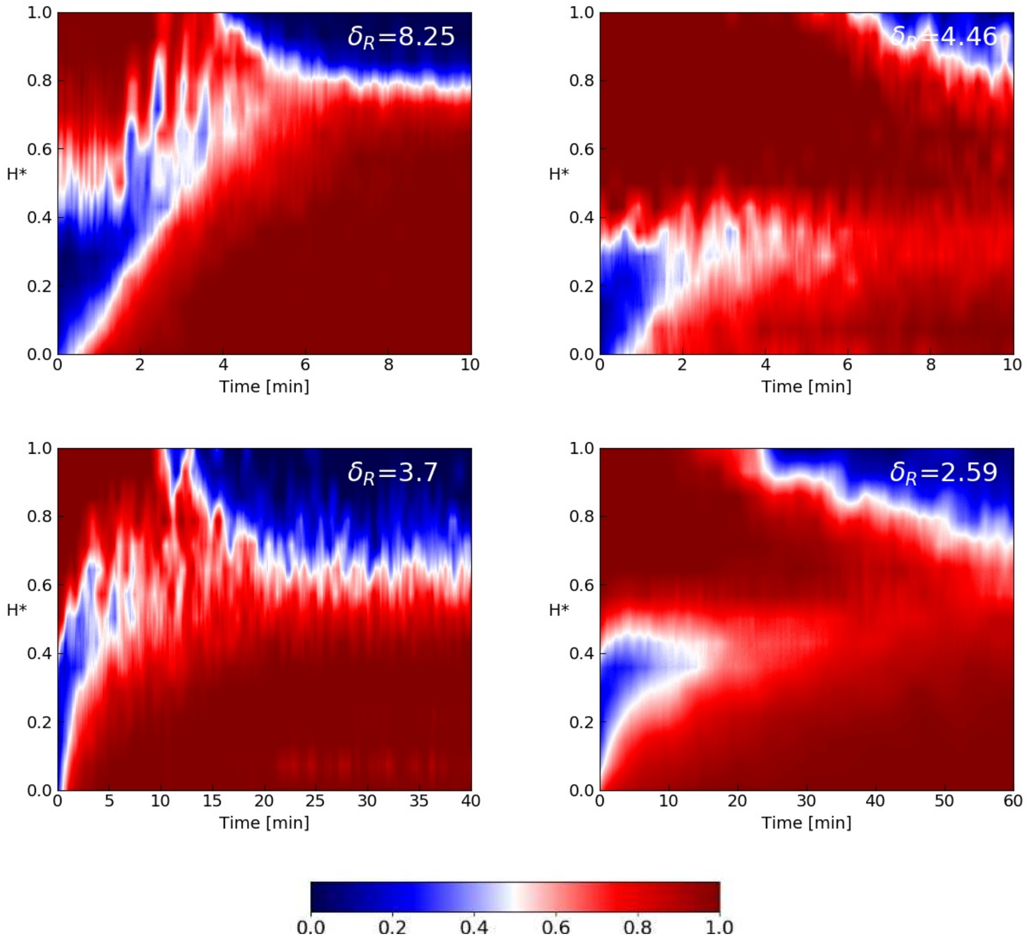

Figure 6.8: Experimental measurements of the heavy particle concentration distributions in time for $\phi_{h,0} = 75\%$ at decreasing density ratio.

indicator. The evaluation of the $RMSD$ between experimental and simulated contour maps (i.e. between matrices) is thus calculated as:

$$RMSD = \sqrt{\frac{\sum_{i=1}^{m}\sum_{j=1}^{n}(\phi_{ij,exp} - \phi_{ij,num})^2}{m \cdot n}}\,, \tag{6.20}$$

where m and n are the matrices dimensions. Tab. 6.3 lists, for each combination, the resulting $RMSD$ in the case of 50:50 mixtures of Ceramic and Polypropylene, Glass and Polypropylene and Glass and filled-POM. It is clear that the optimal combination of k and δ (i.e. the ones that minimize the RMSD) is $k = 0.7$ and $\delta = 0.18H$.

In Figs. 6.10, 6.11 and 6.12 the comparison between experimental findings and numerical results, computed with the optimal combination of k and δ, are reported for 50%, 75% and 90% volumetric fraction of the heavy component, respectively. As expected, the experimental results are much noisier than the numerical ones because of the discrete nature of the real system. However, since the $RMSD$ between experimental and

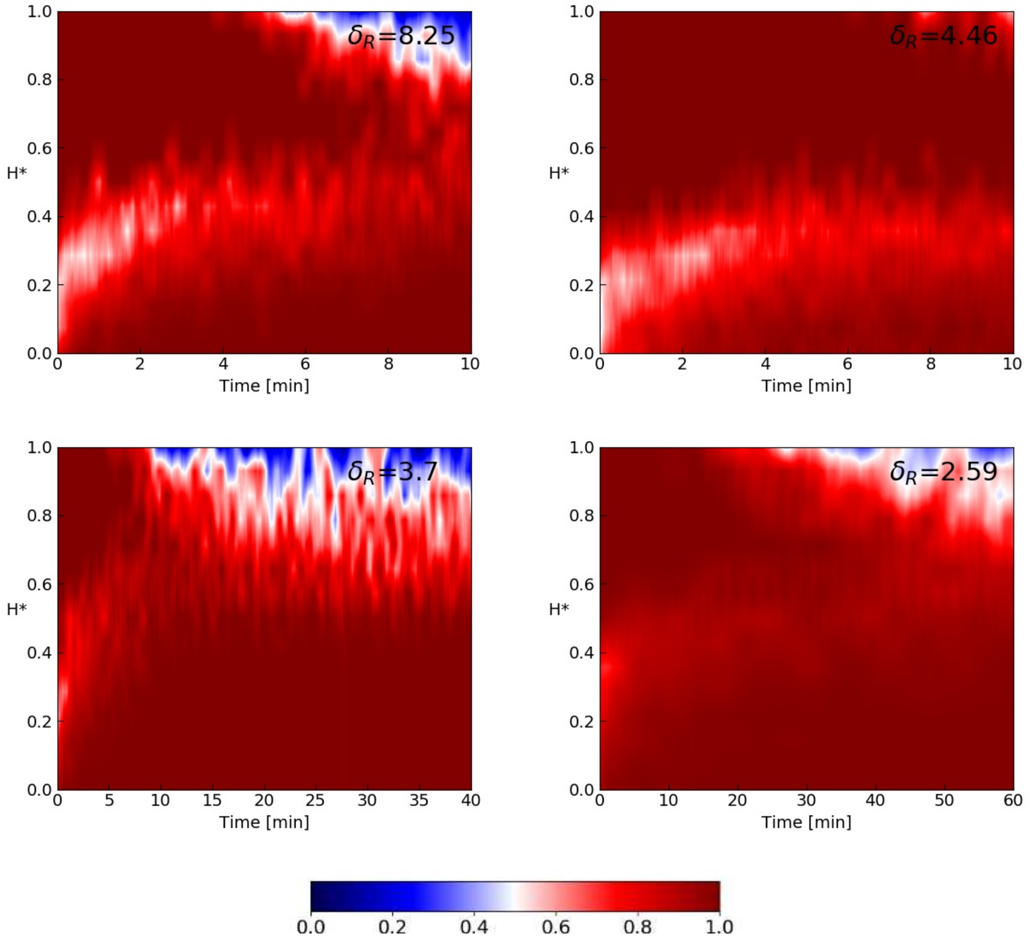

Figure 6.9: Experimental measurements of the heavy particle concentration distributions in time for $\phi_{h,0} = 90\%$ at decreasing density ratio.

Factors			RMSD		
ID	k	δ/H	C-PP	G-PP	G-POM
1	0.50	0.18	0.206	0.217	0.149
2	0.50	0.20	0.254	0.252	0.162
3	0.50	0.22	0.283	0.277	0.170
4	0.60	0.18	0.182	0.194	0.130
5	0.60	0.20	0.231	0.227	0.142
6	0.60	0.22	0.262	0.252	0.150
7	0.70	0.18	0.169	0.182	0.119
8	0.70	0.20	0.213	0.209	0.130
9	0.70	0.22	0.246	0.233	0.138

Table 6.3: The results obtained from the full factorial design of experiment for: 1) C-PP, 2) G-PP and 3) G-POM.

numerical outcomes is always smaller than 0.18, we can conclude that they agree both qualitatively and quantitatively. The proposed model is, therefore, able to capture the main features of density-driven segregation in the case of densely packed flow, also for non-homogeneous shear rates. It is also noteworthy that, numerically, we see more lighter particles at the outer surface. This is because our one-dimensional model cannot capture the three-dimensional recirculation pattern that develops, especially for higher $\tilde{M}$, within the real system (i.e. in reality, the wall affects the particle velocity field and creates a radial profile).

Fig. 6.13 reports the values of the parameters A and τ achieved numerically for a range of density ratios and 50:50 mixture composition, again considering the optimal combination of k and δ. In there, the dashed lines refer to the experiments. The parameter A is always well predicted by the model, however, there are some discrepancies in the prediction of τ. This means that, even if the model can predict the degree of segregation well for all density ratios, it sometimes fails to capture the rate of segregation. In Section 6.4.3, we will prove that this is because the dynamics of the granular flow is strictly related to δ, which in turn is sensitive to $\tilde{M}$. For instance, the cases with $\delta_R = 8.25$ and $\delta_R = 4.46$ are characterized by a greater $\tilde{M}$ and hence, δ should be higher than 0.18 in order to have reliable results.

We have seen that to successfully seize the dynamic of the process, δ and k must be opportunely fit. Nevertheless, independently of the process rate, the model can always well predict the final configuration. This is proven also in Fig. 6.14, where the experimental fully-developed profiles of the heavy particle concentration are compared with the numerical ones. For all density ratios, the model can well capture the main features of segregation: the profile is S-shaped and smooth, and the smoothness is higher for smaller density ratios where diffusional mixing gains a quite significant improvement over segregation.

6.4.3 Shear localization and velocity profile

Artoni et al. [24] showed that the velocity profile is not universal but depends on the flow parameters. Furthermore, the exponential decay is affected by the joint effect of normalized applied load, $\tilde{M}$, and flow depth. In the limit of small $\tilde{M}$, the pressure at the bottom is low with respect to that induced by the grains, and the shear localizes in a wider band. A decrease in the flow depth acts in the same way. In our case, the flow is always 15 particle diameters depth and hence, the only factor influencing δ is the normalized applied weight.

To prove that the dynamics of granular flow is strictly related to the height of the shear band, which in turn is linked to the normalized applied weight, we have performed velocity profile measurements with monodisperse particle systems, except for the steel because too heavy to be supported by the motor. The operating conditions were the same as for the segregation experiments. Unlike before, the process was recorded with a high-speed

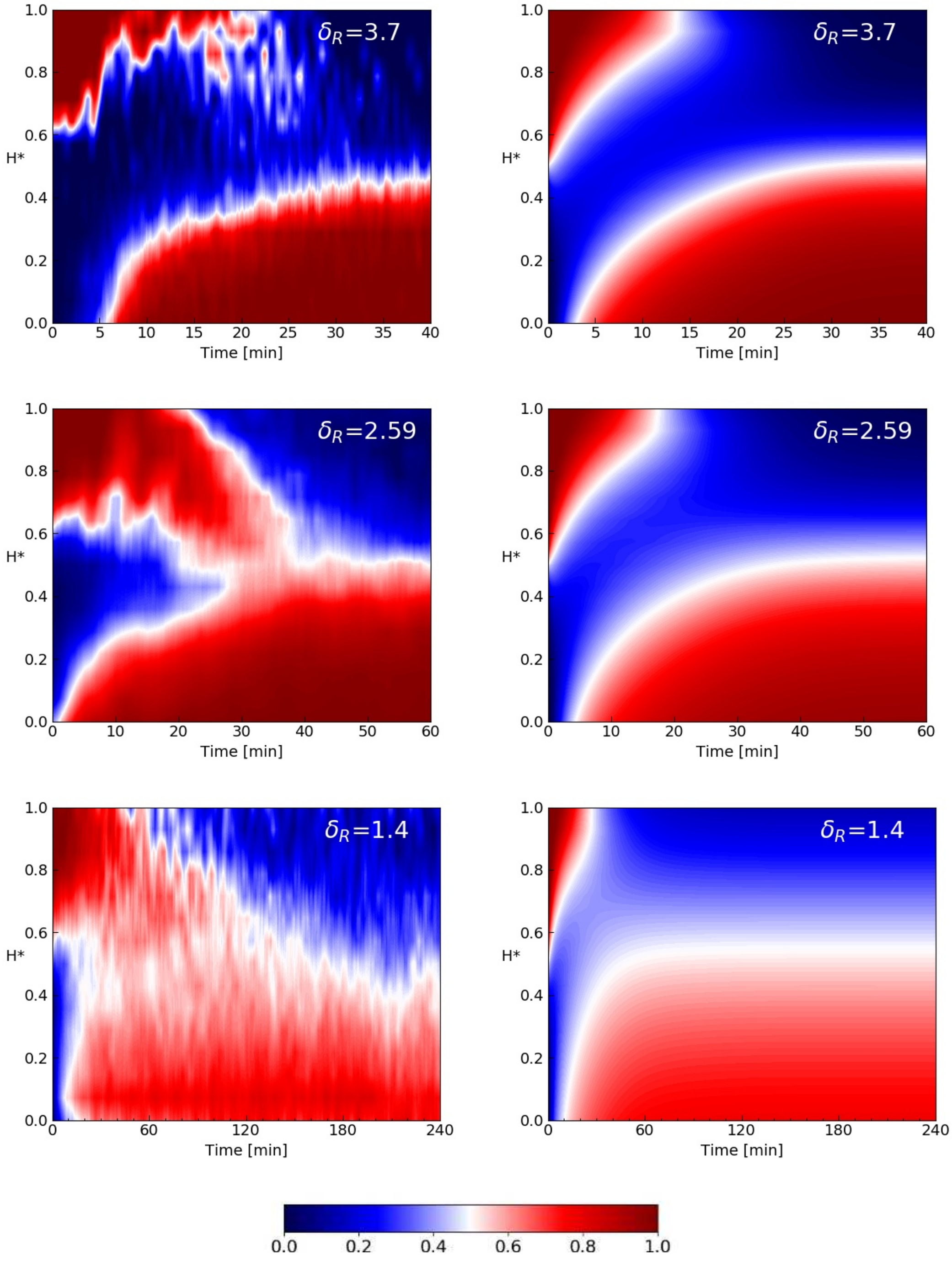

Figure 6.10: Comparison between experimental finding (first column) and numerical results (second column) for $\phi_{h,0} = 50\%$. The numerical contour maps have been obtained with the optimal combination of k and δ. The RMSD are: 0.169, 0.182 and 0.119 for δ_R equal to $3.70 - 2.59 - 1.40$ respectively.

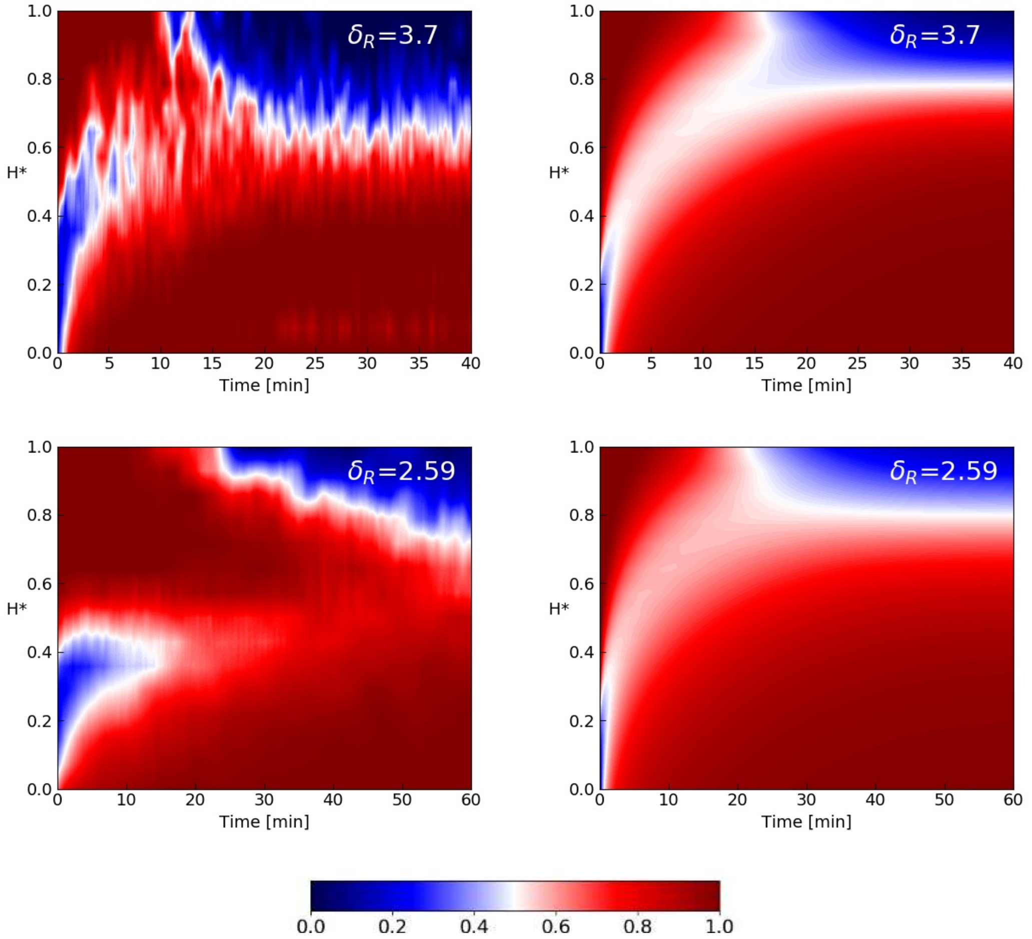

Figure 6.11: Comparison between experimental finding (first column) and numerical results (second column) for $\phi_{h,0} = 75\%$. The numerical contour maps have been obtained with the optimal combination of k and δ. The RMSD are: 0.166 and 0.176 for δ_R equal to 3.70 and 2.59 respectively.

camera (Phantom Miro 320S) at 24, 100 and 1000 fps. Working with different frame rates allowed us to obtain meaningful profiles for all the flow depths. The videos were processed with the free software ImageJ. The displacement of particles between consecutive frames was manually tracked and the velocity profile reconstructed by connecting the segments obtained at different frame rates.

We also carried out discrete element method (DEM) simulations to obtain the velocity profiles of glass and steel. As contact force model, we employed the linear spring-dashpot model based on a Hooke-type relation with CDT (Constant Directional Torque) rolling friction. Table 6.4 shows the simulation parameters implemented, together with some system information. The simulated annular shear cell had the same dimension as the real one (see Fig. 6.1) and finite boundary conditions in all directions. The top and bottom bumpy walls were represented with the same mesh used for the 3D printing of the real ones. On the top wall, 10.72 N of loading acting on the negative z-direction was applied

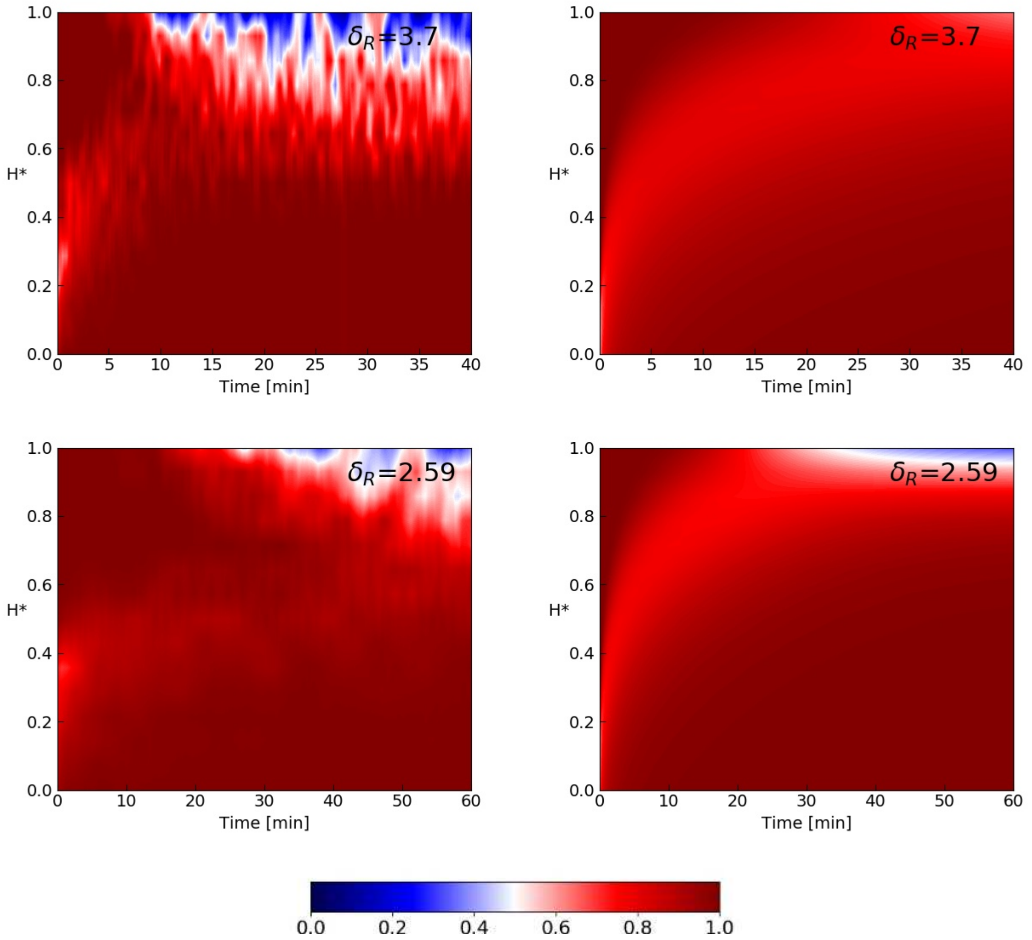

Figure 6.12: Comparison between experimental finding (first column) and numerical results (second column) for $\phi_{h,0} = 90\%$. The numerical contour maps have been obtained with the optimal combination of k and δ. The RMSD are: 0.175 and 0.091 for δ_R equal to 3.70 and 1.40 respectively.

and the bottom wall was rotated at a constant rotational speed of 23.44 rpm. The sliding friction coefficient between particle and wall was set equal to 0.33. Since the velocity profile of glass agrees with the experimental one, our simulation is quantitatively valid and the simulated profile of steel, which was impossible to determine experimentally, can be considered trustworthy.

Fig. 6.15 shows the velocity profile thus obtained. The decay is steeper for Polypropylene and slighter for steel. The difference in the decay of the velocity profile agrees with what is reported in [24]. In the inset, the dimensionless coefficient of exponential decay is reported as a function of M_w/M_g. As expected, the steel is characterized by a wider shear band than lighter material under the same load. It is now evident that, consistently with our main assumption, δ is sensitive to $\tilde{M}$, and this influences the rate, but not the degree, of segregation.

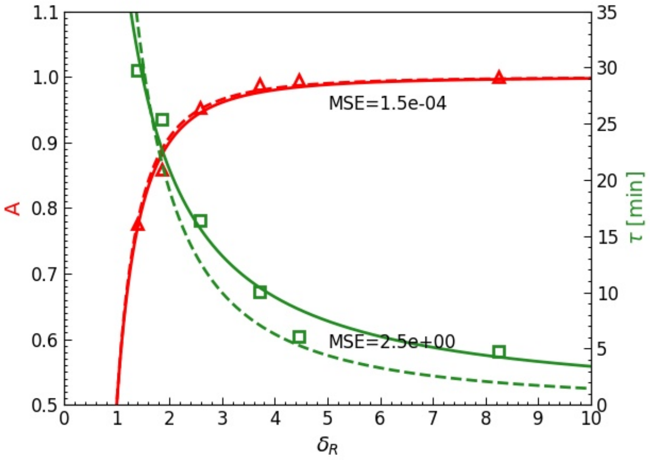

Figure 6.13: The fitting parameters A and τ that we obtained numerically with $k = 0.70$ and $\delta = 0.18$ are plotted as a function of the density ratio for $\phi_h = 50\%$. The first parameter refers to the left y-axis, whereas the latter refers to the right y-axis. The Mean Squared Errors (MSE) are also reported. For comparison, we have drawn also the fitting of the experimental parameters (dashed lines).

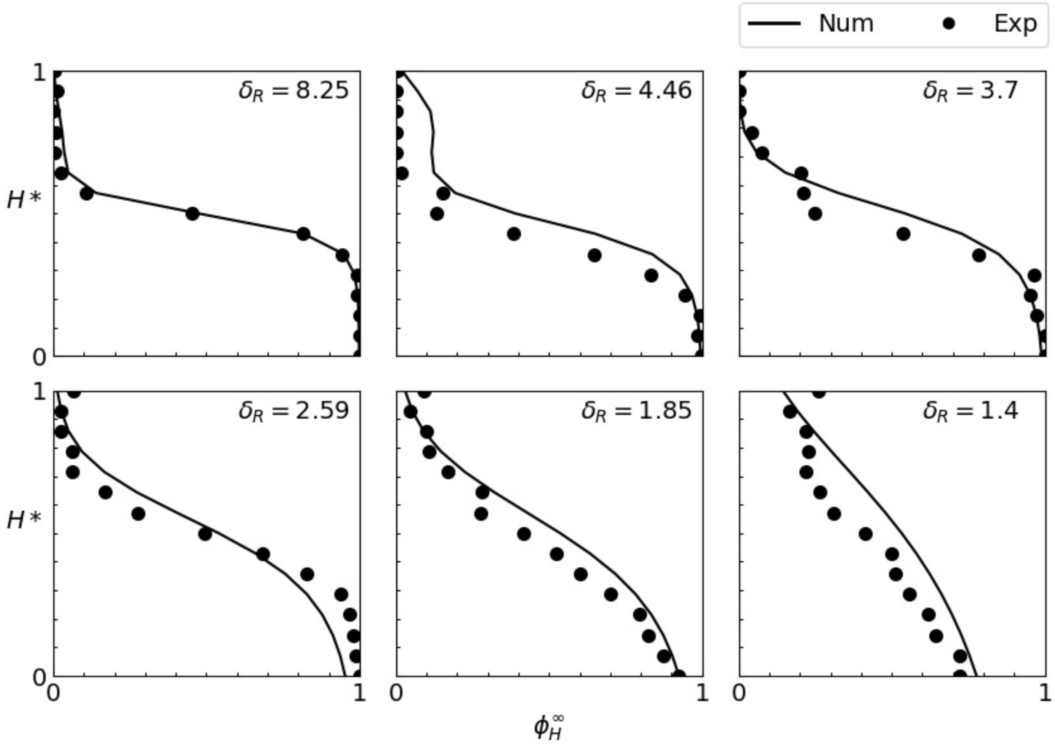

Figure 6.14: Comparison between experimental finding (dots) and numerical results (solid lines) for $\phi_{h,0} = 50\%$ for binary mixtures having different density ratios.

Variable	**Symbol**	**Value**
Particle diamater [m]	d_p	0.006
Intrinsic density of steel [kg/m^3]	ρ_S	7800
Intrinsic density of glass [kg/m^3]	ρ_G	2450
Normal elastic constant [N/m]	k_n	8.00e05
Tangential elastic constant [N/m]	k_t	2.29e05
Normal visco-elastic damping constant of steel [N/m]	$\gamma_{n,S}$	9.61e03
Normal visco-elastic damping constant of glass [N/m]	$\gamma_{n,G}$	1.71e04
Tangential visco-elastic damping constant [N/m]	γ_t	0
Restitution coefficient	e_n	0.70
Inter-particle friction	μ	0.20
Rolling friction coefficient	μ_r	0.005
Time step	Δt	$1e-6$
Wall-particle friction	μ_{wp}	0.33
Rotational speed [rpm]	Ω	23.44
Loading [N]	$\boldsymbol{F}_{load}$	-10.72
Gravity [m/s^2]	$\boldsymbol{g}$	-9.81
Boundary conditions	–	f f f

Table 6.4: A summary of the DEM simulation parameters.

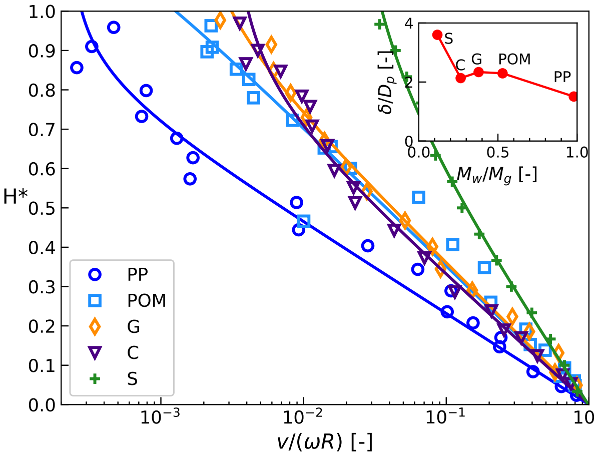

Figure 6.15: Velocity profile for the pure components. The profile for PP, POM, G and C were obtained from experiments, whereas the one of steel by DEM simulation.

6.5 Conclusions

For the first time, density-driven segregation has been experimentally studied in an annular shear cell where the flow is uninterrupted and where there is no need to feed the system. The experimental results show that two are the main factors influencing segregation: the density ratio and the flow features. In particular, the former influences the degree of segregation, the latter affects the rate of the segregation process. We have also shown that, in the limit of high normalized loaded mass, a three-dimensional flow pattern develops within the granular bed.

In this chapter, we have also provided a new density-driven segregation model with a segregation velocity analogous to the settling velocity predicted by Stokes' law. The model has been implemented and validated against experimental findings. The optimal values of the model parameters have been obtained by a full factorial design of the experiment aimed at minimizing the RMSD. The model can well predict the degree of segregation, for all density ratios. However, to predict accurately also the rate of the segregation process, one should accurately model the flow field. In our case, the flow field has been modelled using an exponential velocity profile. Thus, understanding the shear band localization (i.e. the degree of the exponential decay) has been crucial to describe granular flow onset and rheology [24].

The main advantage of our continuum model is that it permits analytical and fast numerical solutions for a range of density ratios and different volumetric fractions. The model can therefore be applied broadly for investigating and designing binary powder systems. The only drawback is that it requires accurate knowledge of the velocity profile since the shear localization features influence the rate of segregation. Further studies will be aimed to better understand the shear localization patterns, evaluate the effect of the wall friction coefficient and generalize the model to multicomponent systems with particles differing only by density.

Bibliography

[1] J. M. N. T. Gray. Particle Segregation in Dense Granular Flows. *Annu. Rev. Fluid Mech*, 50(1):407–33, 2018.

[2] D. V. Khakhar, J. J. McCarthy, and J. M. Ottino. Radial segregation of granular mixtures in rotating cylinders. *Physics of Fluids*, 9(12):3600–3614, 1997.

[3] J. A. Drahun and J. Bridgwater. The mechanisms of free surface segregation. *Powder Technology*, 36:39–53, 1983.

[4] M. Alonso, M. Satoh, and K. Miyanami. Optimum combination of size ratio, density ratio and concentration to minimize free surface segregation. *Powder Technology*, 68: 145–152, 1991.

[5] K. M. Hill, D. V. Khakhar, J. F. Gilchrist, J. J. McCarthy, and J. M. Ottino. Segregation-driven organization in chaotic granular flows. *Proceedings of the National Academy of Sciences of the United States of America*, 96:11701–11706, 1999.

[6] Q. Shi, G. Sun, M. Hou, and K. Lu. Density-driven segregation in vertically vibrated binary granular mixtures. *Physical Review E - Statistical, Nonlinear, and Soft Matter Physics*, 75:3–6, 2007.

[7] K. M. Hill and Y. Fan. Isolating segregation mechanisms in a split-bottom cell. *Physical Review Letters*, 101:1–4, 2008.

[8] L. Sanfratello and E. Fukushima. Experimental studies of density segregation in the 3D rotating cylinder and the absence of banding. *Granular Matter*, 11:73–78, 2009.

[9] H. Xiao, P. B. Umbanhowar, J. M. Ottino, and R. M. Lueptow. Modelling density segregation in flowing bidisperse granular materials. *Proceedings of the Royal Society A: Mathematical, Physical and Engineering Sciences*, 472:1–21, 2016.

[10] A. Tripathi and D. V. Khakhar. Rheology of binary granular mixtures in the dense flow regime. *Physics of Fluids*, 23:1–12, 2011.

[11] A. Tripathi and D. V. Khakhar. Density difference-driven segregation in a dense granular flow. *Journal of Fluid Mechanics*, 717:643–669, 2013.

[12] D. R. Tunuguntla, O. Bokhove, and A. R. Thornton. A mixture theory for size and density segregation in shallow granular free-surface flows. *Journal of Fluid Mechanics*, 749:99–112, 2014.

[13] Y. Fan and K. M. Hill. Shear-induced segregation of particles by material density. *Physical Review E - Statistical, Nonlinear, and Soft Matter Physics*, 92:1–14, 2015.

[14] Y. Duan, P. B. Umbanhowar, J. M. Ottino, and R. M. Lueptow. Kinetic theory based segregation model for density-bidisperse dense granular flows. *arXiv: Soft Condensed Matter*, pages 1–17, 2019.

[15] J. M. N. T. Gray and C. Ancey. Particle-size and -density segregation in granular free-surface flows. *Journal of Fluid Mechanics*, 779:622–668, 2015.

[16] C. Zeilstra, M. A. Van Der Hoef, and J. A. M. Kuipers. Simulation of density segregation in vibrated beds. *Physical Review E - Statistical, Nonlinear, and Soft Matter Physics*, 77:1–13, 2008.

[17] A. Di Renzo, F. P. Di Maio, R. Girimonte, and B. Formisani. DEM simulation of the mixing equilibrium in fluidized beds of two solids differing in density. *Powder Technology*, 184(2):214–223, 2008.

[18] A. Jain, M. J. Metzger, and B. J. Glasser. Effect of particle size distribution on segregation in vibrated systems. *Powder Technology*, 237:543–553, 2013.

[19] S. K. Hajra and D. V. Khakhar. Radial segregation of ternary granular mixtures in rotating cylinders. *Granular Matter*, 13:475–486, 2011.

[20] D. V. Khakhar, A. V. Orpe, and S. K. Hajra. Segregation of granular materials in rotating cylinders. *Physica A: Statistical Mechanics and its Applications*, 318: 129–136, 2003.

[21] S. B. Savage and M. Sayed. Stresses developed by dry cohesionless granular materials sheared in an annular shear cell. *Journal of Fluid Mechanics*, 142:391–430, 1984.

[22] R. D. Wildman, T. W. Martin, J. M. Huntley, J. T. Jenkins, H. Viswanathan, X. Fen, and D. J. Parker. Experimental investigation and kinetic-theory-based model of a rapid granular shear flow. *Journal of Fluid Mechanics*, 602:63–79, 2008.

[23] L. B. H. May, L. A. Golick, K. C. Phillips, M. Shearer, and K. E. Daniels. Shear-driven size segregation of granular materials: Modeling and experiment. *Physical Review E*, 81:2–9, 2010.

[24] R. Artoni, A. Soligo, J. M. Paul, and P. Richard. Shear localization and wall friction in confined dense granular flows. *Journal of Fluid Mechanics*, 849:395–418, 2018.

[25] G. Bradski. The OpenCV Library. *Dr. Dobb's Journal of Software Tools*, 120:122–125, 2000.

[26] R. B. Bird, W. E. Stewart, and E. N. Lightfoot. *Transport phenomena.* Wiley, 2006.

[27] B. Utter and R. P. Behringer. Self-diffusion in dense granular shear flows. *Physical Review E - Statistical, Nonlinear, and Soft Matter Physics*, 69:1–12, 2004.

[28] A. M. Fry, P. B. Umbanhowar, J. M. Ottino, and R. M. Lueptow. Diffusion, mixing, and segregation in confined granular flows. *AIChE Journal*, 65:875–881, 2019.

[29] P. Jop, Y. Forterre, and O. Pouliquen. A constitutive law for dense granular flows. *Nature*, 441:727–730, 2006.

[30] G. D. R. MiDi. On dense granular flows. *European Physical Journal E*, 14(4):341–365, 2004.

[31] D. M. Mueth, G. F. Debregeas, G. S. Karczmar, P. J. Eng, S. R. Magel, and H. M. Jaeger. Signatures of granular microstructure in dense shear flows. *Nature*, 406: 385–388, 2000.

Chapter 7

A theory for size-driven segregation in compressible granular flows

In modelling granular flows and segregation, the bulk velocity field is usually assumed to be incompressible, though it is well known that perturbations of a granular assembly induces density changes. In this chapter, we lay the foundations for the development of a compressible-segregation model that accounts for granular flows compressibility.

7.1 Introduction

In modelling granular flows and segregation, the bulk velocity field is usually assumed to be incompressible. However, real granular flows are compressible and the solid volume fraction may vary. Accounting for particles compressibility becomes important especially when the rapid regime of flow is approached (since the dilatancy become stronger), in the case of mixtures characterized by very high polydispersity (i.e. packings of mixtures of particles of different sizes are denser than packings made of monodisperse grains) and when particles differ by density [1, 2].

Even if the inclusion of compressibility complicates the conservation equations, it removes the ill-posedness of the incompressible $\mu(I)-$rheology [3, 4]. Thus, compressibility has been introduced as a regularizing mechanism in a few flow models. As an example, the compressible I-dependent rheology (CIDR) proposed by Barker et al. [3] extends the $\mu(I)-$rheology to compressible deformations through combination with the critical-state soil mechanics [3]. Since compressibility must be associated with sufficient dissipation, Heyman et al. [4] introduced a bulk friction coefficient associated with volume changes. The problem is well-posed when the bulk friction coefficient is higher than a minimum threshold. Fannon et al. [5] applied the CIDR flow model to two forms of granular instability: an inclined plane and a plane shear. They showed that the model can quantitatively predict the instability properties observed experimentally. Furthermore, it performs better than its incompressible counterpart. In the framework of the CIDR flow model, Schaeffer et al. [6] introduced new constitutive laws for the inertial regime giving rise to the inertial compressible I-dependent rheology (*i*CIDR). This model can well capture the Bagnold scaling, a stress-strain rate relationship according to which the shear stress is proportional to the square of the strain rate [7].

The original CIDR flow model describes a monodisperse system of spherical particles. In this chapter, we employ a modified version of the CIDR model to describe the flow behaviour of a multi-component granular mixture. The modified version includes changes that consider the local averaged particle size. The full coupling between the granular flow model and the segregation equations leads to a new size-driven segregation model. The implementation and validation of the model are still ongoing work. Future studies will aim to build an analogous model for density-driven segregation. To the author knowledge, only Gray and Ancey [8] and Gilberg and Steiner [9] have modelled segregation considering the compressibility of the granular flow, but, unlike us, the first ones did not consider the deviatoric part of the stress tensor and the second ones resorted to the granular temperature equation.

7.2 Multifluid dynamical equation

Let us consider a multi-component mixture of n classes of spherical particles differing by size and an air phase surrounding the material and filling the interstitial voids. If it is assumed that the volume fraction of the air phase can vary locally, it holds that:

$$\sum_{k=1}^{n} \phi_k + \phi_{air} = 1\,, \tag{7.1}$$

and thus, the total solid volume fraction is $\nu = 1 - \phi_{air}$. This differs from the previous chapters where the air has always been incorporated into the particle phases. Given this, in this Section, we propose a new compressible-segregation model.

7.2.1 Segregation modelling

We employ a multifluid modelling approach. Each size class of particles and the air have to satisfy a separate set of conservation equations. The continuity equation for the generic solid class k, considering neither mass transfer nor mass sources, reads:

$$\frac{\partial}{\partial t}(\phi_k \rho_k^*) + \nabla \cdot (\phi_k \rho_k^* \boldsymbol{u_k}) = 0\,, \tag{7.2}$$

where $\boldsymbol{u_k}$ is the velocity field and the product $(\phi_k \rho_k^*) \equiv \rho_k$ is the partial density [10]. The linear momentum balance equation, always for k, reads:

$$\frac{\partial}{\partial t}(\phi_k \rho_k^* \boldsymbol{u_k}) + \nabla \cdot (\phi_k \rho_k^* \boldsymbol{u_k} \boldsymbol{u_k}) = \nabla \cdot \boldsymbol{\sigma_k} + \phi_k \rho_k^* \boldsymbol{g} + \boldsymbol{F_{b,k}} + \boldsymbol{F_k}\,, \tag{7.3}$$

where $\boldsymbol{\sigma_k}$ is the stress tensor of phase k, $\phi_k \rho_k^* \boldsymbol{g}$ is the body force due to gravity, $\boldsymbol{F_k}$ is the force exerted on k by air and $\boldsymbol{F_{b,k}}$ arise from the interaction between the bulk solid and the single-particle phase k. Note that, segregation is the result of the interaction between different sized particles. This interaction is given in the momentum balance due to the interaction force [9]. In Lagrangian form, the two conservation equations reduce to:

$$\frac{\mathrm{D}}{\mathrm{D}t}\boldsymbol{u_k} = \frac{1}{\phi_k \rho_k^*}\left[\nabla \cdot \boldsymbol{\sigma_k} + \boldsymbol{F_{b,k}} + \boldsymbol{F_k}\right] + \boldsymbol{g}\,. \tag{7.4}$$

For mathematical proof, refer to Appendix A.5. Analogously, the two conservation equations for air are:

$$\frac{\partial}{\partial t}\phi_{air} + \nabla \cdot (\phi_{air} \boldsymbol{u_{air}}) = 0\,, \tag{7.5}$$

$$\frac{\partial}{\partial t}(\phi_{air} \boldsymbol{u_{air}}) + \nabla \cdot (\phi_{air} \boldsymbol{u_{air}} \boldsymbol{u_{air}}) = \frac{1}{\rho_{air}^*}\left[\boldsymbol{\nabla} \cdot \boldsymbol{\sigma_{air}} - \sum_{k=1}^{n} \boldsymbol{F_k}\right] + \phi_{air} \boldsymbol{g}\,, \tag{7.6}$$

and in Lagrangian form:

$$\frac{\mathrm{D}}{\mathrm{D}t}\boldsymbol{u_{air}} = \frac{1}{\phi_{air} \rho_{air}^*}\left[\boldsymbol{\nabla} \cdot \boldsymbol{\sigma_{air}} - \sum_{k=1}^{n} \boldsymbol{F_k}\right] + \boldsymbol{g}\,. \tag{7.7}$$

To render these dynamical equations solvable, the effective stress tensors and the interphase forces require closure.

7.2.2 The CIDR rheology

This Section report the original CIDR flow model by Barker et al. [3]. Let us consider a monodisperse granular material. As reported in chapter 2, $\boldsymbol{\sigma}$ may be decomposed into $\boldsymbol{\sigma} = -p\boldsymbol{I} + \boldsymbol{\tau}$. When dilation or compression occurs, the normal stress tensor in the medium departs from the critical state pressure by [4]:

$$p = p_c \left(1 - \mu_b \frac{\mathrm{tr}(\boldsymbol{D})}{||\boldsymbol{S}||}\right)\,, \tag{7.8}$$

where $\mu_b(\phi)$ is a bulk friction coefficient associated with non-isochoric deformations (i.e. volume changes), $||\boldsymbol{S}||$ is the second invariant of the deviatoric strain-rate tensor $\boldsymbol{S}$, and $\boldsymbol{D}$ is the total strain-rate tensor. The total strain rate tensor $\boldsymbol{D}$ (defined in Eq. 2.31) can be split into a deviatoric and an isotropic contribution:

$$\boldsymbol{D} = \boldsymbol{S} + \frac{1}{3}\mathrm{tr}(\boldsymbol{D})\boldsymbol{I}\,. \tag{7.9}$$

Into matrix notation, $\boldsymbol{D}$ and $\boldsymbol{S}$ are respectively equal to:

$$\boldsymbol{D} = \frac{1}{2}\begin{bmatrix} 2\ \partial_x u_x & \partial_y u_x + \partial_x u_y & \partial_z u_x + \partial_x u_z \\ \partial_x u_y + \partial_y u_x & 2\ \partial_y u_y & \partial_z u_y + \partial_y u_z \\ \partial_x u_z + \partial_z u_x & \partial_y u_z + \partial_z u_y & 2\ \partial_z u_z \end{bmatrix} \tag{7.10}$$

$$\boldsymbol{S} = \frac{1}{2}\begin{bmatrix} 2\ (\partial_x u_x - \pi) & \partial_y u_x + \partial_x u_y & \partial_z u_x + \partial_x u_z \\ \partial_x u_y + \partial_y u_x & 2\ (\partial_y u_y - \pi) & \partial_z u_y + \partial_y u_z \\ \partial_x u_z + \partial_z u_x & \partial_y u_z + \partial_z u_y & 2\ (\partial_z u_z - \pi) \end{bmatrix} \tag{7.11}$$

with $\mathrm{tr}(\boldsymbol{S}) = 0$ and π defined as:

$$\pi \equiv \frac{1}{3}\mathrm{tr}(\boldsymbol{D}) = \frac{\partial_x u_x + \partial_y u_y + \partial_z u_z}{3} = \frac{\nabla \cdot \boldsymbol{u}}{3}\,. \tag{7.12}$$

For the closure of the $\boldsymbol{\tau}$, we have to consider the alignment and yield conditions. Considering compressibility, the alignment condition reads:

$$\frac{\boldsymbol{\tau}}{||\boldsymbol{\tau}||} = \frac{\boldsymbol{S}}{||\boldsymbol{S}||}\,, \tag{7.13}$$

whereas the generalized yield condition, which relates $||\boldsymbol{\tau}||$ with the critical pressure, is equal to [11]:

$$||\boldsymbol{\tau}|| = \mu p_c\,. \tag{7.14}$$

Introducing the yield condition (Eq. 7.14) into the alignment condition (Eq. 7.13) leads to a closure relation for the deviatoric stress tensor:

$$\boldsymbol{\tau} = \mu p_c \frac{\boldsymbol{S}}{||\boldsymbol{S}||}\,, \tag{7.15}$$

where $||\boldsymbol{S}||$ is:

$$\begin{aligned} ||S|| = 0.5\,\big[&2(\partial_x u_x - \pi)^2 + 2(\partial_y u_y - \pi)^2 + 2(\partial_z u_z - \pi)^2 + \\ &(\partial_y u_x - \partial_x u_y)^2 + (\partial_z u_x - \partial_x u_z)^2 + (\partial_y u_z - \partial_z u_y)^2\big]^{0.5}\,. \end{aligned} \tag{7.16}$$

Given Eq. 7.8 and Eq. 7.15, the stress–strain relationship becomes [4]:

$$\boldsymbol{\sigma} = -p_c\boldsymbol{I} + p_c\mu\frac{\boldsymbol{S}}{||\boldsymbol{S}||} + p_c\mu_b\frac{\mathrm{tr}(\boldsymbol{D})}{||\boldsymbol{S}||}\boldsymbol{I}\,. \tag{7.17}$$

The terms on the right-hand side represent, in order, the isotropic contribution, the deviatoric contribution and the non-isochoric deformations. The deviatoric contribution does not impart volume changes, whereas the isotropic one accounts for volume changes with identical stretching [10]. Note that, in the case of isochoric deformations (i.e. incompressible granular flow), $\mathrm{tr}(\boldsymbol{D}) = 0$, $\boldsymbol{D} = \boldsymbol{S}$ and the rheology reduces to the incompressible formulation of Jop et al. [12]. Remembering that the shear rate $\dot{\gamma} = 2||\boldsymbol{S}||$ and $\mathrm{tr}(\boldsymbol{D}) = \nabla \cdot \boldsymbol{u}$, the general compressibility rheology (Eq. 7.17) can be reformulated as:

$$\boldsymbol{\sigma} = -p_c \boldsymbol{I} + \eta(\nabla \boldsymbol{u} + \nabla \boldsymbol{u}^T) + \left(\eta_b - \frac{2}{3}\eta\right) \nabla \cdot \boldsymbol{u} \boldsymbol{I} \,, \tag{7.18}$$

where η and η_b denote the viscosity and the bulk viscosity of the solid, namely:

$$\eta \equiv \frac{p_c \mu}{\dot{\gamma}} \,, \tag{7.19}$$

$$\eta_b \equiv \frac{2 p_c \mu_b}{\dot{\gamma}} \,. \tag{7.20}$$

Analogously to the bulk viscosity of fluids, the bulk viscosity of solids accounts for the resistance of the solid phase against compression. The closures for critical pressure p_c, friction coefficient μ, and bulk friction coefficient μ_b, are discussed in Section 7.2.3.

Here, for the first time, the CIDR flow model is employed to describe multi-component mixtures of particles differing by size. In the case of n solid phases, each k constituent supports the phasic stress tensor $\boldsymbol{\sigma_k}$ that is a fraction of the total stress tensor $\boldsymbol{\sigma}$. The key assumption for partitioning the total stress tensor among different sized particles is that the smallest particles support less stress than the proportion of volume they occupy. In contrast, the large particles carry proportionately more of the load [13–17]. Following Marks et al. [16] and Tunuguntla et al. [17], the partitioning factor is:

$$f_k = \frac{d_k^\alpha \phi_k}{\sum_k d_k^\alpha \phi_k} \,, \tag{7.21}$$

where $\alpha = 2$ (i.e. since we aim at distributing the force acting on a volume of particles, the stress scales with the surface of the particle). The partitioning factors satisfy the following constraints: they sum to unity (i.e. $\sum_k f_k = 1$) and pure phase constituents carry all of the stress (i.e. $f_k = 1$). Therefore, the proportion of the stress carried out by each solid k is:

$$\nabla \cdot \boldsymbol{\sigma_k} = \nabla \cdot (f_k \boldsymbol{\sigma}) \,. \tag{7.22}$$

This rheology is included in the momentum balance of the species k (Eq. 7.4):

$$\frac{\mathrm{D}}{\mathrm{D}t} \boldsymbol{u_k} = \frac{1}{\phi_k \rho_k^*} \left[\nabla \cdot (f_k \boldsymbol{\sigma}) + \boldsymbol{F_{b,k}} + \boldsymbol{F_k}\right] + \boldsymbol{g} \,. \tag{7.23}$$

Thus, the closure problem reduces to finding appropriate constitutive expressions for 1) granular frictional viscosity, 2) granular bulk viscosity and 3) solid pressure pertaining to the bulk solid phase, and partitioning them:

$$\eta_k = f_k \eta \, , \; \eta_{b,k} = f_k \eta_b \;\text{ and } p_{c,k} = f_k p_c \, . \tag{7.24}$$

Eqs. 7.24, together with closures for p_c, μ and μ_b, completely describe the stress state of each solid phase. Note that, to close the dynamical equation for air one have simply to set the bulk (or volume) viscosity and the shear (or dynamic) viscosity.

7.2.3 Critical state pressure, local friction and dilatancy law

In this study, we consider dry cohesionless multi-sized grains in the dense-inertial regime during compressible flows. We retain the usual incompressible inertial number definition (see Eq. 2.37) but p has been substituted with the critical state pressure p_c [4, 6]:

$$I = \frac{\dot{\gamma}\mathcal{D}}{\sqrt{p_c/\rho^*}} \, , \tag{7.25}$$

where $\mathcal{D}$ is the average particle diameter [18, 19]:

$$\mathcal{D} = \frac{\sum_k \phi_k d_k}{\sum_k \phi_k} \, . \tag{7.26}$$

This choice does not impact the stability and well-posed criteria [4]. The inertial number can also be written as a function of the solid volume fraction [4, 6]:

$$I(\nu) \equiv \frac{\nu_c - \nu}{a} \, , \tag{7.27}$$

where ν_c corresponds to the critical volume fraction (it depends on the polydispersity of the grain-size distribution as well as the interparticle friction [6]) and a is a constant material parameter. Considering Eqs. 7.25 and 7.27, solving for p_c leads to an equation of state for the critical-state pressure:

$$p_c = \left(\frac{a\dot{\gamma}\mathcal{D}}{\nu_{max} - \nu} \right)^2 \rho^* \, . \tag{7.28}$$

The friction coefficient is rate-dependent and, therefore, it scales with the inertial number. The most commonly used friction law was developed by Jop et al. [12] (see Eq. 2.41). To overcome the assumption of incompressibility, the variations of ν is included within the variations of the friction coefficient:

$$\mu(I) = \mu_s + \frac{\mu_2 - \mu_s}{\frac{aI_0}{\nu_c - \nu} + 1} \, . \tag{7.29}$$

For what concerns the bulk friction coefficient, it directly controls the amplitude of the pressure variations in the compressible flow. In contrast to μ, little is known about its value and its variations [4]. However, there exists a lower threshold below which the CIDR rheology is ill-posed [4]. To guarantee the well-posedness of the method at any inertial number, we set as first attempt μ_b to be 20% higher than the minimum threshold:

$$\mu_b(I) = 1.2 \left[1 - \frac{7}{6}\mu(I) \right] . \tag{7.30}$$

The bulk viscosity can play an interesting role in granular dense flows, however, since it has never been measured so far, more work is needed [20].

7.2.4 Particle-particle interaction forces

To model the interaction forces at low inertial numbers, we assume that the force exerted on k by the other solid classes has two contributions: 1) a grain-grain interaction force and 2) an interaction drag [16, 17]. Contributions such as lift forces or virtual mass are instead neglected. Unlike Gray and Thornton [13] and Gray and Chugunov [14], we employ a drag force that is inversely proportional to the shear rate so that the drag force reduces with increasing fluctuation in local pore creation [16, 17]. The particle-particle interaction force is therefore closed using the expression proposed by Tunuguntla et al. [17]:

$$\boldsymbol{F_{b,k}} = p_c \nabla f_k - \frac{\phi_k \rho_k^* C_{D,k}}{\dot{\gamma}} (\boldsymbol{u_k} - \boldsymbol{u_b}) , \tag{7.31}$$

where $C_{D,k}$ is the drag coefficient. Because the exact nature of the parameter $C_{D,k}$ for systems characterized by long-lasting particle-particle interactions is still poorly understood, as a first approximation, the same constant value of C_D can be set for all the constituents. Note that $C_D/\dot{\gamma}$ has dimension s^{-1} and $\sum_{k=1}^{n} \boldsymbol{F_{b,k}} = 0$. About the bulk velocity, it is simply $\boldsymbol{u_b} = \sum(u_k \phi_k)/\sum \phi_k$ since all particles have the same intrinsic density. Introducing Eq. 7.31 into Eq. 7.23 yields:

$$\frac{\mathrm{D}}{\mathrm{D}t}\boldsymbol{u_k} = \frac{1}{\phi_k \rho_k^*} \left[-f_k \nabla p_c + \nabla \cdot (f_k \boldsymbol{\tau'}) + \boldsymbol{F_k} \right] - \frac{C_D}{\dot{\gamma}} (\boldsymbol{u_k} - \boldsymbol{u_b}) + \boldsymbol{g} . \tag{7.32}$$

Notice that the grain-grain interaction force $p_c \nabla f_k$ combined to the partial pressure gradient $-\nabla(f_k p_c)$, leaved $-f_k \nabla p_c$ [14].

7.2.5 Fluid-particle interaction forces

Proper quantification of fluid–particle interactions is crucial for obtaining good model performances [21]. Here, we consider that the interaction force between air and particle consists of buoyancy and drag: $F_k = F_k^B + F_k^D$ [22]. The buoyancy is simply defined as $-\phi_k \nabla p$ where p is the static pressure. The drag force is instead $F_k^D = K_k(\boldsymbol{u_{air}} - \boldsymbol{u_k})$, where K_k is the fluid-solid exchange coefficient. The latter can be modelled as proposed by Gidaspow et al. [23]. Thus, it is:

$$K_k = \begin{cases} \frac{3}{4} C'_D \frac{\phi_k \phi_{air} \rho_{air} |\boldsymbol{u_k} - \boldsymbol{u_{air}}|}{d_k} \phi_{air}^{-2.65}, & \text{if } \phi_{air} > 0.80 \\ 150 \frac{\phi_k (1-\phi_{air}) \eta_{air}}{\phi_{air} d_k^2} + 1.75 \frac{\phi_k \rho_{air} |\boldsymbol{u_k} - \boldsymbol{u_{air}}|}{d_k}, & \text{if } \phi_{air} \leq 0.80 \end{cases} \tag{7.33}$$

where η_{air} is the viscosity of air and C'_D is the drag coefficient:

$$C'_D = \frac{24}{\phi_{air} Re_k} \left[1 + 0.15 (\phi_{air} Re_k)^{0.678} \right] . \tag{7.34}$$

In the latter expression, Re_k is the Reynold number at the minimum fluidized condition.

7.3 Conclusions

Granular flows are prone to dilate or contract in response to deformation [4]. This determines local variation of the flow field, porosity and components distribution. For this reason, we have speculated a new compressible-segregation model.

A modified version of the compressible inertial-dependent rheology developed by Barker et al. [3] and regularized by Heyman et al. [4] against the Hadamard (short-wavelength) instability is coupled with an Eulerian-Eulerian multifluid model describing a segregating system. Despite the high computational cost, the model might allow the evolution of the void space within the powder bed to be tracked. The model represents a starting point for future developments in the modelling of size-driven segregation. The model should be implemented and validated for simple flow geometries. It is necessary to investigate whether its additional complexity yields predictions that more accurately capture experimental results. Future works aim to develop an analogous model for size-driven segregation.

Bibliography

[1] L. B. H. May, L. A. Golick, K. C. Phillips, M. Shearer, and K. E. Daniels. Shear-driven size segregation of granular materials: Modeling and experiment. *Physical Review E*, 81:2–9, 2010.

[2] B. Andreotti, Y. Forterre, and O. Pouliquen. *Granular media: between fluid and solid*. Cambridge University Press, 2013.

[3] T. Barker, D. G. Schaeffer, M. Shearer, and J. M.N.T. Gray. Well-posed continuum equations for granular flow with compressibility and (I)-rheology. *Proceedings of the Royal Society A: Mathematical, Physical and Engineering Sciences*, 473(2201), 2017.

[4] J. Heyman, R. Delannay, H. Tabuteau, and A. Valance. Compressibility regularizes the μ(I)-rheology for dense granular flows. *Journal of Fluid Mechanics*, 830:553–568, 2017.

[5] J. S. Fannon, I. R. Moyles, and A. C. Fowler. Application of the compressible I-dependent rheology to chute and shear flow instabilities. *Journal of Fluid Mechanics*, 864:1026–1057, 2019.

[6] D. G. Schaeffer, T. Barker, D. Tsuji, P. Gremaud, M. Shearer, and J. M.N.T. Gray. Constitutive relations for compressible granular flow in the inertial regime. *Journal of Fluid Mechanics*, 874:926–951, 2019.

[7] L. E. Silbert, D. Ertaş, G. S. Grest, T. C. Halsey, D. Levine, and S. J. Plimpton. Granular flow down an inclined plane: Bagnold scaling and rheology. *Physical Review E*, 64(5):051302, 2001.

[8] J. M. N. T. Gray and C. Ancey. Particle-size and -density segregation in granular free-surface flows. *Journal of Fluid Mechanics*, 779:622–668, 2015.

[9] D. Gilberg and K. Steiner. Size segregation in compressible granular shear flows of binary particle systems. *Granular Matter*, 22(2):1–15, 2020.

[10] L. W. Morland. Flow of viscous fluids through a porous deformable matrix. *Surveys in Geophysics*, 13(3):209–268, 1992.

[11] G. D. R. MiDi. On dense granular flows. *European Physical Journal E*, 14(4):341–365, 2004.

[12] P. Jop, Y. Forterre, and O. Pouliquen. A constitutive law for dense granular flows. *Nature*, 441:727–730, 2006.

[13] J. M.N.T. Gray and A. R. Thornton. A theory for particle size segregation in shallow granular free-surface flows. *Proceedings of the Royal Society A: Mathematical, Physical and Engineering Sciences*, 461(2057):1447–1473, 2005.

[14] J. M. N. T. Gray and V. A. Chugunov. Particle-size segregation and diffusive remixing in shallow granular avalanches. *Journal of Fluid Mechanics*, 569:365–398, 2006.

[15] J. M.N.T. Gray and C. Ancey. Multi-component particle-size segregation in shallow granular avalanches. *Journal of Fluid Mechanics*, 678:535–588, 2011.

[16] B. Marks, P. G. Rognon, and I. Einav. Grainsize dynamics of polydisperse granular segregation down inclined planes. *Journal of Fluid Mechanics*, 690:499–511, 2012.

[17] D. R. Tunuguntla, O. Bokhove, and A. R. Thornton. A mixture theory for size and density segregation in shallow granular free-surface flows. *Journal of Fluid Mechanics*, 749:99–112, 2014.

[18] P. G. Rognon, J. N. Roux, M. Naaïm, and F. Chevoir. Dense flows of bidisperse assemblies of disks down an inclined plane. *Physics of Fluids*, 19(5):15–19, 2007.

[19] A. Tripathi and D. V. Khakhar. Rheology of binary granular mixtures in the dense flow regime. *Physics of Fluids*, 23:1–12, 2011.

[20] M. Trulsson, M. Bouzid, P. Claudin, and B. Andreotti. Dynamic compressibility of dense granular shear flows. *Epl*, 103(3), 2013. ISSN 02955075.

[21] F. Cello, A. Di Renzo, and F. P. Di Maio. A semi-empirical model for the drag force and fluid-particle interaction in polydisperse suspensions. *Chemical Engineering Science*, 65(10):3128–3139, 2010.

[22] L. Mazzei, A. Casillo, P. Lettieri, and P. Salatino. CFD simulations of segregating fluidized bidisperse mixtures of particles differing in size. *Chemical Engineering Journal*, 156(2):432–445, 2010.

[23] D. Gidaspow, R. Bezburuah, and J. Ding. Hydrodynamics of circulating fluidized beds: kinetic theory approach. Technical report, Illinois Inst. of Tech., Chicago, IL (United States). Dept. of Chemical . . . , 1991.

Chapter 8

Conclusions and perspectives

This thesis focuses on the development of continuum segregation models in dense sheared granular flows. All the models proposed have been validated against either experiments or simulations, and allow a better understanding of the segregation features in different flow configurations. The main conclusion of the work, which lies in between granular physics and particle technology, are drawn in Section 8.1. In Section 8.2, we propose some perspectives for future works.

8.1 Conclusions

The first part of this thesis is dedicated to segregation driven by size in different flow configurations. As a first and preliminary step, we have considered diluted binary mixtures (chapter 3). We have proposed a reliable model for a small isolated particle percolating through a mono-disperse bed of coarse grains when subjected to shear. The model, which arises from physical considerations and probabilistic assumptions, well captures both experimental and DEM results for a range of shear rates and diameter ratios. This theory has been successively generalized to the case of multi-component granular mixtures made up of discrete solid phases differing only in size (chapter 4). Such a generalized model has been implemented in a continuum framework and fully coupled with a solid flow rheology. To test whether the model can successfully represent the reality, we have employed data taken from the literature concerning the discharge of ternary mixtures from a storage hopper. It has appeared that the model can well predict segregation for almost all the discharge process. The only discrepancies are related to the very final stage of the discharge. Aware of the fact that real granular mixtures are typically polydisperse over their size, we have also proposed a new theory for modelling segregation in polydisperse granular mixtures (chapter 5). We have tracked the evolution of the particle size distribution in space and time by means of the DQMOM and solved the transport equations for the weights and weighted nodes in a CFD software. Since developing an experimental setting for segregation in polydisperse granular mixtures is very challenging, we have validated the model through DEM simulations. We have proven that the theoretical results are in very good qualitative agreement with the simulation outcomes. However, the model fails to quantitatively predict the correct evolution of the quadrature nodes under some circumstances. It is hoped that further insights concerning drag coefficient, diffusion and rheological behaviour of polydisperse granular systems will improve our predictions.

The second part of this thesis concerns the study of segregation in binary mixtures of spherical particles differing not by size but by density, and still subjected to shear rate (chapter 6). The predictions of the theoretical model have been compared with ad-hoc experimental data. As expected, the denser particles sink to the bottom and the less dense particles rise to the surface. Furthermore, we have shown that if the degree of segregation is enhanced for increasing density ratios, the rate of segregation is strictly influenced by the normalized applied load.

Finally, in chapter 7, we have offered some speculation regarding the inclusion of compression in modelling segregation.

To conclude, we can say that the proposed models are well-suited for predicting the segregation features of granular mixtures in nature and in industry, for several settings and flow configurations. They can be successfully applied for a range of mixture compositions and diameter (or density) ratios. Furthermore, they allow simulating segregation within large granular systems with reasonable computational costs (i.e. the number of particles is irrelevant). The only drawback of the models is that they might rely on fitting parameters having no clear physical meaning.

8.2 Future work

Even if this work represents a further step towards a complete and accurate description of segregation in a variety of dense granular flows, there are still several aspects that should be pursued in future research. Some of them are mentioned here as an outlook.

In deriving our segregation models, we have focused on systems of particles differing only by size (chapters 3, 4 and 5) or by density (chapter 6). However, it may be interesting to adapt and implement the models to particle systems differing simultaneously in both size and density. It would also be helpful to address the issue of segregation in more complex systems such as irregular-shaped particles, cohesion and interaction with interstitial fluid. Note that the interplay of size and density differences, as well as making the particles more cohesive by modifying particle shape, texture, surface condition and/or by adding moisture or a weak binding agent, may reduce or prevent segregation.

The widespread of polydisperse granular materials motivates further studies related to our CFD-PBE model (chapter 5). It seems reasonable that, the main discrepancies are related to the lack of reliable constitutive equations for the system under consideration. Thus, to improve the model accuracy, a systematic study of the rheological behaviour of polydisperse granular system is required.

In addition, in Chapter 7 we have begun to consider the inclusion of compressibility in modelling segregation. The chapter is only speculative and hence, a viable next step would be implementing and validating the model, and evaluating whether it is generally suitable for simulating segregation in compressible granular flows. If this is the case, it certainly would have several applications.

Finally, it would be interesting to link continuum and discrete modelling (i.e. DEM-CFD-based models). The connection between local and macro scale effects would be advantageous for the complete understanding of the phenomenon, for developing mitigation strategies relevant for industry and, more in general, for finding the solution of several particulate-based problems.

Appendix A

Mathematical proofs

A.1 Mean free distance between particles

Stereology gives a relationship to describe the mean free distance between randomly distributed neighbouring spheres. Referring to Fig. A.1, the distance between points a and b can be expressed as:

$$d_{ab} = d_{ac} - d_{bc} \, . \tag{A.1}$$

In Eq. A.1, the distance d_{ac} is proportional to:

$$d_{ac} \propto \frac{V_b}{S_p} \, , \tag{A.2}$$

where V_b is the volume of the void channel and S_p is the surface area of the packing. If we assume a regular packing of spheres having diameter d_c and being in static conditions, d_{ac} becomes:

$$d_{ac} = \frac{2}{3} \frac{d_c}{\nu} \, , \tag{A.3}$$

where ν is the solid volume fraction. If we generalize Eq. A.3 for the case of sheared systems, we get:

$$d_{ac} = k \frac{d_c}{\nu} \, , \tag{A.4}$$

where k is a parameter that takes into account the geometrical properties of the packing. Regarding the distance d_{bc} appearing in Eq. A.1, which is usually referred to as mean intercept length, it is equal to:

$$d_{bc} = \frac{2}{3} d_c \, . \tag{A.5}$$

The distance d_{ab} between two particles is, therefore:

$$d_{ab} = d_{ac} - d_{bc} = k \frac{d_c}{\nu} - \frac{2}{3} d_c \, . \tag{A.6}$$

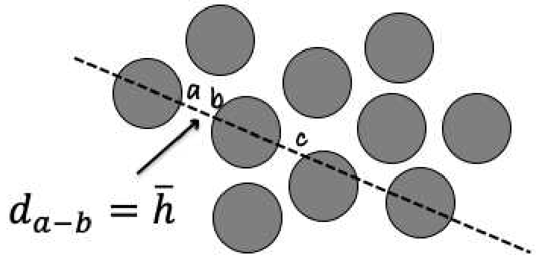

Figure A.1: Schematic representation of random spheres.

If we generalized this definition for the entire packing, we get that the mean distance between two surface points of neighbouring spheres is: $\bar{h} = d_{ab}$. Assuming that $k = 2/3k'$, we obtain:

$$\bar{h} = \frac{2}{3} d_c \left(\frac{k' - \nu}{\nu} \right) . \tag{A.7}$$

If the bed is isotropic and static, $k' = 1$, and thus:

$$\bar{h} = \frac{2}{3} d_c \left(\frac{1 - \nu}{\nu} \right) . \tag{A.8}$$

On the other hand, if the bed is dilated k' must be greater than 1.

A.2 Falling probability

The probability that the mean free distance $\bar{h}$ between particles in a granular bed is greater than the dimension of the percolating particle, d_f, reads:

$$P(h \geq d_f) = \exp\left(-\frac{d_f}{\bar{h}}\right) . \tag{A.9}$$

This probability, however, guarantees that the condition is satisfied only in one direction (let us say, for instance, x). To extend the validity in the other two directions, the probability must be written also for the $y-$ and $z-$directions:

$$P_x = P(h_x \geq d_f) = \exp\left[-\frac{1}{k_x}\frac{d_f}{d_c}\frac{\nu}{(1-\nu)}\right] , \tag{A.10}$$

$$P_y = P(h_y \geq d_f) = \exp\left[-\frac{1}{k_y}\frac{d_f}{d_c}\frac{\nu}{(1-\nu)}\right] , \tag{A.11}$$

$$P_z = P(h_z \geq d_f) = \exp\left[-\frac{1}{k_z}\frac{d_f}{d_c}\frac{\nu}{(1-\nu)}\right] . \tag{A.12}$$

If we assume that these three probabilities derive from three independent events, the global falling probability is simply given by their product:

$$P_f = P_x \cdot P_y \cdot P_z . \tag{A.13}$$

Substituting in Eq. A.13, the relations for P_x, P_y and P_z, we obtain:

$$P_f = \exp\left[-\left(\frac{1}{k_x}+\frac{1}{k_y}+\frac{1}{k_z}\right)\frac{d_f}{d_c}\frac{\nu}{(1-\nu)}\right] . \tag{A.14}$$

If we also assume that the bed is homogeneously dilated in the three directions (i.e. isotropic), we get $k_x = k_y = k_z \equiv k$ and hence:

$$P_f = \exp\left[-\frac{3}{k}\frac{d_f}{d_c}\frac{\nu}{(1-\nu)}\right] . \tag{A.15}$$

A.3 Derivation of the DQMOM transport equations

In this section, we aim to derive the DQMOM transport equations. The reduced Population Balance Equation describing our segregating system reads:

$$\frac{\partial}{\partial t}\hat{f}_v + \nabla_x \cdot \left(\hat{f}_v \boldsymbol{v_b}\right) + \nabla_x \cdot \left(\hat{f}_v \boldsymbol{v}_s\right) - \mathcal{D}\nabla_x^2 \hat{f}_v = 0\,. \tag{A.16}$$

If we solve the latter by employing the direct quadrature method of moments, we obtain:

$$\begin{gathered}\frac{\partial}{\partial t}\left(\sum_{\alpha=1}^{n}\phi_\alpha \delta\left(\xi-\xi_\alpha\right)\right) + \nabla_x \cdot \left(\sum_{\alpha=1}^{n}\phi_\alpha \delta\left(\xi-\xi_\alpha\right)\boldsymbol{v}_b\right) + \\ \nabla_x \cdot \left(\sum_{\alpha=1}^{n}\phi_\alpha \delta\left(\xi-\xi_\alpha\right)\boldsymbol{v}_{s,\alpha}\right) - \mathcal{D}\nabla_x^2\left(\sum_{\alpha=1}^{n}\phi_\alpha \delta\left(\xi-\xi_\alpha\right)\right) = 0\,.\end{gathered} \tag{A.17}$$

Each term of Eq. A.17 can be derived by considering that the following identity holds true:

$$\phi_\alpha \frac{\partial \xi_\alpha}{\partial t} = \frac{\partial(\phi_\alpha \xi_\alpha)}{\partial t} - \xi \frac{\partial \phi_\alpha}{\partial t}\,. \tag{A.18}$$

Thus, the derivative of the first term yields:

$$\begin{gathered}\frac{\partial}{\partial t}\left(\sum_{\alpha=1}^{n}\phi_\alpha \delta\left(\xi-\xi_\alpha\right)\right) = \sum_{\alpha=1}^{n}\left(\frac{\partial \phi_\alpha}{\partial t}\delta\left(\xi-\xi_\alpha\right) - \phi_\alpha \frac{\partial \xi_\alpha}{\partial t}\delta'\left(\xi-\xi_\alpha\right)\right) = \\ \sum_{\alpha=1}^{n}\left(\frac{\partial \phi_\alpha}{\partial t}\delta\left(\xi-\xi_\alpha\right) - \frac{\partial(\phi_\alpha \xi_\alpha)}{\partial t}\delta'\left(\xi-\xi_\alpha\right) + \xi \frac{\partial \phi_\alpha}{\partial t}\delta'\left(\xi-\xi_\alpha\right)\right)\,,\end{gathered} \tag{A.19}$$

where $\delta'\left(\xi-\xi_\alpha\right)$ denotes the derivative of $\delta\left(\xi-\xi_\alpha\right)$ with respect to ξ_α. From now on, we use the following nomenclatures for $\delta := \delta\left(\xi-\xi_\alpha\right)$ and its derivatives: $\delta' := \delta'\left(\xi-\xi_\alpha\right)$ and $\delta'' := \delta''\left(\xi-\xi_\alpha\right)$.

The other terms of Eq. A.17 are manipulated similarly. Thus, the second and third terms of the right-hand side become, respectively:

$$\begin{gathered}\nabla_x \cdot \left(\sum_{\alpha=1}^{n}\phi_\alpha \delta \boldsymbol{v_b}\right) = \sum_{\alpha=1}^{n}\left(\nabla_x \cdot (\phi_\alpha \boldsymbol{v_b})\delta - (\phi_\alpha \boldsymbol{v_b}) \cdot \nabla_x \xi_\alpha \delta'\right) = \\ \sum_{\alpha=1}^{n}\left(\nabla_x \cdot (\phi_\alpha \boldsymbol{v_b})\delta - \nabla_x(\phi_\alpha \boldsymbol{v_b}\xi_\alpha)\delta' + \xi_\alpha \nabla_x \cdot (\phi_\alpha \boldsymbol{v_b})\delta'\right)\,,\end{gathered} \tag{A.20}$$

$$\begin{gathered}\nabla_x \cdot \left(\sum_{\alpha=1}^{n}\phi_\alpha \delta \boldsymbol{v_{s,\alpha}}\right) = \sum_{\alpha=1}^{n}\left(\nabla_x \cdot (\phi_\alpha \boldsymbol{v_{s,\alpha}})\delta - (\phi_\alpha \boldsymbol{v_{s,\alpha}}) \cdot \nabla_x \xi_\alpha \delta'\right) = \\ \sum_{\alpha=1}^{n}\left(\nabla_x \cdot (\phi_\alpha \boldsymbol{v_{s,\alpha}})\delta - \nabla_x(\phi_\alpha \boldsymbol{v_{s,\alpha}}\xi_\alpha)\delta' + \xi_\alpha \nabla_x \cdot (\phi_\alpha \boldsymbol{v_{s,\alpha}})\delta'\right)\,,\end{gathered} \tag{A.21}$$

whereas, the manipulation of the diffusive term yields:

$$\begin{gathered}\mathcal{D}\nabla_x^2\left(\sum_{\alpha=1}^{n}\phi_\alpha\delta\right)=\mathcal{D}\sum_{\alpha=1}^{n}\nabla_x\cdot\left(\nabla_x\phi_\alpha\delta-\phi_\alpha\nabla_x\xi_\alpha\delta'\right)=\\ \mathcal{D}\sum_{\alpha=1}^{n}\left(\delta\nabla_x^2\phi_\alpha-2\delta'\nabla_x\phi_\alpha\nabla_x\xi_\alpha-\delta'\phi_\alpha\nabla_x^2\xi_\alpha+\delta''\phi_\alpha\nabla_x\xi_\alpha\cdot\nabla_x\xi_\alpha\right)\,.\end{gathered}\tag{A.22}$$

Using the following identity:

$$\nabla_x^2(f(\boldsymbol{x})g(\boldsymbol{x}))=f(\boldsymbol{x})\nabla_x^2g(\boldsymbol{x})+2\nabla_xf(\boldsymbol{x})\cdot\nabla_xg(\boldsymbol{x})+g(\boldsymbol{x})\nabla_x^2f(\boldsymbol{x})\,,\tag{A.23}$$

the diffusive term in Eq. A.22 becomes:

$$\begin{gathered}\mathcal{D}\nabla_x^2\left(\sum_{\alpha=1}^{n}\phi_\alpha\delta\right)=\\ \mathcal{D}\sum_{\alpha=1}^{n}\left(\delta\nabla_x^2\phi_\alpha-\delta'\nabla_x^2(\phi_\alpha\xi_\alpha)+\delta'\xi_\alpha\nabla_x^2\phi_\alpha+\delta''\phi_\alpha\nabla_x\xi_\alpha\cdot\nabla_x\xi_\alpha\right)\,.\end{gathered}\tag{A.24}$$

Introducing all the previous results in Eq. A.17 gives:

$$\begin{gathered}\sum_{\alpha=1}^{n}\left(\frac{\partial\phi_\alpha}{\partial t}\delta-\frac{\partial(\phi_\alpha\xi_\alpha)}{\partial t}\delta'+\xi\frac{\partial\phi_\alpha}{\partial t}\delta'+\nabla_x\cdot(\phi_\alpha\boldsymbol{v_b})\delta-\nabla_x(\phi_\alpha\boldsymbol{v_b}\xi_\alpha)\delta'+\right.\\ \xi_\alpha\nabla_x\cdot(\phi_\alpha\boldsymbol{v_b})\delta'+\nabla_x\cdot(\phi_\alpha\boldsymbol{v_{s,\alpha}})\delta-\nabla_x(\phi_\alpha\boldsymbol{v_{s,\alpha}}\xi_\alpha)\delta'+\xi_\alpha\nabla_x\cdot(\phi_\alpha\boldsymbol{v_{s,\alpha}})\delta'\\ \left.-\mathcal{D}\delta\nabla_x^2\phi_\alpha+\mathcal{D}\delta'\nabla_x^2(\phi_\alpha\xi_\alpha)-\mathcal{D}\delta'\xi_\alpha\nabla_x^2\phi_\alpha-\mathcal{D}\delta''\phi_\alpha\nabla_x\xi_\alpha\cdot\nabla_x\xi_\alpha\right)=0\,.\end{gathered}\tag{A.25}$$

If we now define the following DQMOM transport equations:

$$\frac{\partial}{\partial t}\phi_\alpha+\nabla_x\cdot(\phi_\alpha\boldsymbol{v}_b)+\nabla_x\cdot(\phi_\alpha\boldsymbol{v}_{s,\alpha})-\mathcal{D}\nabla_x^2\phi_\alpha\equiv c_\alpha^\phi\,,\tag{A.26}$$

$$\frac{\partial}{\partial t}\sigma_\alpha+\nabla_x\cdot(\sigma_\alpha\boldsymbol{v}_b)+\nabla_x\cdot(\sigma_\alpha\boldsymbol{v}_{s,\alpha})-\mathcal{D}\nabla_x^2\sigma_\alpha\equiv c_\alpha^\sigma\,,\tag{A.27}$$

the DQMOM for the monovariate VFD describing our segregating system reads:

$$\sum_{\alpha=1}^{n}\left[c_\alpha^\phi(\boldsymbol{x},t)\delta-(c_\alpha^{\phi\xi}(\boldsymbol{x},t)-\xi_\alpha c_\alpha^\phi(\boldsymbol{x},t))\delta'\right]=\sum_{\alpha=1}^{n}\left[\mathcal{D}\delta''\phi_\alpha\nabla_x\xi_\alpha\cdot\nabla_x\xi_\alpha\right]\,.\tag{A.28}$$

It is worth noticing that, instead of tracking the weighted nodes of the quadrature approximation (i.e. Eq. A.27), one could directly track the evolution of the quadrature nodes.

In that case, the transport equation would be obtained from Eq. A.27 as follow:

$$\begin{aligned}\phi_\alpha \frac{\partial}{\partial t}\xi_\alpha + \xi_\alpha \frac{\partial}{\partial t}\phi_\alpha + (\phi_\alpha \boldsymbol{v_b}) \cdot \nabla_x \xi_\alpha + \xi_\alpha \nabla_x \cdot (\phi_\alpha \boldsymbol{v_b}) + (\phi_\alpha \boldsymbol{v_{s,\alpha}}) \cdot \nabla_x \xi_\alpha + \\ \xi_\alpha \nabla_x \cdot (\phi_\alpha \boldsymbol{v_{s,\alpha}}) - \mathcal{D}\phi_\alpha \nabla_x^2 \xi_\alpha - 2\mathcal{D}\nabla_x \phi_\alpha \cdot \nabla_x \xi_\alpha - \mathcal{D}\xi_\alpha \nabla_x^2 \phi_\alpha = c_\alpha^\sigma \,,\end{aligned} \tag{A.29}$$

that becomes, after manipulation:

$$\begin{aligned}\phi_\alpha \left[\frac{\partial}{\partial t}\xi_\alpha + \boldsymbol{v_b} \cdot \nabla_x \xi_\alpha + \boldsymbol{v_{s,\alpha}} \cdot \nabla_x \xi_\alpha - \mathcal{D}\nabla_x^2 \xi_\alpha\right] + \\ \xi_\alpha \left[\frac{\partial}{\partial t}\phi_\alpha + \nabla_x \cdot (\phi_\alpha \boldsymbol{v_b}) + \nabla_x \cdot (\phi_\alpha \boldsymbol{v_{s,\alpha}}) - \mathcal{D}\nabla_x^2 \phi_\alpha\right] - 2\mathcal{D}\nabla_x \phi_\alpha \cdot \nabla_x \xi_\alpha = c_\alpha^\sigma \,.\end{aligned} \tag{A.30}$$

The second term of the left-hand side of Eq. A.30 is equal to $\xi_\alpha c_\alpha^\phi$ (see Eq. A.26) and thus:

$$\frac{\partial}{\partial t}\xi_\alpha + \boldsymbol{v_b} \cdot \nabla_x \xi_\alpha + \boldsymbol{v_{s,\alpha}} \cdot \nabla_x \xi_\alpha - \mathcal{D}\nabla_x^2 \xi_\alpha = c_\alpha^\xi \,, \tag{A.31}$$

where:

$$c_\alpha^\xi = \frac{c_\alpha^\sigma - c_\alpha^\phi \xi_\alpha + 2\mathcal{D}\nabla_x \phi_\alpha \cdot \nabla_x \xi_\alpha}{\phi_\alpha} \,. \tag{A.32}$$

In conclusion, if n is the number of classes in the quadrature approximation, solving the PBE with the DQMOM reduces to solving n transport equations for the quadrature weights (Eq. A.26) and n transport equations for the weighted nodes (Eq. A.27) - or alternatively n transport equations for the quadrature nodes (Eq. A.32). In Lagrangian form, the quadrature transport equations become:

$$\frac{D\phi_\alpha}{Dt} = -\phi_\alpha \nabla_x \cdot (\boldsymbol{v_b} + \boldsymbol{v_{s,\alpha}}) + \mathcal{D}\nabla_x^2 \phi_\alpha + c_\alpha^\phi \,, \tag{A.33}$$

$$\frac{D\sigma_\alpha}{Dt} = -\sigma_\alpha \nabla_x \cdot (\boldsymbol{v_b} + \boldsymbol{v_{s,\alpha}}) + \mathcal{D}\nabla_x^2 \sigma_\alpha + c_\alpha^\sigma \,, \tag{A.34}$$

$$\frac{D\xi_\alpha}{Dt} = \mathcal{D}\nabla_x^2 \xi_\alpha + c_\alpha^\xi \,, \tag{A.35}$$

where, by definition, it is:

$$\frac{D(\cdot)}{Dt} \equiv \frac{\partial(\cdot)}{\partial t} + \boldsymbol{v} \cdot \nabla_x(\cdot) \,. \tag{A.36}$$

A.4 Moment transform of the PBE

To close the source terms of the DQMOM transport equations, we apply this moment transform

$$\mathscr{M}_k \equiv \int_0^\infty \xi^k \hat{f}_v\left(\xi; \boldsymbol{x}, t\right) \mathrm{d}\xi \approx \sum_{\alpha=1}^{n} \phi_\alpha(\boldsymbol{x}, t)\xi_\alpha^k(\boldsymbol{x}, t) \tag{A.37}$$

to each term in Eq. A.28. However, before proceeding, we need to define some properties of the Dirac's delta function. Let us consider an arbitrary function $f(x)$. It holds true that:

$$\int_a^b f(x)\delta(x - x^*)dx = f(x^*)\,,\ x^* \in (a, b) \tag{A.38}$$

$$\int_a^b f(x)\delta'(x - x^*)dx = -\frac{df}{dx}(x^*)\,,\ x^* \in (a, b) \tag{A.39}$$

$$\int_a^b f(x)\delta''(x - x^*)dx = -\left[-\frac{d^2 f}{dx^2}(x^*)\right]\,,\ x^* \in (a, b) \tag{A.40}$$

Thus, the terms in Eq. A.28 become, in order:

$$\mathscr{M}_k \left(\sum_{\alpha=1}^{n} c_\alpha^\phi \delta\left(\xi - \xi_\alpha\right)\right) = \sum_{\alpha=1}^{n} c_\alpha^\phi \int_0^\infty \xi^k \delta\left(\xi - \xi_\alpha\right) d\xi = \sum_{\alpha=1}^{n} c_\alpha^\phi \xi_\alpha^k\,, \tag{A.41}$$

$$\begin{gathered}\mathscr{M}_k \left(\sum_{\alpha=1}^{n} (c_\alpha^{\phi\xi} - \xi_\alpha c_\alpha^\phi)\delta'\left(\xi - \xi_\alpha\right)\right) = \\ \sum_{\alpha=1}^{n} (c_\alpha^{\phi\xi} - \xi_\alpha c_\alpha^\phi) \int_0^\infty \xi^k \delta'\left(\xi - \xi_\alpha\right) d\xi = -k \sum_{\alpha=1}^{n} (c_\alpha^{\phi\xi} - \xi_\alpha c_\alpha^\phi)\xi_\alpha^{k-1}\,,\end{gathered} \tag{A.42}$$

$$\begin{gathered}\mathscr{M}_k \left(\sum_{\alpha=1}^{n} \mathcal{D}\delta''\left(\xi - \xi_\alpha\right) \phi_\alpha \nabla_x \xi_\alpha \cdot \nabla_x \xi_\alpha\right) = \\ \sum_{\alpha=1}^{n} \mathcal{D}\phi_\alpha \nabla_x \xi_\alpha \cdot \nabla_x \xi_\alpha \int_0^\infty \xi^k \delta''\left(\xi - \xi_\alpha\right) d\xi = k(k-1) \sum_{\alpha=1}^{n} \mathcal{D}\phi_\alpha \xi_\alpha^{k-2} \nabla_x \xi_\alpha \cdot \nabla_x \xi_\alpha\,.\end{gathered} \tag{A.43}$$

At this point, the $2n$ unknown source terms can be easily found by solving the linear algebraic system (or evolution equation) such obtained:

$$\begin{gathered}\sum_{\alpha=1}^{n} c_\alpha^\phi \xi_\alpha^k + k \sum_{\alpha=1}^{n} (c_\alpha^{\phi\xi} - \xi_\alpha c_\alpha^\phi)\xi_\alpha^{k-1} = \\ k(k-1) \sum_{\alpha=1}^{n} \mathcal{D}\phi_\alpha \xi_\alpha^{k-2} \nabla_x \xi_\alpha \cdot \nabla_x \xi_\alpha\,,\ k \in [0, 2n-1]\end{gathered} \tag{A.44}$$

If we employ a two-node quadrature approximation, the four source terms are the one reported in Eq. 5.21.

A.5 Substantial derivatives

In this section, we express the momentum balance in Lagrangian form. To this end, we start by applying the product rule to the the left hand side of Eq. 7.3, that becomes:

$$\begin{gathered}(\phi_k \rho^*)\frac{\partial}{\partial t}\boldsymbol{u_k} + (\phi_k \rho_k^* \boldsymbol{u_k})\nabla\cdot\boldsymbol{u_k} + \boldsymbol{u_k}\left[\frac{\partial}{\partial t}(\phi_k \rho_k^*) + \nabla\cdot(\phi_k \rho_k^* \boldsymbol{u_k})\right] = \\ \nabla\cdot\boldsymbol{\sigma_k} + \phi_k \rho_k^* \boldsymbol{g} + \boldsymbol{F_{b,k}} + \boldsymbol{F_k}\,. \end{gathered} \tag{A.45}$$

If we substitute the mass balance (Eq. 7.2), the latter yields:

$$(\phi_k \rho^*)\frac{\partial}{\partial t}\boldsymbol{u_k} + (\phi_k \rho_k^* \boldsymbol{u_k})\nabla\cdot\boldsymbol{u_k} = \nabla\cdot\boldsymbol{\sigma_k} + \phi_k \rho_k^* \boldsymbol{g} + \boldsymbol{F_{b,k}} + \boldsymbol{F_k}\,, \tag{A.46}$$

and hence,

$$(\phi_k \rho^*)\frac{\mathrm{D}}{\mathrm{D}t}\boldsymbol{u_k} = \nabla\cdot\boldsymbol{\sigma_k} + \phi_k \rho_k^* \boldsymbol{g} + \boldsymbol{F_{b,k}} + \boldsymbol{F_k}\,, \tag{A.47}$$

where $\frac{\mathrm{D}}{\mathrm{D}t}$ is the definition of substantial derivative:

$$\frac{\mathrm{D}}{\mathrm{D}t}\boldsymbol{u_k} \equiv \frac{\partial}{\partial t}\boldsymbol{u_k} + \boldsymbol{u_k}\nabla\cdot\boldsymbol{u_k}\,. \tag{A.48}$$

List of publications

This thesis is based on the following research publications.

Refereed journals publications

S. Volpato, M. Tirapelle, A. Santomaso, Modeling and experimental investigation of shear-induced particle percolation in diluted binary mixtures, *Physical Review E*, 102(1), (2020)

M. Tirapelle, S. Volpato, A. Santomaso, Shear-induced particle segregation in binary mixtures: Verification of a percolation theory, *Particuology*, 57, (2021)

M. Tirapelle, A. Santomaso, P. Richard, R. Artoni, Experimental investigation and numerical modelling of density-driven segregation in an annular shear cell, *Advanced Powder Technology*, 32, (2021) 1305-1317

M. Tirapelle, A. C. Santomaso, and L. Mazzei (2021). CFD-PBE coupled model for size-driven segregation in polydisperse granular flows. *Chemical Engineering Science*, 247, (2021) 117065.

Refereed conference publications

M. Tirapelle, L. Troncon, S. Volpato, A. Santomaso, Size segregation of ternary mixtures in inclined chute flows: an experimental study, *Chemical Engineering Transactions*, 86, (2021) 823-828

M. Tirapelle, A. Santomaso, P. Richard, R. Artoni, Shear-driven density segregation: an experimental study, *EPJ Web of Conferences*, 249, (2021) 03021